NACA RM L56F18a

NACA

RESEARCH MEMORANDUM

Rept. 1353

AN EXPERIMENTAL INVESTIGATION OF STING-SUPPORT EFFECTS ON DRAG AND A COMPARISON WITH JET EFFECTS AT TRANSONIC SPEEDS

By Maurice S. Cahn

Langley Aeronautical Laboratory
Langley Field, Va.

NATIONAL ADVISORY COMMITTEE
FOR AERONAUTICS

WASHINGTON
September 24, 1956

NATIONAL ADVISORY COMMITTEE FOR AERONAUTICS

RESEARCH MEMORANDUM

AN EXPERIMENTAL INVESTIGATION OF STING-SUPPORT EFFECTS ON DRAG AND A COMPARISON WITH JET EFFECTS AT TRANSONIC SPEEDS

By Maurice S. Cahn

SUMMARY

This paper presents the results of an investigation of sting-support interference on afterbody drag at transonic speeds. Stings with varying diameter, cone angle, and cylindrical length were tested at the rear of a model with various afterbody shapes. The data were obtained at an angle of attack of 0° and at Mach numbers from 0.80 to 1.10. It was found that, in general, the addition of a sting caused a drag reduction. A method is presented whereby approximate sting-interference corrections may be made to models with afterbodies and sting supports of similar size and scale to those of this paper provided the boundary layer is turbulent at the model base and the Reynolds numbers are of the same order of magnitude. Reynolds number of the tests presented varied from 15.0×10^6 to 17.4×10^6 based on body length.

Sting effects from this investigation are compared with data of jet effects on the same afterbodies. The results of this comparison indicate that for the more gradually contoured afterbodies, a sting shape can be found which will duplicate the jet effects, but that for blunt afterbodies no solid sting shape will duplicate the jet effects.

INTRODUCTION

A large part of wind-tunnel testing involves the use of rear sting-supported models. Experimental data for sting-support effects on model characteristics are needed in order to estimate more exactly free-flight conditions. A recent summary of information on sting-support interference (ref. 1) presents a comprehensive study of sting effects at supersonic speeds. However, as noted in reference 1, the acute problem at transonic speeds requires more experimental data.

An investigation has been conducted in the Langley 8-foot transonic tunnel to evaluate some of the effects of sting-support configuration on the drag characteristics of a systematic series of afterbodies. The tests were conducted at an angle of attack of 0° through the Mach number range from 0.80 to 1.10 for stings with varying cone-angle, length, and diameter. The sting effects determined are compared with data of jet effects on the same afterbodies.

SYMBOLS

A	cross-sectional area
C_D	pressure drag coefficient, $\sum \frac{P_l A_l}{A_m}$
ΔC_D	increment between total afterbody pressure drag coefficient at any given D_b/l and at $D_b/l = 0$
$\Delta C_{D_{max}}$	increment between total afterbody pressure drag coefficient at $D_b/l = \infty$ and at $D_b/l = 0$
D	diameter
H_j/p_o	ratio of jet total pressure to free-stream static pressure
L	body length
l	sting length between model base and sting cone
M	free-stream Mach number
P	pressure coefficient, $\frac{p_l - p_o}{q_o}$
p	static pressure
q	dynamic pressure
R	Reynolds number based on body length
T_j	jet total temperature, $^{\circ}F$

β	afterbody boattail angle, deg
θ	sting cone half-angle, deg

Subscripts:

A	afterbody
b	base
s	sting
o	free stream
β	boattail
l	local
m	model maximum

APPARATUS AND METHODS

Wind Tunnel

This investigation was conducted in the Langley 8-foot transonic tunnel which has a dodecagonal slotted test section. Continuous testing up to a Mach number of 1.10 was possible for these models. Details of the test section are presented in reference 2. Characteristics of the airstream are given in reference 3 wherein it is shown that the maximum deviation from the indicated free-stream Mach number is ± 0.003.

Models

The models used in the investigation were bodies of revolution that consisted of a single forebody with interchangeable afterbodies. These bodies had fineness ratios of 10 or 10.6, depending on the choice of afterbody. They were supported in the tunnel as shown in figure 1 by two 45° swept struts. These struts had chords of 11.25 inches and NACA 65-010 airfoil sections measured parallel to the airstream. Their leading edges intersected the bodies 21.7 inches from the nose.

Drawings of the afterbody shapes are shown in figure 2. Table I shows the equation utilized to define the external shapes of the afterbodies investigated with the exception of afterbody IX. Afterbody IX, while not of this afterbody family, is included since it provides a low

boattail angle otherwise not available for the bodies having a fineness ratio of 10.0. Tabulated in table II are the ordinates from which the body shapes were constructed. These configurations with the exception of afterbody XI were the same as those used in reference 4.

The models were instrumented with 26 static-pressure orifices in each of three rows located 0°, 45°, and 72° from the plane of symmetry. Orifice distribution was the same in each row. Also there were two diametrically opposite base-pressure orifices located a short distance inside the model base annulus.

Stings

The stings were constructed of wood and were attached to the rear of the models by means of an adapter contained within the sting and the afterbody. The models were tested with no sting and with the stings shown in figure 3. These consisted of stings with conical half-angles from 0° to 10° and with no cylindrical sections ahead of the cone, stings with conical half-angles of 5° and lengths of cylindrical section ahead of the cone varying from 0 to 13.40 inches, and cylindrical stings with diameters varying from 0.84 to 2.36 inches. The overall length of all stings was 26 inches.

Tests and Measurements

Various stings were tested with each afterbody at an angle of attack of 0°. For each configuration, the Mach number was varied in 0.05 increments from 0.80 to 1.10. Reynolds number based on body length varied from 15.0×10^6 to 17.4×10^6. (See fig. 4.) All pressures were photographically recorded from multiple tube manometers.

Reduction of Data

The pressure coefficients of these tests were numerically integrated to obtain values of afterbody pressure drag coefficient which are based on body frontal area. The stings used in this investigation had no effect on the forebody pressure drag as will be shown in the section entitled "Results and Discussion." Base drags were obtained by assuming that measured base pressures acted over the entire model base.

PRECISION

Total-drag coefficient errors due to possible inaccuracies in measurement and to tunnel empty stream nonuniformities are estimated generally to be less than 0.005 at subsonic speeds and not more than 0.010 at supersonic speeds.

The magnitude of the sting effects may be somewhat affected by tunnel-wall disturbances above $M = 1.0$. A detailed analysis of shock reflections of this type may be found in reference 3.

RESULTS AND DISCUSSION

Description of Flow Phenomena

Prior to presentation of these results, it is believed a brief discussion of the flow mechanism occurring at the model base would be desirable. Since the flow will separate from the body at the model base, a region of low-energy air will be created immediately behind the base. As a consequence, the streamline adjacent to the wake will have essentially a constant pressure. How the pressure at the base arrives at its steady value can be illustrated by considering a cylindrical afterbody. If in some way an external stream is immediately imposed on this afterbody, the base pressure will in the first instant be equal to the free-stream static pressure. (See fig. 5(a).) After some time, due to viscous mixing, the external stream will aspirate the base region and lower its pressure. The free stream will be turned inward with an accompanying increase in velocity. Viscous mixing now being stronger will cause more aspiration of the base region with further turning inward of the free stream. Opposing this effect is the increase in pressure in the wake where the external stream must be turned to become horizontal again. Since the base region will also feel this wake pressure rise, a base pressure will be established when the two opposing effects are in equilibrium. (See fig. 5(b).)

Boattailing, if not so great as to cause separation ahead of the base will cause an increase in base pressure. (See fig. 5(c).) This increase in base pressure results from an increase in compression over the body as well as the fact that less wake region is exposed to the aspiration effects of the external stream. Placing a sting in the rear of a model, in addition to causing less wake exposure, requires the external stream to be turned outward more rapidly. (See fig. 5(d).) These effects result in a base-pressure increase. Increasing the sting cone angle or moving the sting cone closer to the base will cause a further increase in the external stream turning rate near the base resulting in a further base-pressure increase.

A sting also has effects on the body pressures ahead of the model base which are similar to the sting effects on base pressure. These effects which are transmitted through the body boundary layer become smaller with increasing distance upstream of the base as shown in figure 6. In figure 6 are typical pressure distributions over the body with and without a sting. The pressure coefficients for the orifice row along the plane of symmetry are shown for two afterbodies at four Mach numbers. The two afterbodies represent a blunt and a gradually contoured rear end configuration, and the sting is the one which had the largest effect. It can be seen that the sting did not affect the body pressures forward of the 60-percent station.

Effect of Sting Configuration on Base Pressure

In figure 7, base pressure coefficients are presented as a function of sting half-angle, length, and cross-sectional-area parameters. As previously stated, the presence of a sting results in changes in base pressure as well as similar changes in body pressures upstream of the base. Consequently, as would be expected, the variations in afterbody drag, which will be discussed in the following sections, are similar to changes in base pressure.

Effect of Sting Configuration on Drag

Sting cone-angle effect.- Figure 8 shows the effect of sting half-angle on afterbody pressure drag. Presented at Mach numbers from 0.80 to 1.10 are curves of base, boattail, and total afterbody pressure drag coefficients as a function of sting half-angle for each body tested. The length of the sting-cylindrical section ahead of the sting cone is zero. These data show that in spite of the large differences in absolute drag values, the curves are similar for all afterbodies in that the drag became lower with increasing sting cone angle. This trend occurred primarily because of the more rapid rate of turning of the external stream with increasing sting cone angle. It should be pointed out that the downstream end of the sting cones was limited to a diameter of 3.75. Sting cones with different downstream diameters might be expected to result in sting effects different from those of this investigation.

Since the curves of figure 8 tended to be linear, slopes of the total afterbody drag curves were taken. These slopes are plotted in figure 9 and can be used to summarize the sting-cone angle effect. For the cases where the variation of drag with sting cone angle was not linear, the slopes were taken so as to favor the low-angle portion of the curves. For afterbodies I, II, and III, the curves indicate that the sting-cone angle effect near the speed of sound can be double the effect noted at higher and lower speeds. The subsonic and supersonic levels of

the angle effect, $\partial C_{D_A}/\partial\theta$, for all bodies were of the order of -0.006 with the exception of afterbody VI. Afterbody VI was effectively the most blunt afterbody tested. It can be seen that increasing boattail angle in general caused an increase in sting-angle effect. This was due to the increased turning rate required by the external stream at the model base.

Sting-cone-position effect.- Figure 10 shows the effect of varying sting-cone position along the sting on base, boattail, and afterbody pressure drag coefficients. These data were obtained with 5° cones behind varying lengths of constant-diameter cylindrical sting sections. A drag reduction always occurred as the sting cone was moved toward the base causing an increased rate of turning of the external flow. Similar trends although of different magnitude were noted in reference 5 for a somewhat different configuration. It should again be pointed out that stings with different limiting diameters of the downstream end of the cone may produce drag effects of a different magnitude.

The effect of sting-cone position has been determined for stings with a 5° cone angle only. However, it is felt that reasonable approximations of the effect of varying cone position for stings with other cone angles can be obtained by proper interpolation of the results presented herein. A simple method of achieving this can be illustrated by use of a typical plot of drag coefficient against sting angle. (See following sketch.)

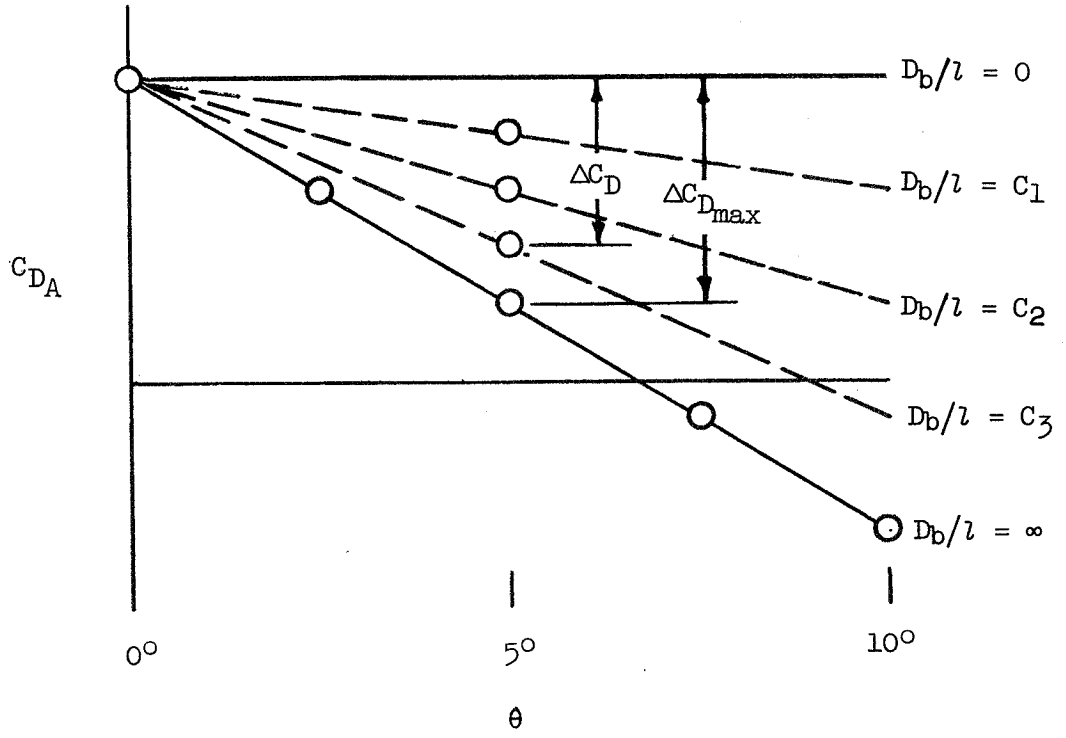

The entire range of angles and lengths is bounded by the two linear curves for $D_b/l = 0$ and $D_b/l = \infty$. The curves for the intermediate values of D_b/l cannot cross over each other since the variation of drag with sting length is a monotonic function. Therefore, it would appear that the drag for intermediate values of D_b/l could be reasonably approximated with linear curves. Having the drag values for the intermediate D_b/l values for $\theta = 5^\circ$ will allow these approximation lines to be determined.

Let ΔC_D be defined as the difference between total afterbody drag coefficient at any given D_b/l and at $D_b/l = 0$, and let $\Delta C_{D_{max}}$ be the difference between total afterbody drag coefficient at $D_b/l = \infty$ and $D_b/l = 0$. Then on the basis of the above discussion $\Delta C_D/\Delta C_{D_{max}}$ for any D_b/l may be considered to be approximately a constant for all values of θ. The parameter $\Delta C_D/\Delta C_{D_{max}}$ represents the ratio of sting-cone effect on drag for a given sting length (D_b/l) to the maximum sting-cone effect on drag. The maximum effect is obtained when the sting length is zero $(D_b/l = \infty)$. Values of $\Delta C_D/\Delta C_{D_{max}}$ obtained from the data of figure 10 are presented in figure 11(a). Their variation with D_b/l is shown for each afterbody configuration through the Mach number range. Values of $\Delta C_D/\Delta C_{D_{max}}$ for configurations having larger values of D_b/l than those shown in figure 11(a) may be obtained in figure 11(b). These values are plotted against the reciprocal of D_b/l for each afterbody configuration through the Mach number range. Figure 12 presents the slopes of the linear portion of the curves shown in figure 11(a). The magnitude of these slopes is about 1.0 for all configurations.

Sting-diameter effect.- The effect on the base, boattail, and afterbody pressure drag coefficients of varying the diameter of a cylindrical sting is presented in figure 13 for each afterbody. No sting cone was present on the sting for these data and the effect of limiting the sting length to 26 inches is felt to be negligible. It can be seen that, in general, the effect of increasing the sting size was to decrease the drag. An attempt was made here to make these data more useful by taking average slopes of total afterbody pressure drag with the sting size parameter. These slopes are plotted against Mach number in figure 14. The slopes are seen to vary from approximately zero to -0.05.

Sting-Interference Corrections

The scope of the present investigation was rather large; that is, there were a large number of afterbodies and stings tested in combination.

Hence, a general equation has been derived to simplify the use of the experimental results in correcting wind-tunnel drag measurements for sting-interference effects. Although the scope of the present investigation was rather large, it was necessarily limited. Therefore, any corrections obtained empirically from these results should be restricted to stings and afterbodies similar in scale and shape to those investigated. It is also recommended that the results only be used for models whose Reynolds number and boundary-layer conditions comply with those of the present tests. (See ref. 1.) The boundary layer was turbulent ahead of the model base for the present tests.

Provided the previously mentioned limitations apply, it is suggested that the derived general equation be used for obtaining sting interference corrections in the following manner. After selecting a similar afterbody shape from this report, the correction due to the presence of the sting cone is

$$\Delta C_D = \left(\frac{\Delta C_D}{\Delta C_{D_{max}}}\right)\Delta C_{D_{max}}$$

where $\Delta C_D/\Delta C_{D_{max}}$ can be read from figure 11 for the proper values of D_b/l and M, or for D_b/l less than 0.5 $\Delta C_D/\Delta C_{D_{max}}$ can be approximated by using figure 12.

Also noting as before that the variation of C_D with sting angle is linear, then

$$\Delta C_{D_{max}} = \theta\left(\frac{\partial C_{D_A}}{\partial \theta}\right)$$

where $\partial C_{D_A}/\partial\theta$ can be read from figure 9 for the correct value of M.

This means that the drag correction

$$\Delta C_D = \theta\left(\frac{\Delta C_D}{\Delta C_{D_{max}}}\right)\left(\frac{\partial C_D}{\partial \theta}\right)$$

will correct data for a sting with a conical section to data for a sting with a cylindrical section only.

In order to correct for the cylindrical-section diameter

$$\Delta C_D = \left(\frac{A_s}{A_b}\right)\left[\frac{\partial C_{D_A}}{\partial(A_s/A_b)}\right]$$

where $\frac{\partial C_{D_A}}{\partial(A_s/A_b)}$ can be read from figure 14. The complete sting correction then becomes

$$\Delta C_D = \theta\left(\frac{\Delta C_D}{\Delta C_{D_{max}}}\right)\left(\frac{\partial C_{D_A}}{\partial \theta}\right) + \left(\frac{A_s}{A_b}\right)\left[\frac{\partial C_{D_A}}{\partial(A_s/A_b)}\right]$$

The correction thus obtained must be subtracted from the total-drag coefficient based on model frontal area. It should be noted that the value of ΔC_D will in all cases be negative and will result in a drag increase when data are corrected to the sting-off condition. It is estimated that the above method of obtaining sting corrections will give drag-coefficient increments generally within 0.03 of the values obtained using the actual data points.

Corrections determined from the present results have been calculated for a model discussed in reference 6. In figure 15, the resulting corrections are compared with the corrections determined by the method described in reference 6. The model of reference 6 had $\beta = 5.6°$, $D_b/D_m = 0.416$, $\theta = 4.2°$, $D_b/l = \infty$, and $A_s/A_b = 0.85$. Afterbody IX was chosen as most closely approximating the model. The model was tested in a closed-throat tunnel. The sting corrections in reference 6 were determined by using decreasing sting sizes and extrapolating to zero sting size. Figure 15 indicates good agreement between the present test and reference 6 for all configurations below a Mach number of 0.9. Above this speed, there are indications that sting corrections are more sensitive to changes in tail configurations.

A direct comparison with the sting effects of references 5 and 7 could not be made since none of the afterbodies of this report approximate the configurations of references 5 and 7. However, it is worthy of note that the sting effects in references 5 and 7 are considerably larger than any of this test. This is a result of the configurations of references 5 and 7 having larger values of D_b/D_m (0.737 and 1.00, respectively).

Simulation of Jet Effects With a Sting

The present investigation which was made in conjunction with the tests of reference 4, included unpublished results on a sting which had the shape of a free sonic jet expanding from the rear of the bodies. The sting was determined by schlieren photograph measurements of a jet at a total-pressure ratio of 5 and a temperature of 1,200° F. This sting having the same size and shape as the free jet always produced higher afterbody pressures than the jet. This is what might be expected since the sting could produce the solid-body effect but not the aspirating effect of the jet.

There is, however, a possibility of simulating jet effects with a sting of a different shape than that of the free jet. In figure 16 is shown the variation of afterbody pressure drag coefficient with the sting parameters of this paper and with jet total-pressure ratio for a sonic free jet exhausting at 1,200° F. The jet data are the same as that in reference 4 with the exception of data for afterbody XI which is from unpublished data.

Figure 16 indicates that for the gradually contoured afterbodies a practical sting shape can be made which will produce the same drag as the jet at a given pressure ratio. As the afterbody shape becomes more blunt, the aspiration effect of the jet becomes increasingly predominant on the larger wake behind the blunt rear end, and it becomes increasingly more difficult to duplicate the jet effect with solid sting shapes. This duplication is impossible for afterbodies III and VI for reasonable jet-pressure ratios. Because of the small-diameter sting required, jet duplication is impractical for afterbody V. Afterbodies IV and IX would probably show agreement between sting and jet data at pressure ratios above those presented since for the higher jet pressure ratios, the free jet size would increase and cause higher aft-end pressures.

CONCLUSIONS

The following conclusions have been drawn as a result of the present investigation:

1. The presence of a sting in general causes a drag reduction.

2. Increasing sting cone angle, decreasing sting cylindrical length ahead of the sting cone, and in general increasing sting diameter causes a drag reduction.

3. Sting-cone-angle effect increases with increasing boattail angle.

4. Approximate sting interference corrections can be made on models with afterbodies and sting supports similar in scale and geometry to those reported on herein provided the Reynolds number is of the same order of magnitude and the boundary layer ahead of the model base is turbulent.

5. For gradually contoured afterbodies, a sting can be made which will duplicate jet effects, but for blunt afterbodies no solid sting shape will produce the same effect as the jet.

Langley Aeronautical Laboratory,
National Advisory Committee for Aeronautics,
Langley Field, Va., June 4, 1956.

REFERENCES

1. Love, Eugene S.: A Summary of Information on Support Interference at Transonic and Supersonic Speeds. NACA RM L53K12, 1954.

2. Wright, Ray H., and Ritchie, Virgil S.: Characteristics of a Transonic Test Section With Various Slot Shapes in the Langley 8-Foot High-Speed Tunnel. NACA RM L51H10, 1951.

3. Ritchie, Virgil S., and Pearson, Albin O.: Calibration of the Slotted Test Section of the Langley 8-Foot Transonic Tunnel and Preliminary Experimental Investigation of Boundary-Reflected Disturbances. NACA RM L51K14, 1952.

4. Henry, Beverly Z., Jr., and Cahn, Maurice S.: Preliminary Results of an Investigation at Transonic Speeds To Determine the Effects of a Heated Propulsive Jet on the Drag Characteristics of a Related Series of Afterbodies. NACA RM L55A24a, 1955.

5. Tunnell, Philips J.: An Investigation of Sting-Support Interference on Base Pressure and Forebody Chord Force at Mach Numbers From 0.60 to 1.30. NACA RM A54K16a, 1955.

6. Osborne, Robert S.: High-Speed Wind-Tunnel Investigation of the Longitudinal Stability and Control Characteristics of a 1/16-Scale Model of the D-558-2 Research Airplane at High Subsonic Mach Numbers and at a Mach Number of 1.2. NACA RM L9C04, 1949.

7. Hart, Roger G.: Effects of Stabilizing Fins and a Rear-Support Sting on the Base Pressures of a Body of Revolution in Free Flight at Mach Numbers From 0.7 to 1.3. NACA RM L52E06, 1952.

TABLE I.- AFTERBODY DESIGN

Equation:

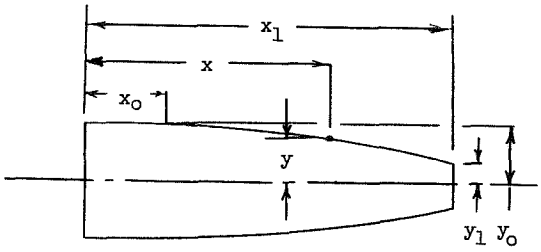

$$y = y_o - (y_o - y_1)\left(\frac{x - x_o}{x_1 - x_o}\right)^{\left(\frac{x_1 - x_o}{y_o - y_1}\right)\tan \beta}$$

where:

x	any afterbody station	y_1	body base radius
x_1	body base station	y_o	maximum body radius
x_o	end of cylindrical section	β	boattail angle
y	radius at station x	$\frac{x_1 - x_o}{y_o - y_1}$	= Constant

Design values:

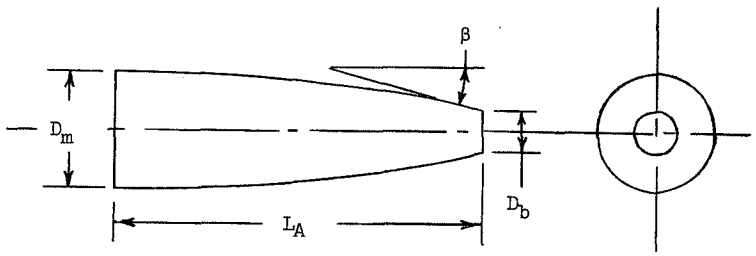

Afterbody	D_m, in.	L_A, in.	β, deg	D_b, in.	x_o
XI	5.0	15.70	8	1.672	2.81
I	5.0	15.70	16	1.672	2.81
II	5.0	15.70	24	1.672	2.81
III	5.0	15.70	45	1.672	2.81
IX	5.0	19.55	7.7	2.513	Not defined by above equation
IV	5.0	12.72	16	2.364	2.51
V	5.0	12.72	24	2.364	2.51
VI	5.0	12.72	45	2.364	2.51

TABLE II.- BODY ORDINATES

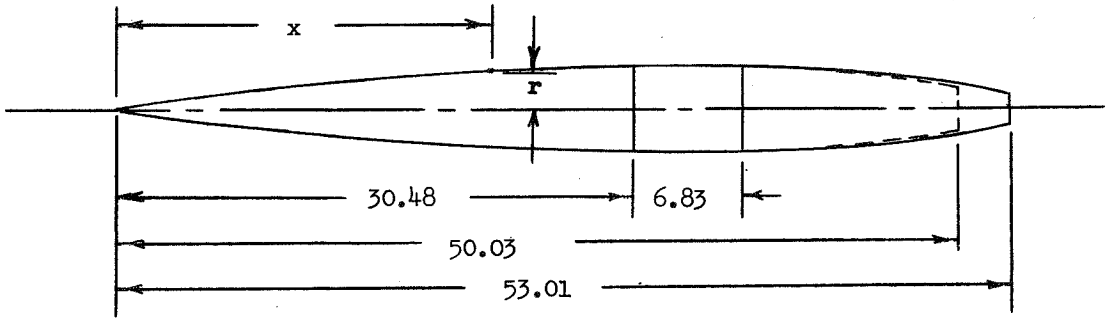

Forebody Ordinates

Station x, in.	Radius	Station x, in.	Radius
0.300	0.139	12.000	1.854
.450	.179	15.000	2.079
.750	.257	18.00	2.245
1.500	.433	21.000	2.360
3.000	.723	24.000	2.438
4.500	.968	27.000	2.486
6.000	1.183	30.000	2.500
9.000	1.556	30.480	2.500

Afterbody Ordinates

Station x, in.	Radius, r, in.							
	XI	I	II	III	IX	IV	V	VI
30.48	2.500	2.500	2.500	2.500	2.500	2.500	2.500	2.500
33.12	-----	-----	-----	-----	2.478	-----	-----	-----
36.12	-----	-----	-----	-----	2.414	-----	-----	-----
37.31	2.500	2.500	2.500	2.500	-----	2.500	2.500	2.500
39.12	-----	-----	-----	-----	2.305	-----	-----	-----
40.12	2.500	2.500	2.500	2.500	-----	2.499	2.500	2.500
42.12	2.278	2.469	2.495	2.500	2.137	2.446	2.488	2.500
44.12	2.030	2.364	2.458	2.500	-----	2.293	2.414	2.498
45.12	-----	-----	-----	-----	1.877	-----	-----	-----
46.12	1.772	2.176	2.350	2.496	-----	2.031	2.211	2.469
48.12	1.506	1.901	2.130	2.459	1.516	1.654	1.814	2.235
50.03	-----	-----	-----	-----	1.257	1.182	1.182	1.182
50.12	1.235	1.534	1.752	2.268	-----	-----	-----	-----
51.12	1.098	1.315	1.490	2.013	-----	-----	-----	-----
52.12	0.960	1.073	1.172	1.545	-----	-----	-----	-----
53.01	0.836	.836	.836	.836	-----	-----	-----	-----

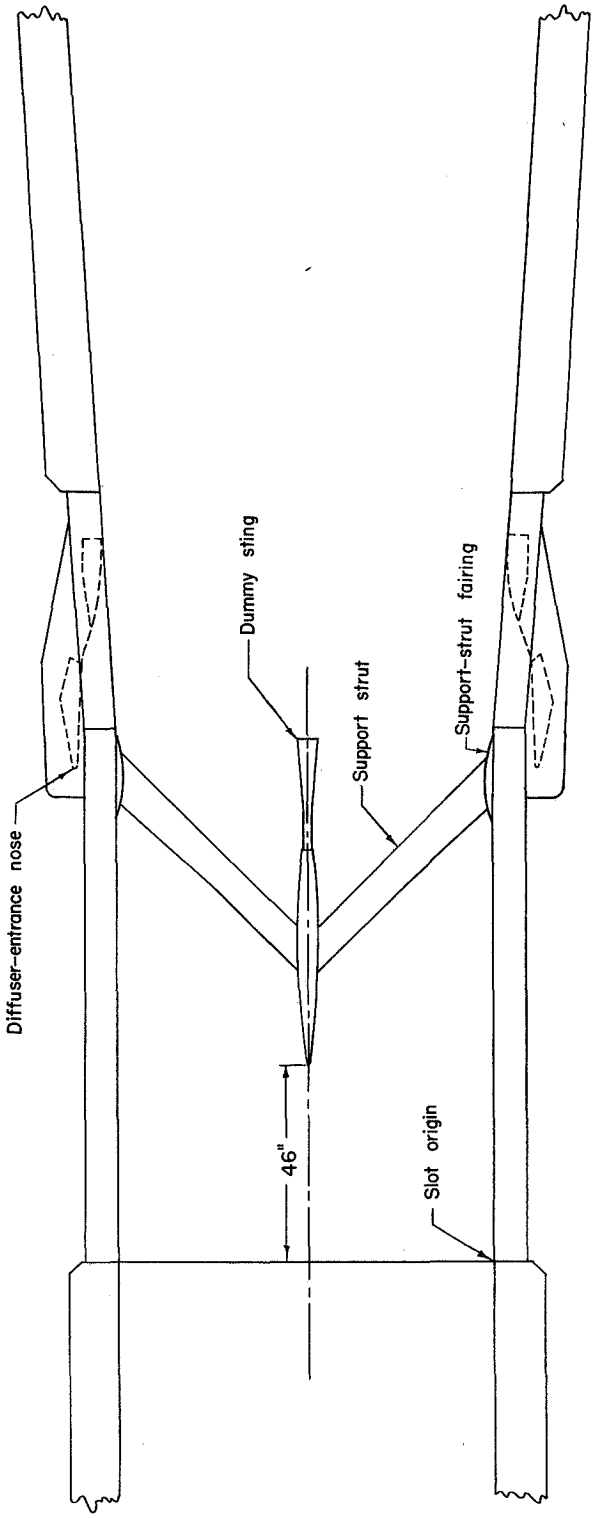

Figure 1.- Test model of sting interference in Langley 8-foot transonic tunnel.

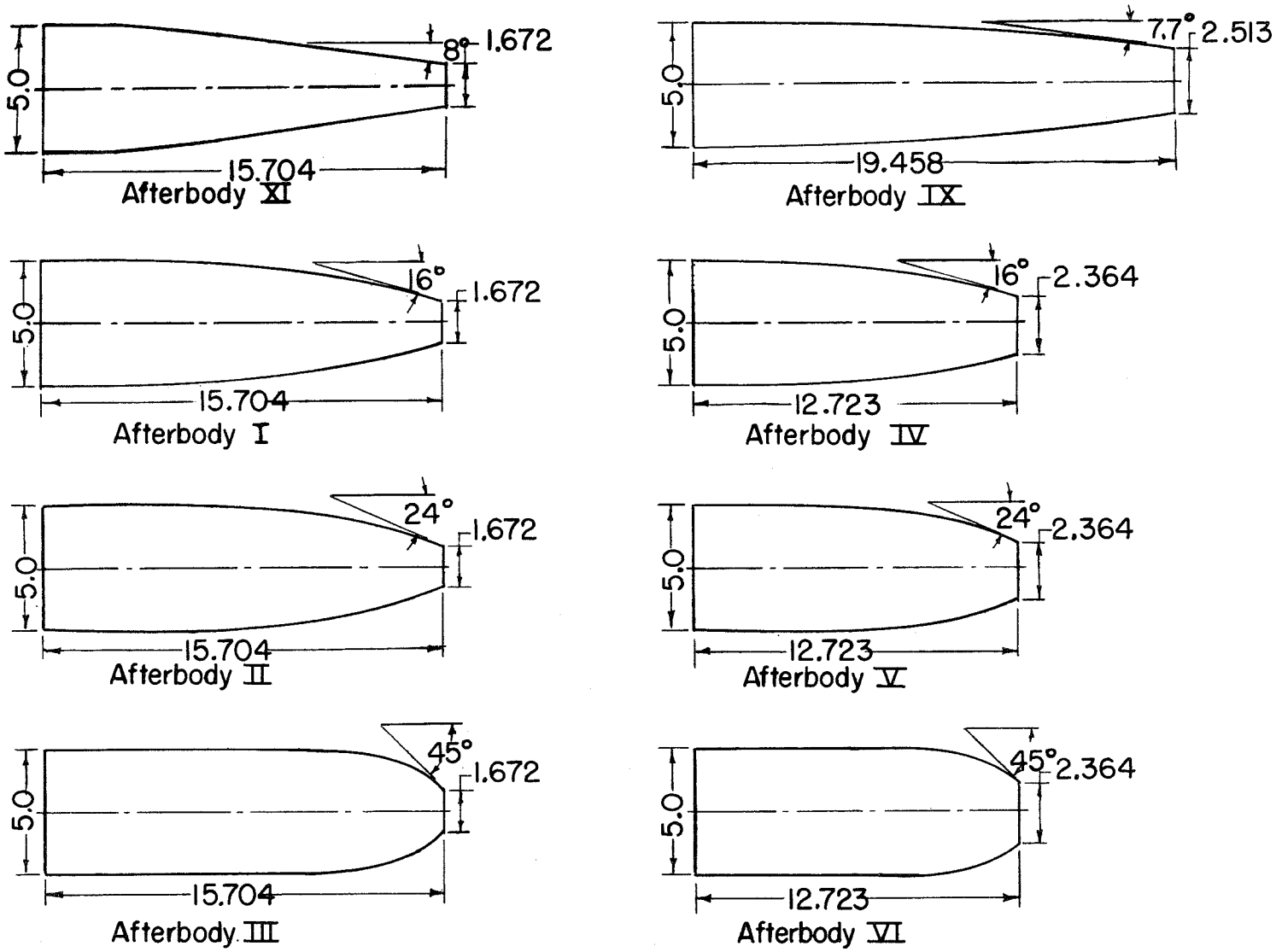

Figure 2.- Afterbody shapes investigated. All dimensions are in inches.

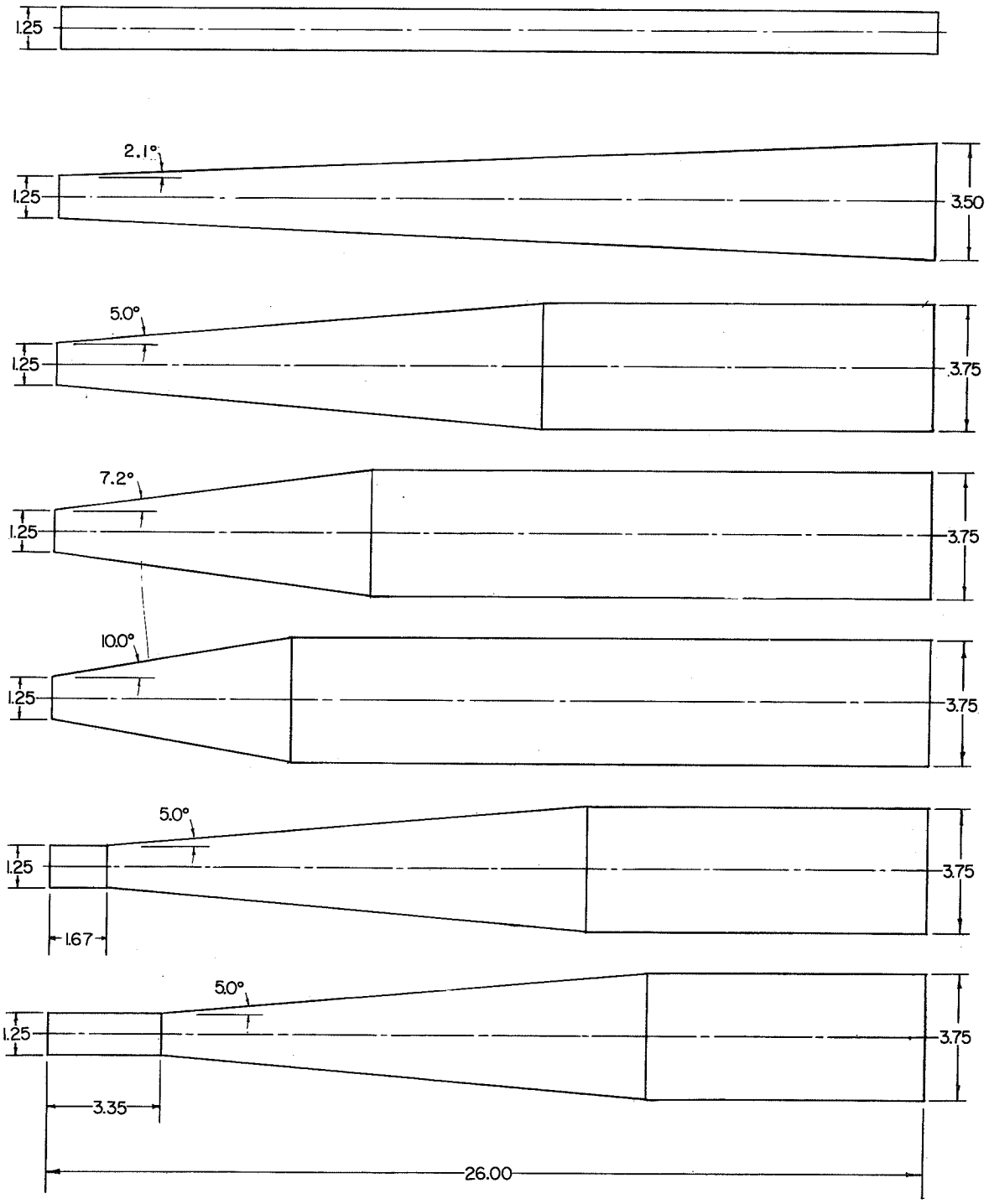

Figure 3.- Sting shapes investigated. All dimensions are in inches.

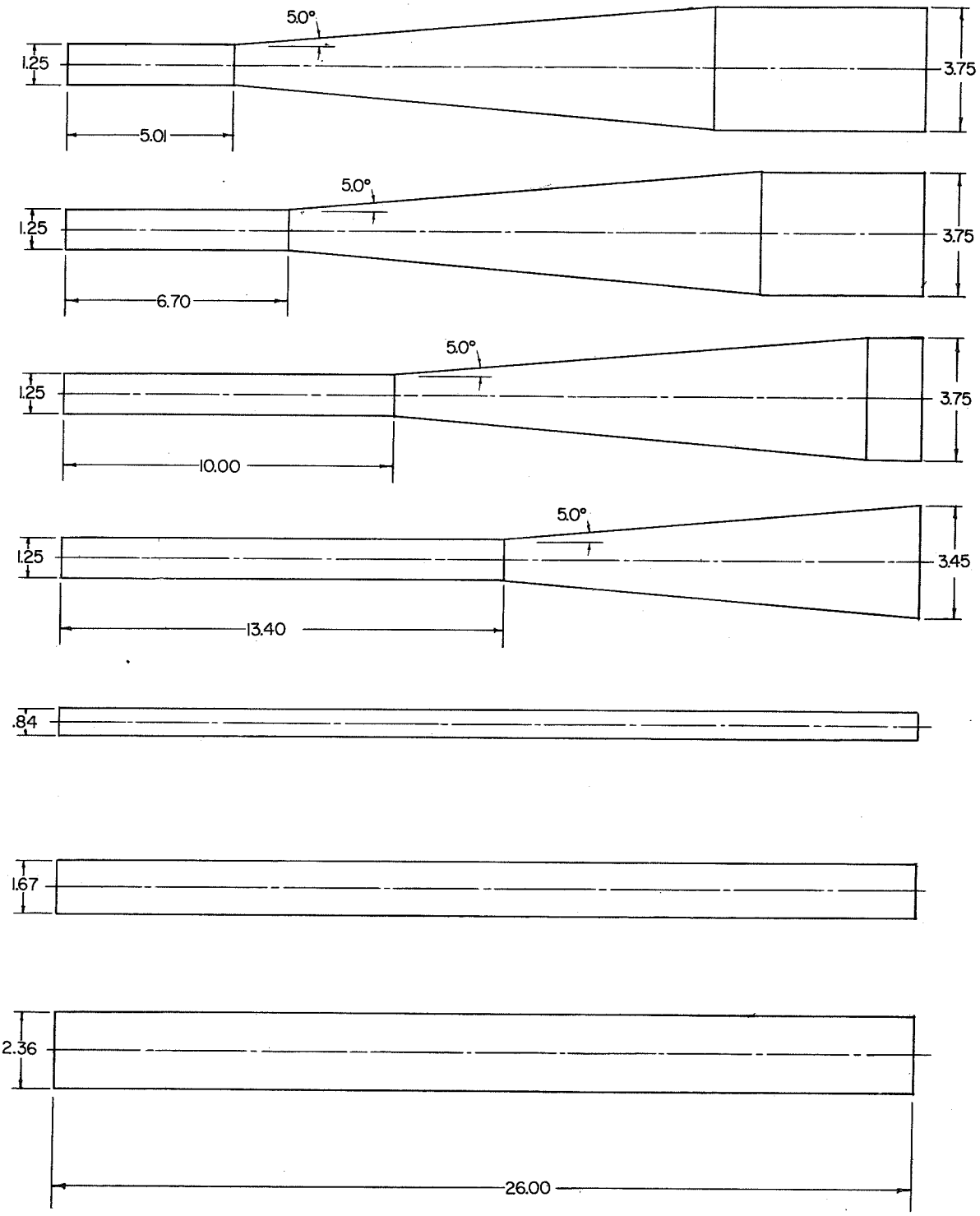

Figure 3.- Concluded.

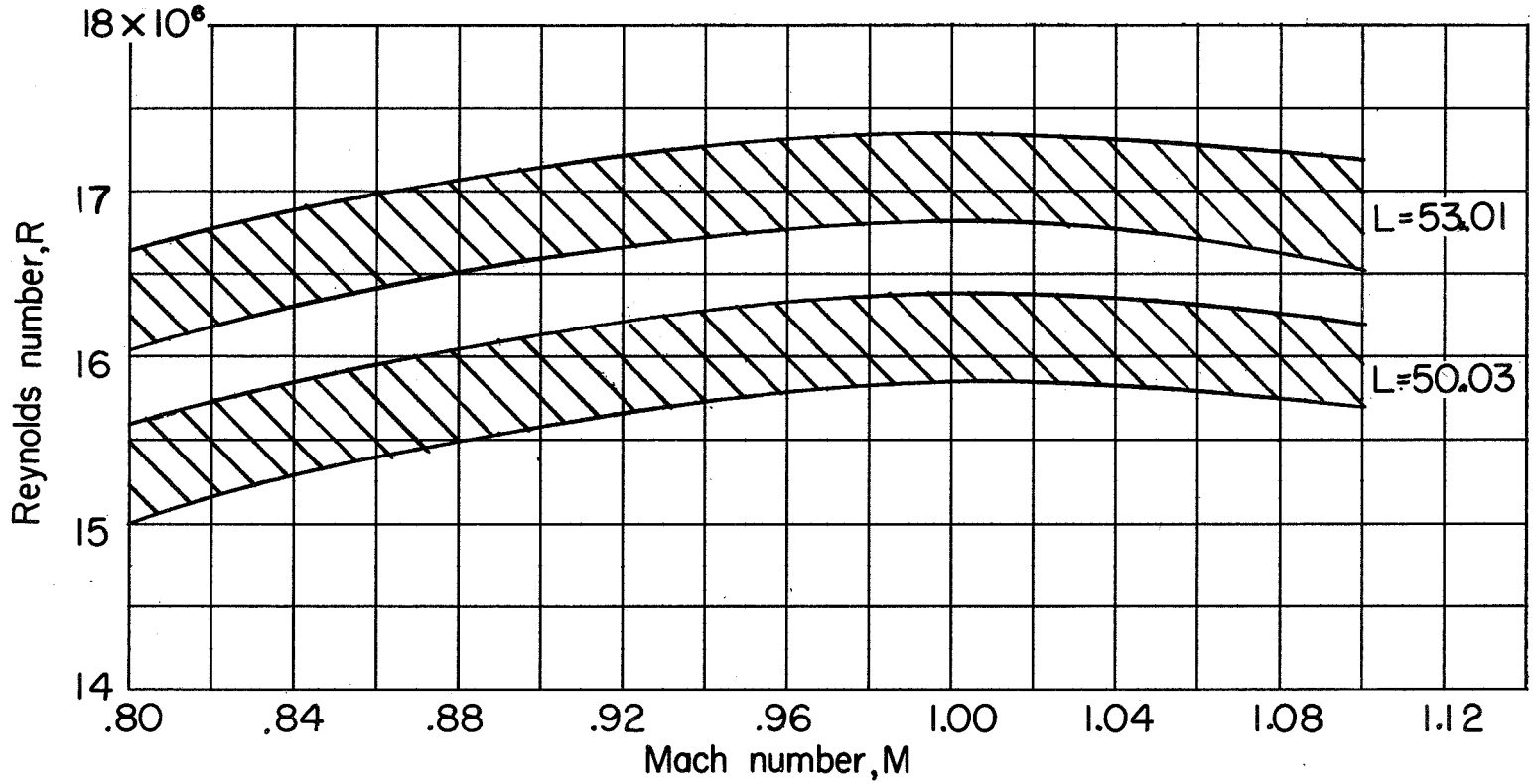

Figure 4.- Variation of Reynolds number, based on body length, with Mach number.

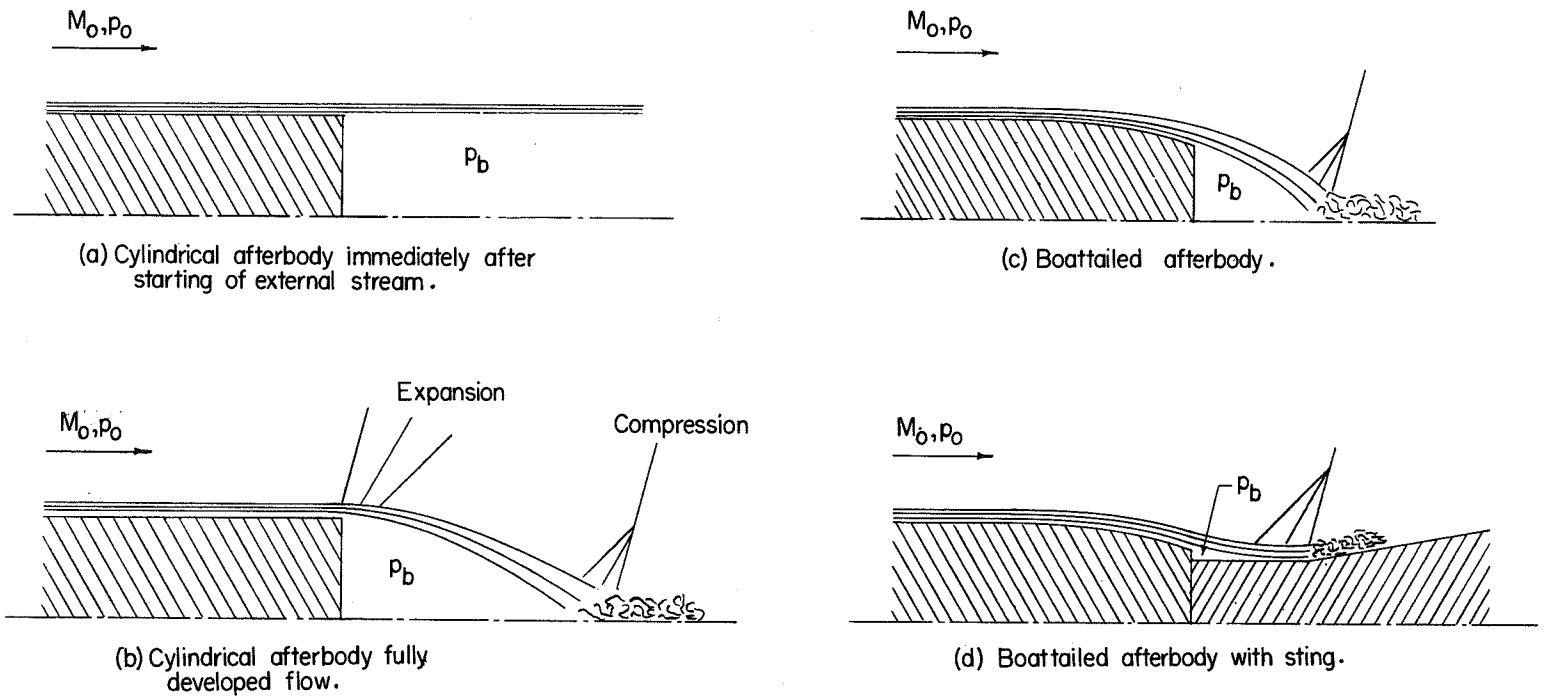

Figure 5.- Sketch of flow mechanism at base.

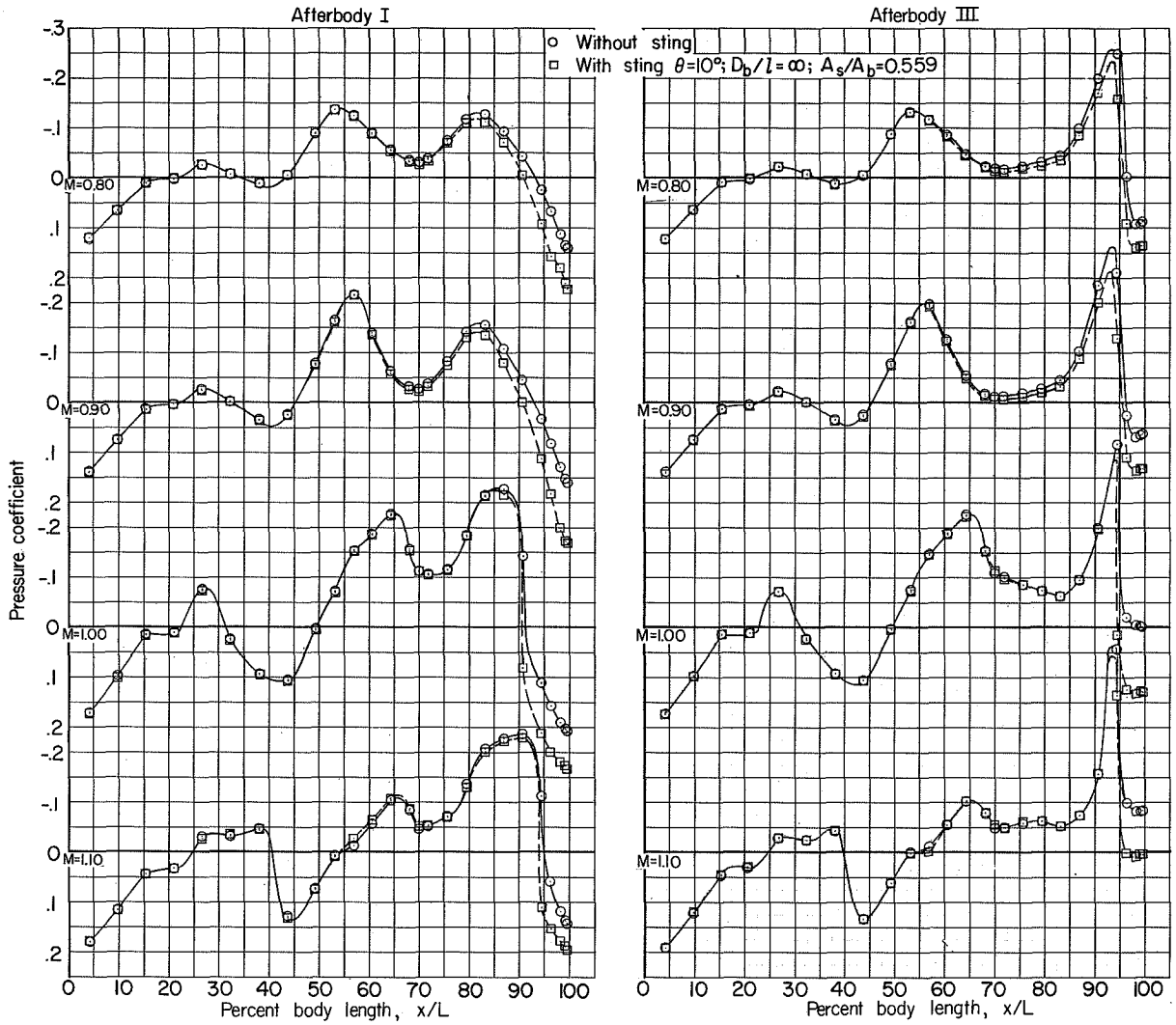

Figure 6.- Typical pressure distributions for orifice row along the plane of symmetry.

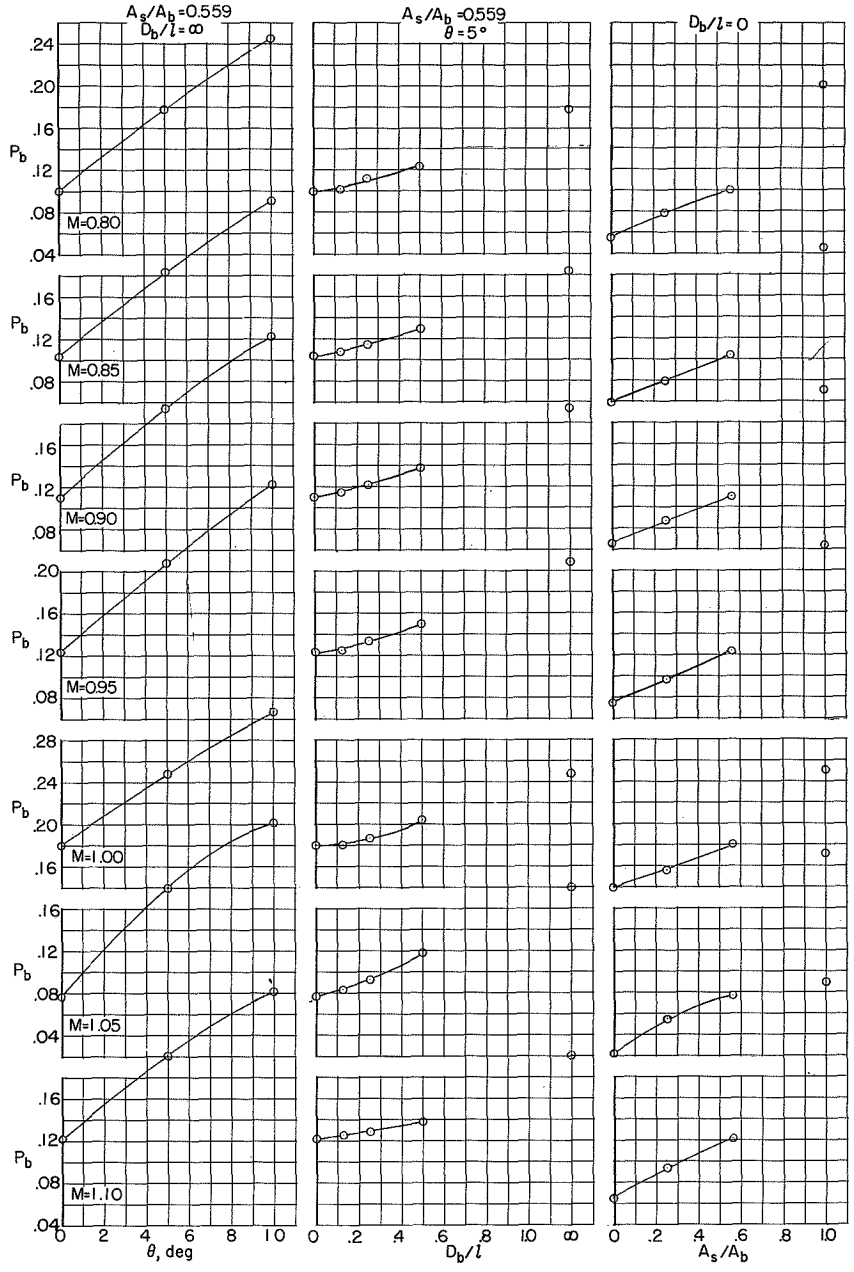

(a) Afterbody XI. $\beta = 8^{\circ}$; $\frac{D_b}{D_m} = 0.334$.

Figure 7.- Variation of base pressure coefficient with sting parameters at different values of stream Mach number.

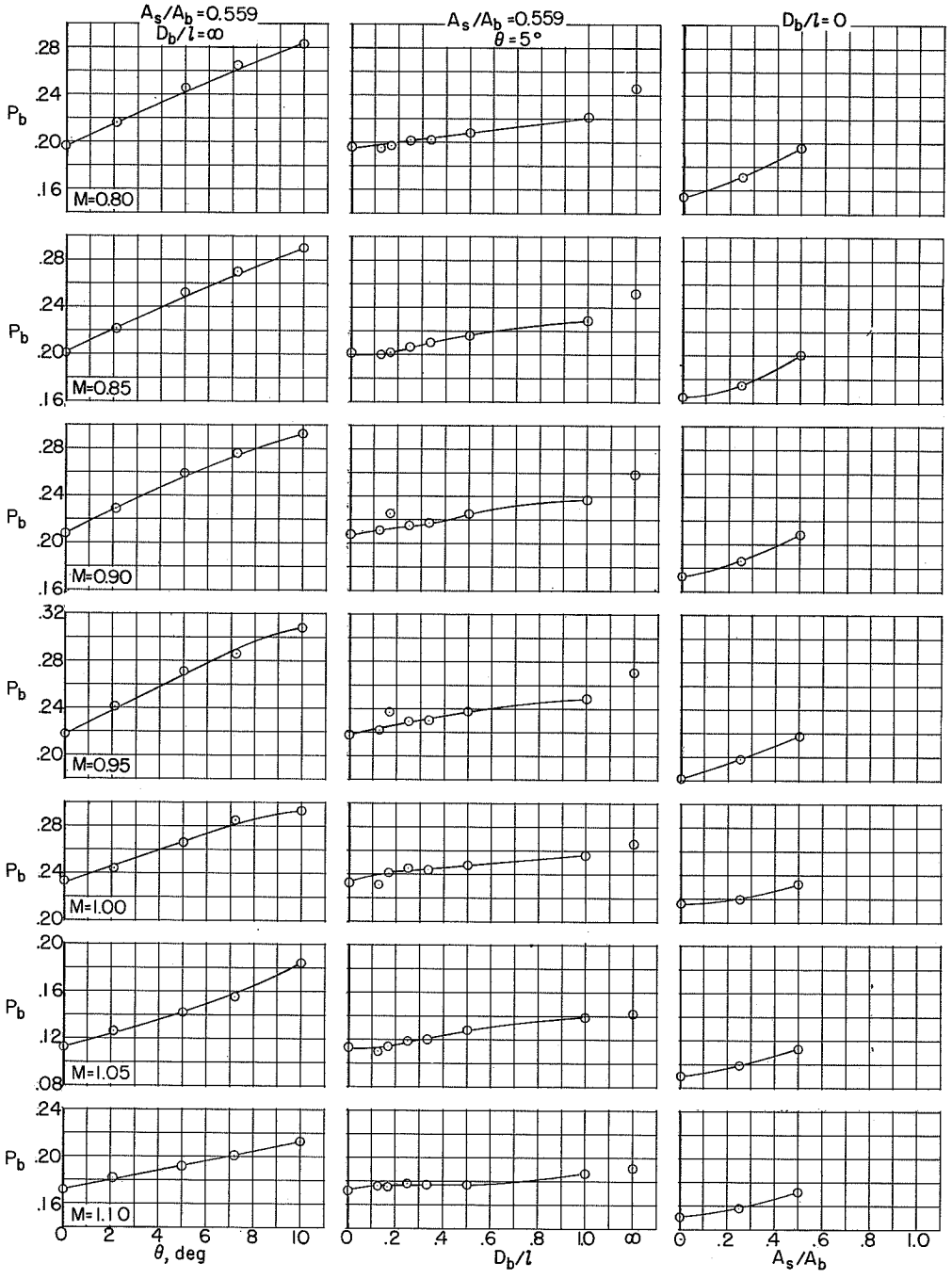

(b) Afterbody I. $\beta = 16^\circ$; $\frac{D_b}{D_m} = 0.334$.

Figure 7.- Continued.

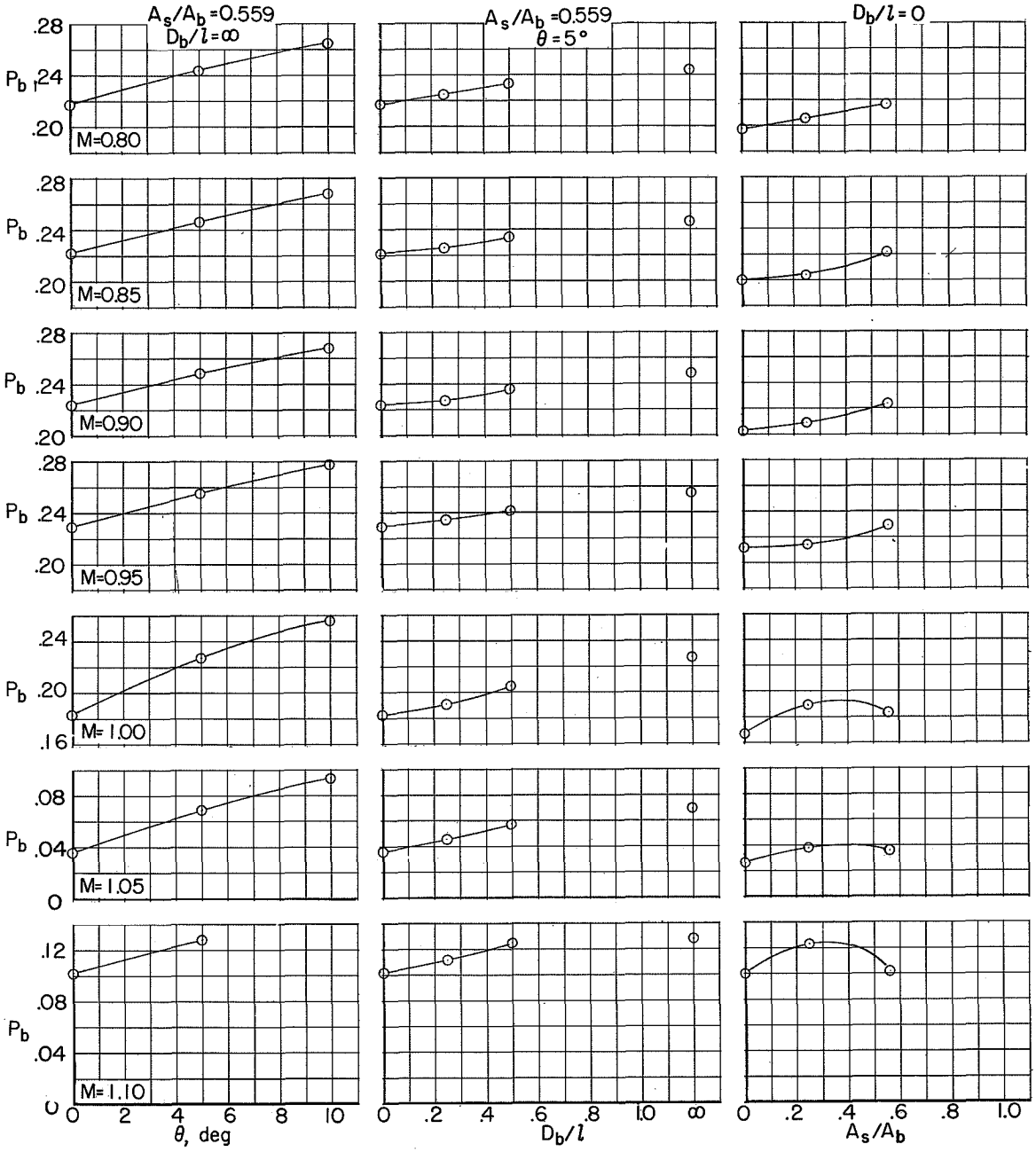

(c) Afterbody II. $\beta = 24^{\circ}$; $\frac{D_b}{D_m} = 0.334$.

Figure 7.- Continued.

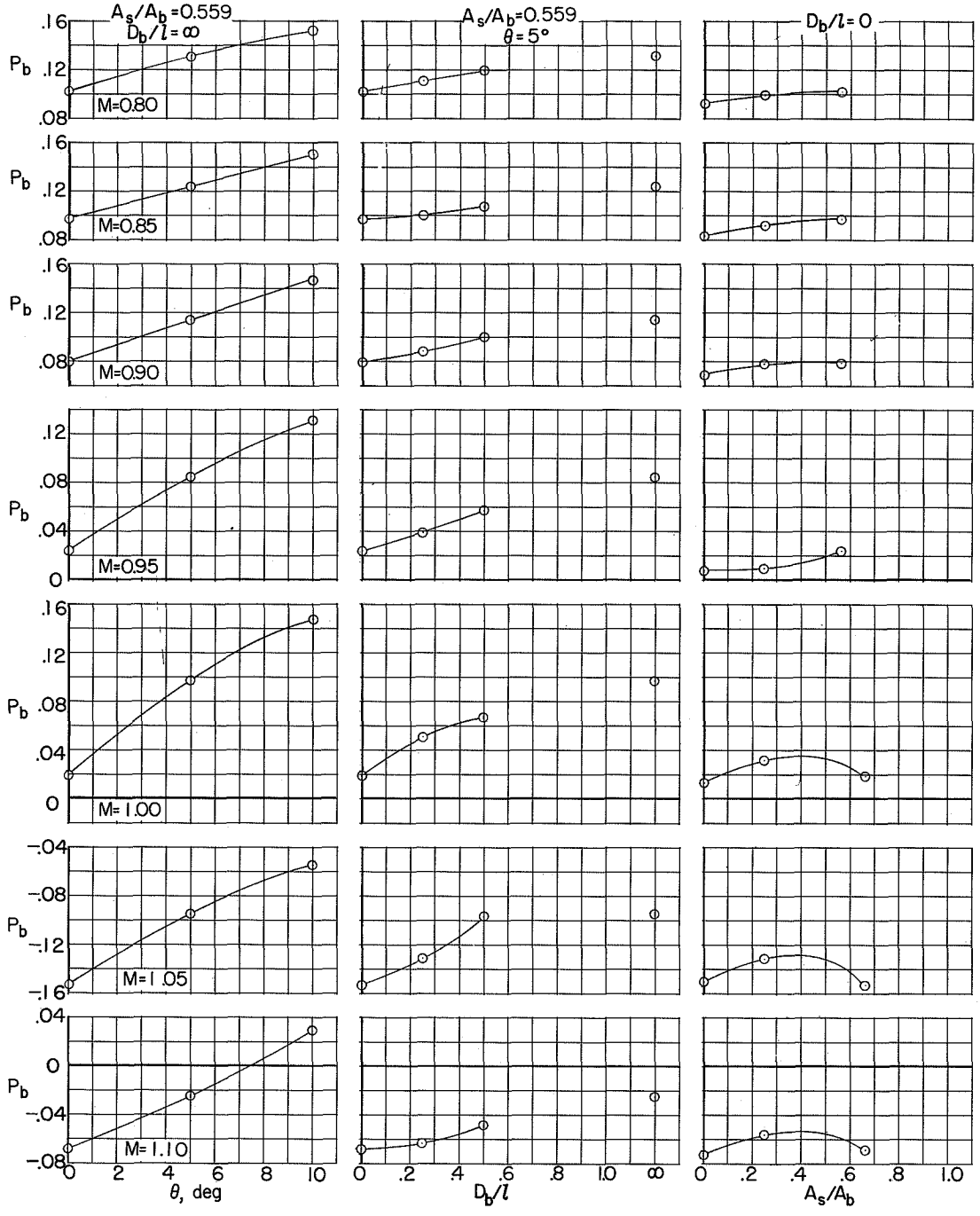

(d) Afterbody III. $\beta = 45^\circ$; $\frac{D_b}{D_m} = 0.334$.

Figure 7.- Continued.

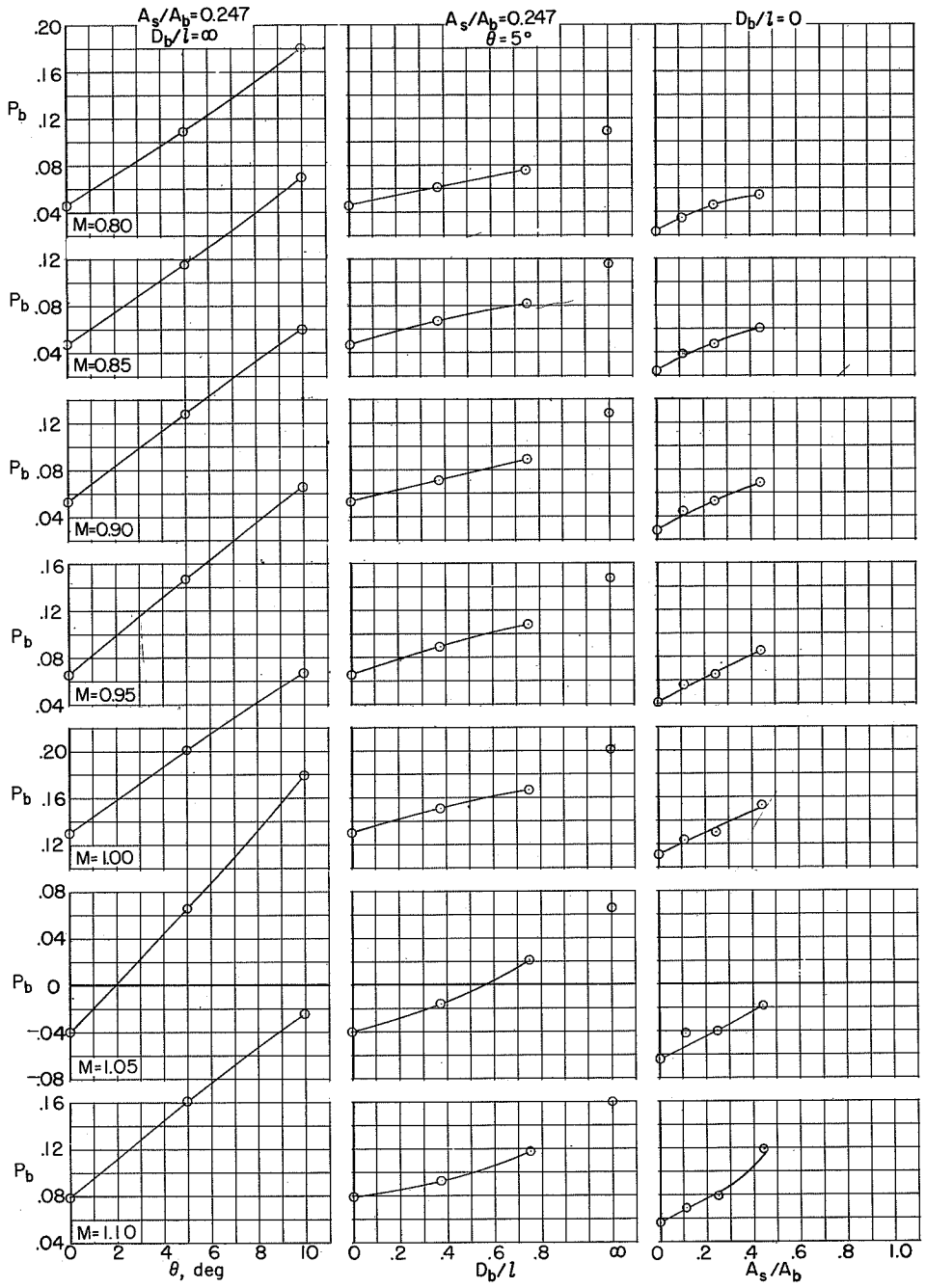

(e) Afterbody IX. $\beta = 7.7^{\circ}$; $\frac{D_b}{D_m} = 0.503$.

Figure 7.- Continued.

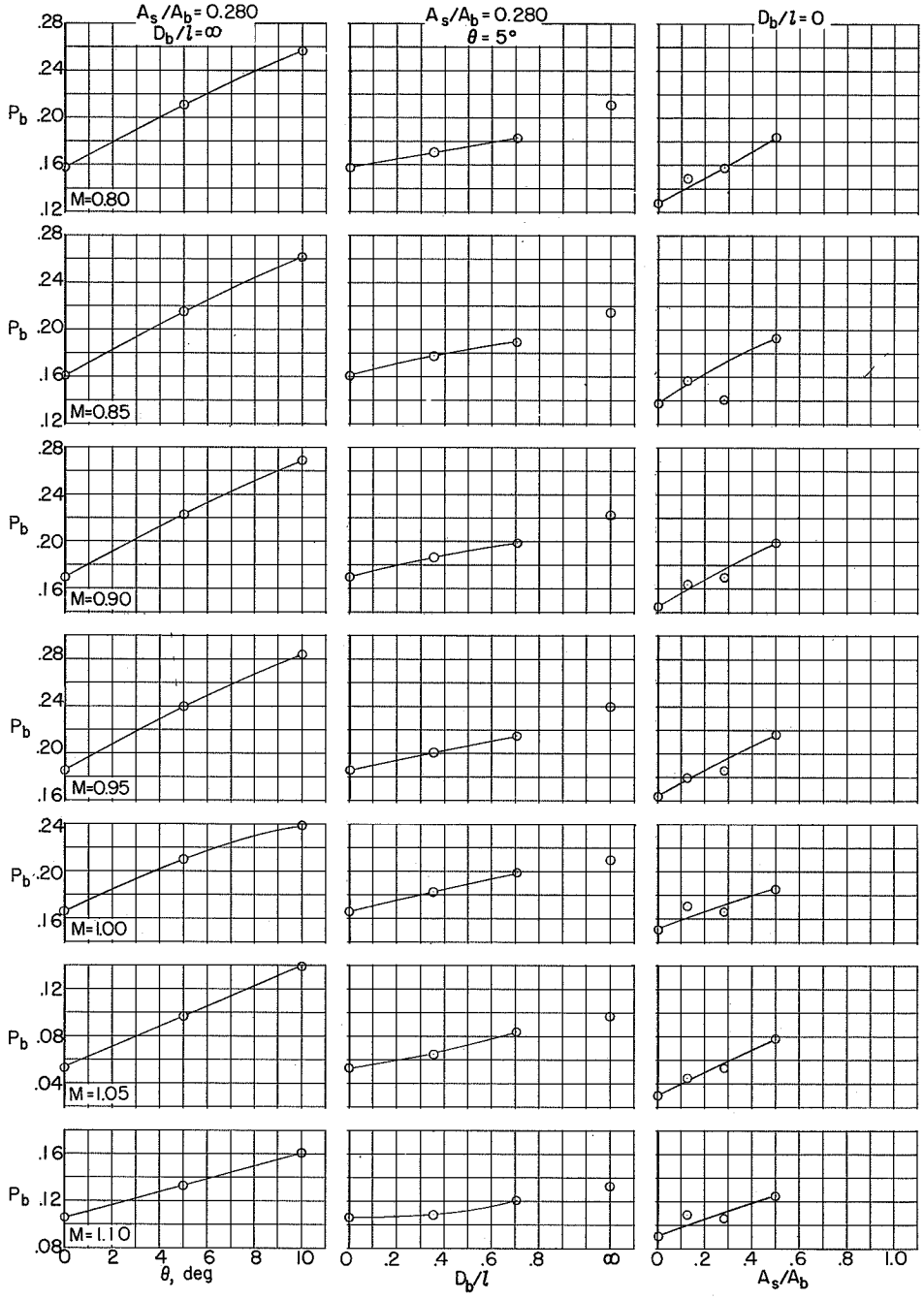

(f) Afterbody IV. $\beta = 16°$; $\frac{D_b}{D_m} = 0.473$.

Figure 7.- Continued.

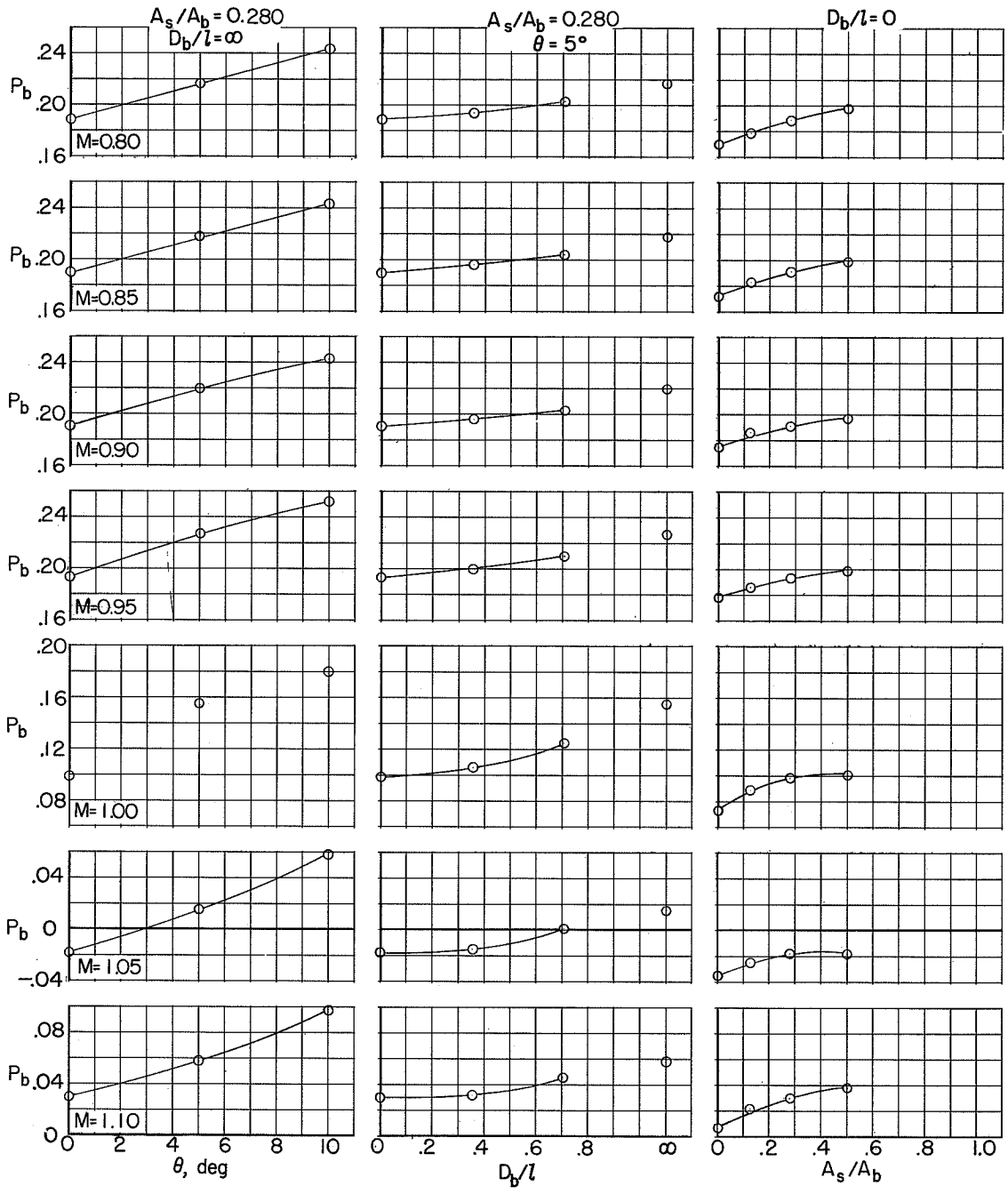

(g) Afterbody V. $\beta = 24°$; $\frac{D_b}{D_m} = 0.473$.

Figure 7.- Continued.

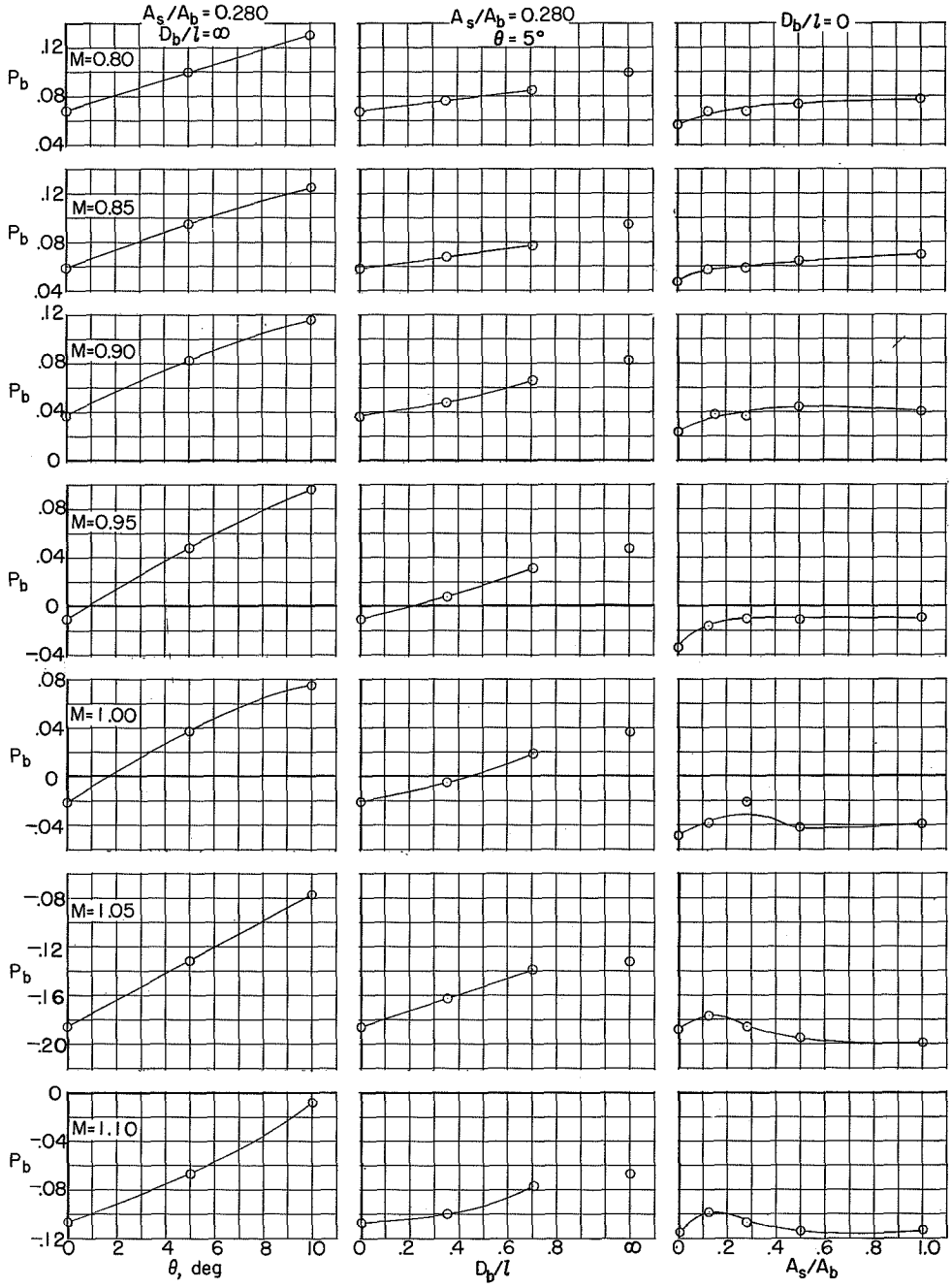

(h) Afterbody VI. $\beta = 45^{\circ}$; $\frac{D_b}{D_m} = 0.473$.

Figure 7.- Concluded.

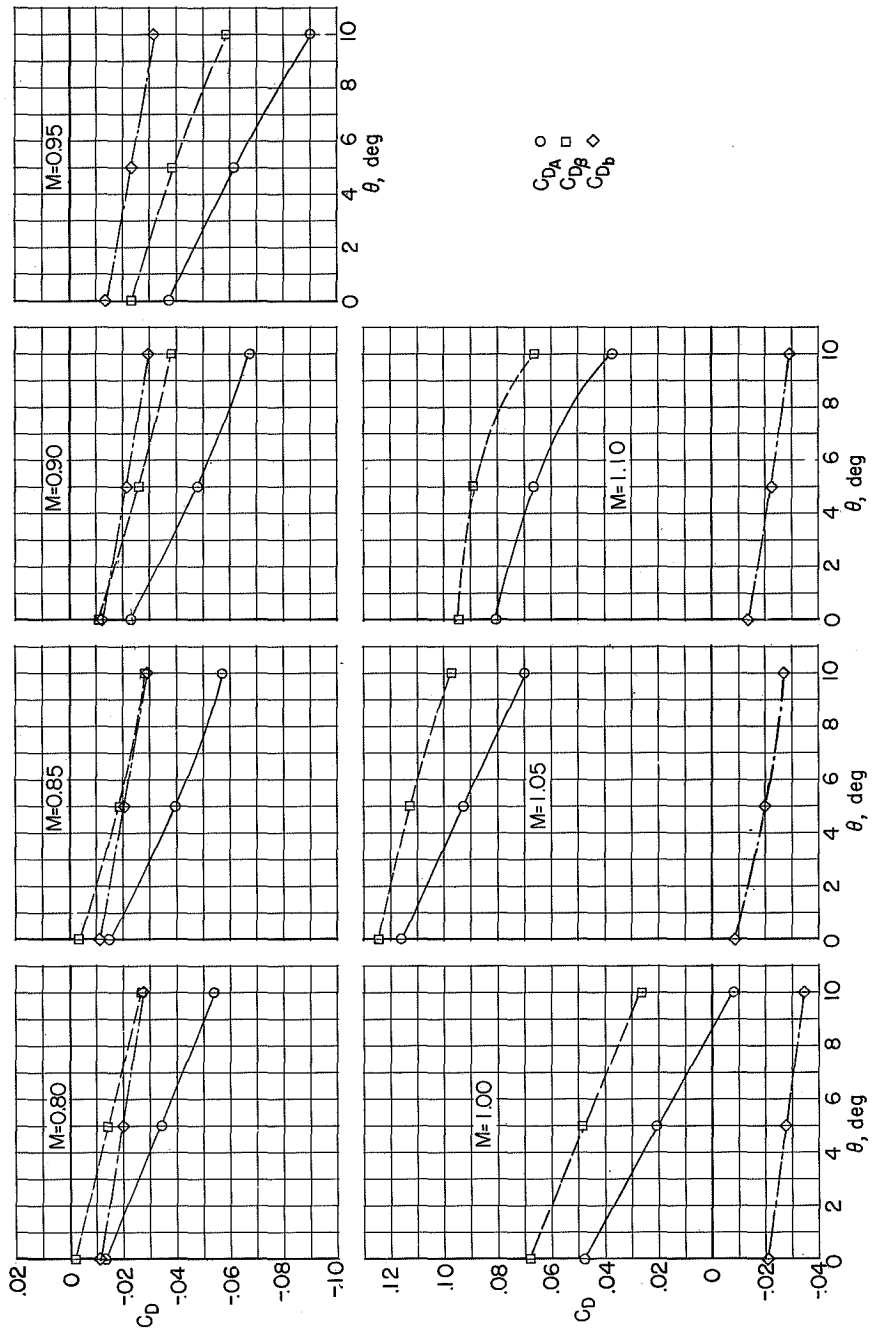

(a) Afterbody XI. $\beta = 8^\circ$; $\frac{A_s}{A_b} = 0.559$; $\frac{D_b}{D_m} = 0.334$.

Figure 8.- Variation of base, boattail, and total afterbody pressure drag coefficient with sting half-angle at different values of stream Mach number and with $\frac{D_b}{l} = \infty$.

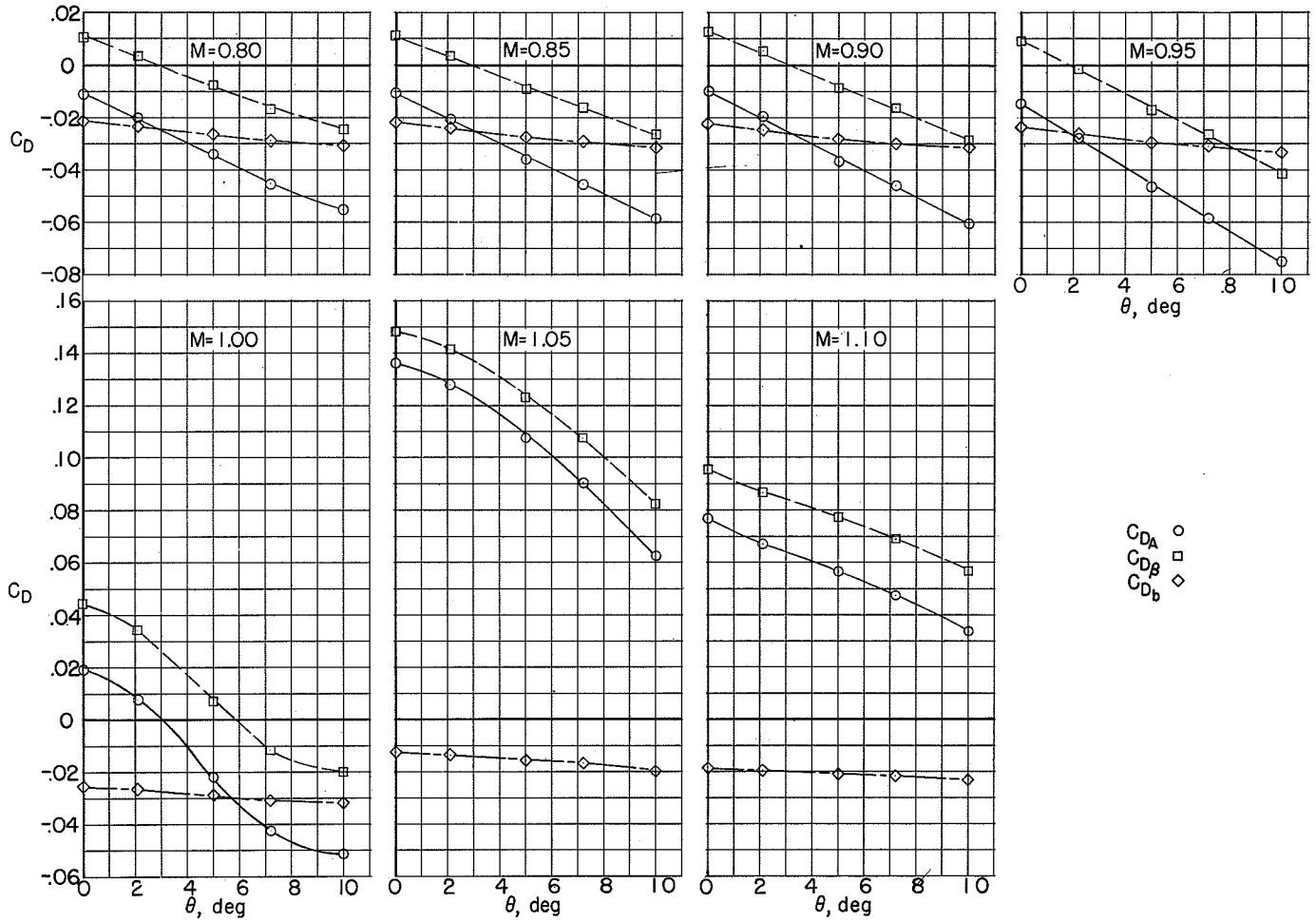

(b) Afterbody I. $\beta = 16^\circ$; $\frac{A_s}{A_b} = 0.559$; $\frac{D_b}{D_m} = 0.334$.

Figure 8.- Continued.

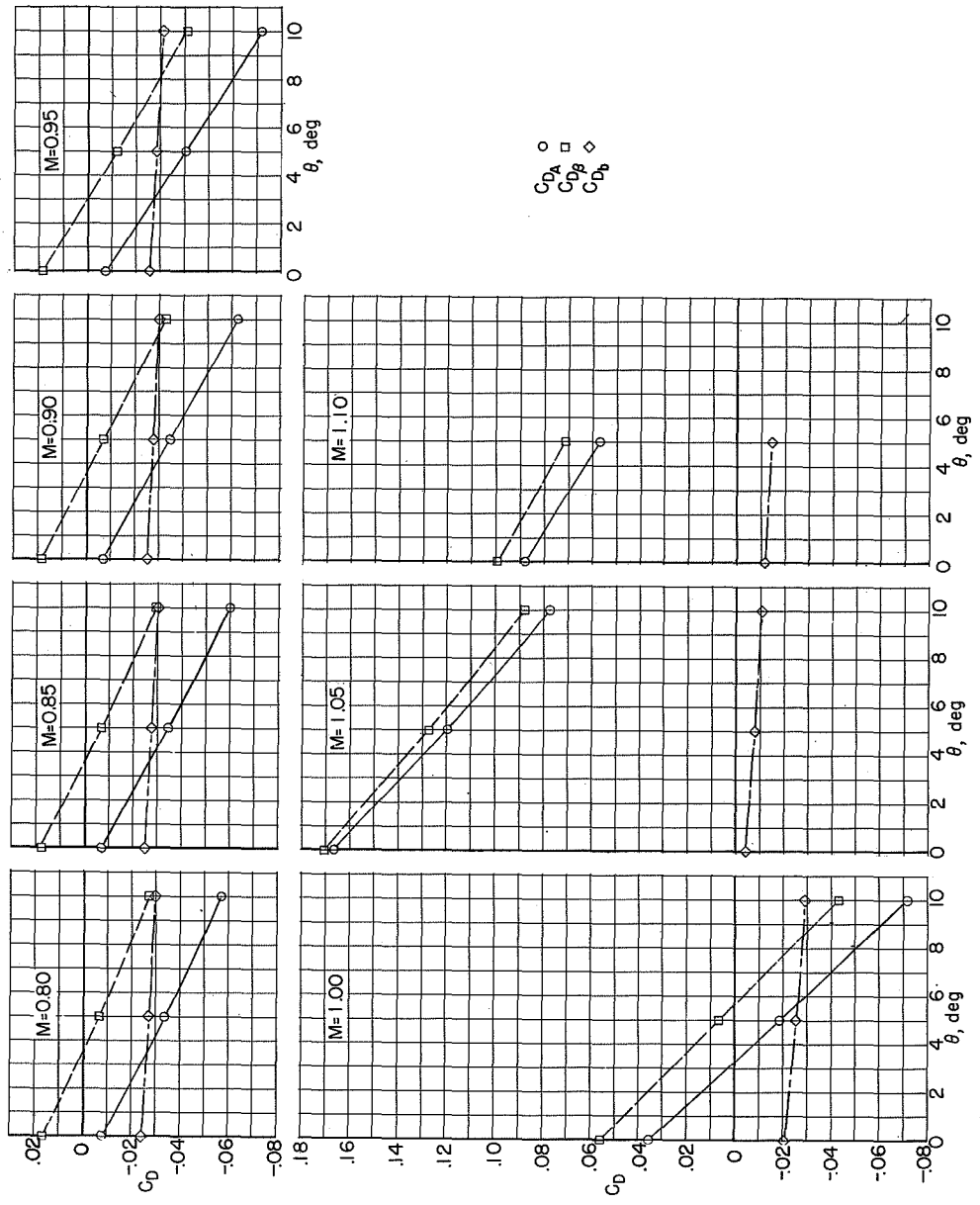

(c) Afterbody II. $\beta = 24^\circ$; $\frac{A_s}{A_b} = 0.559$; $\frac{D_b}{D_m} = 0.334$.

Figure 8.- Continued.

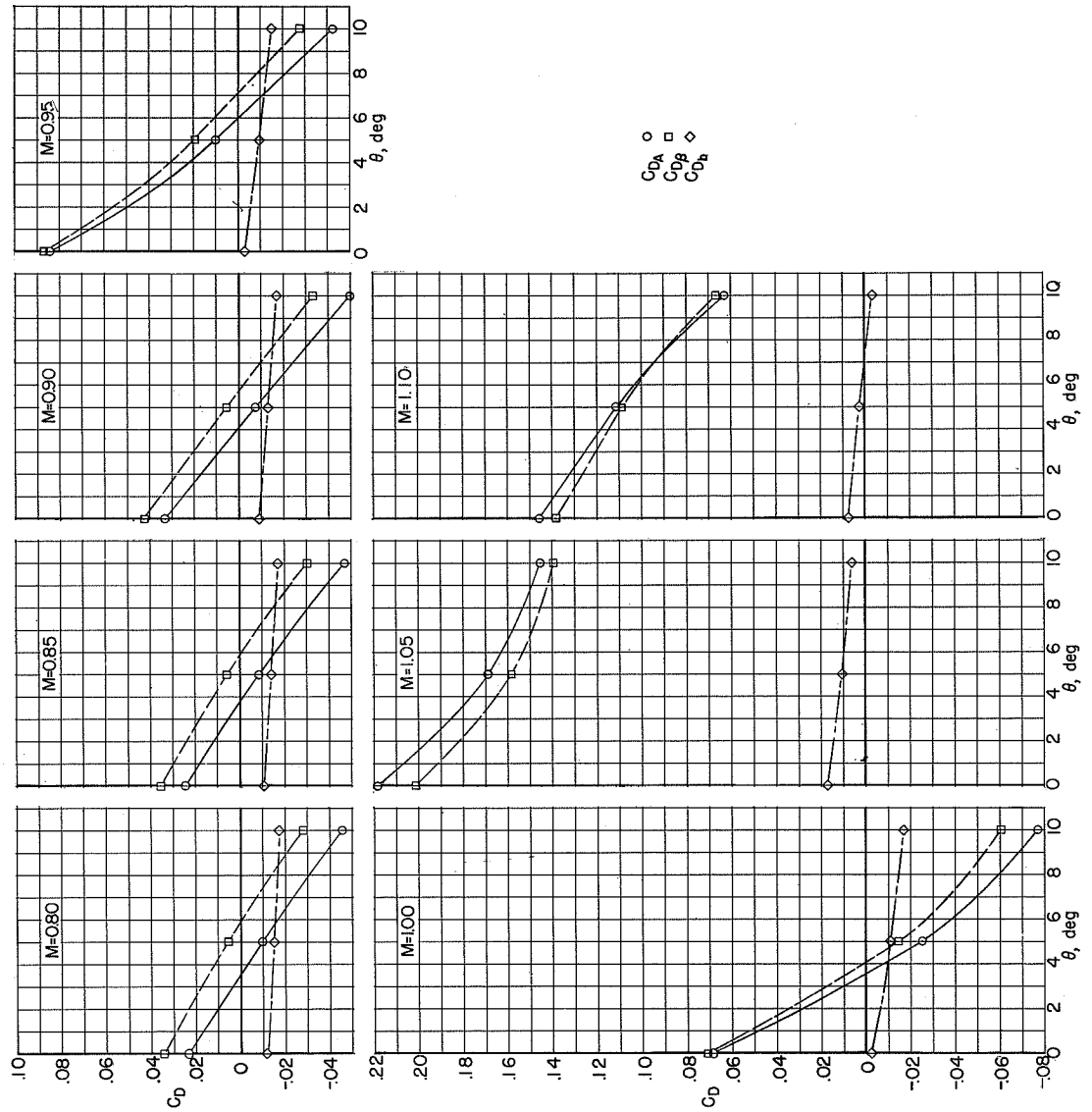

(d) Afterbody III. $\beta = 24^{\circ}$; $\frac{A_s}{A_b} = 0.559$; $\frac{D_b}{D_m} = 0.334$.

Figure 8.- Continued.

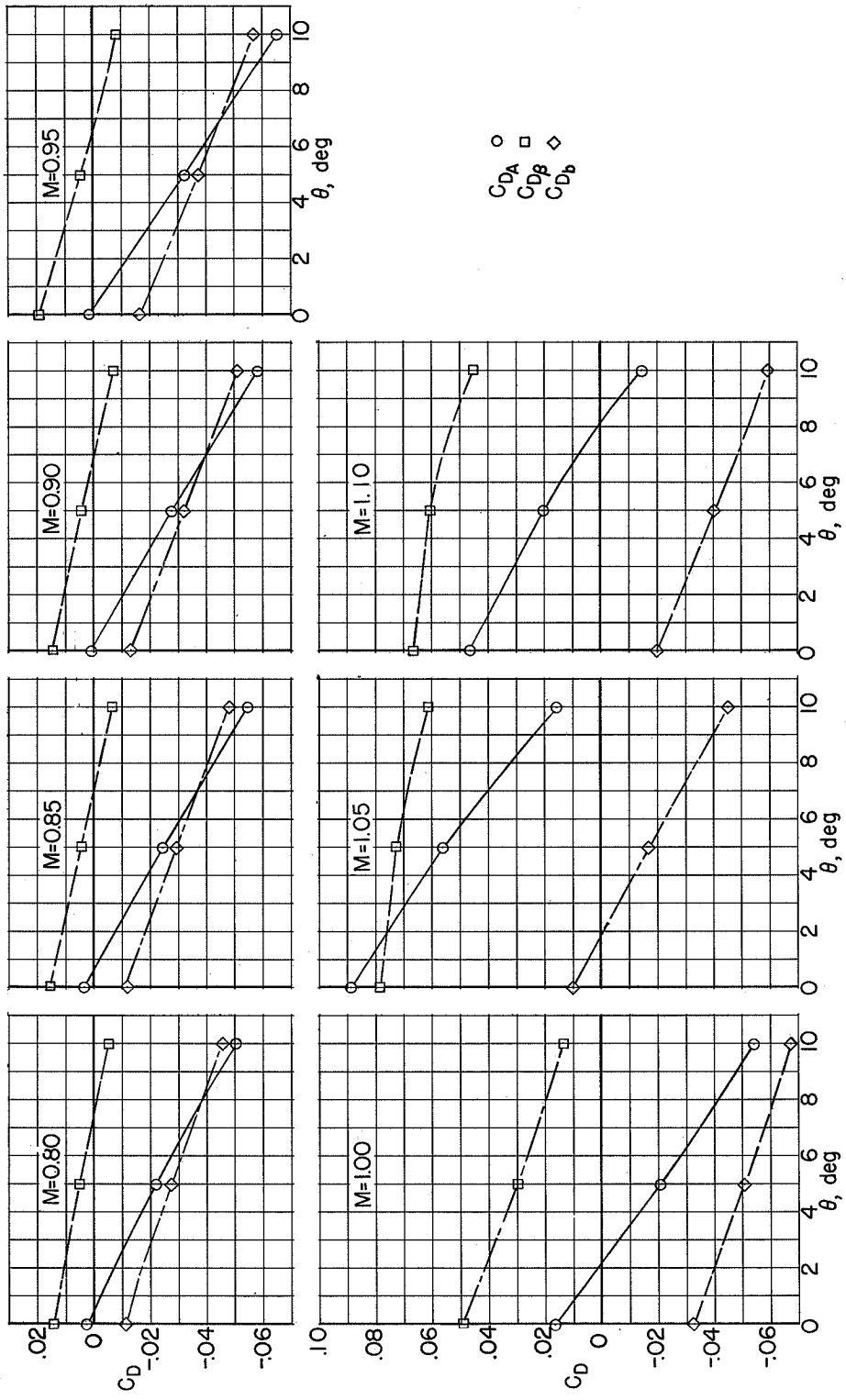

(e) Afterbody IX. $\beta = 7.7°$; $\frac{A_s}{A_b} = 0.247$; $\frac{D_b}{D_m} = 0.503$.

Figure 8.- Continued.

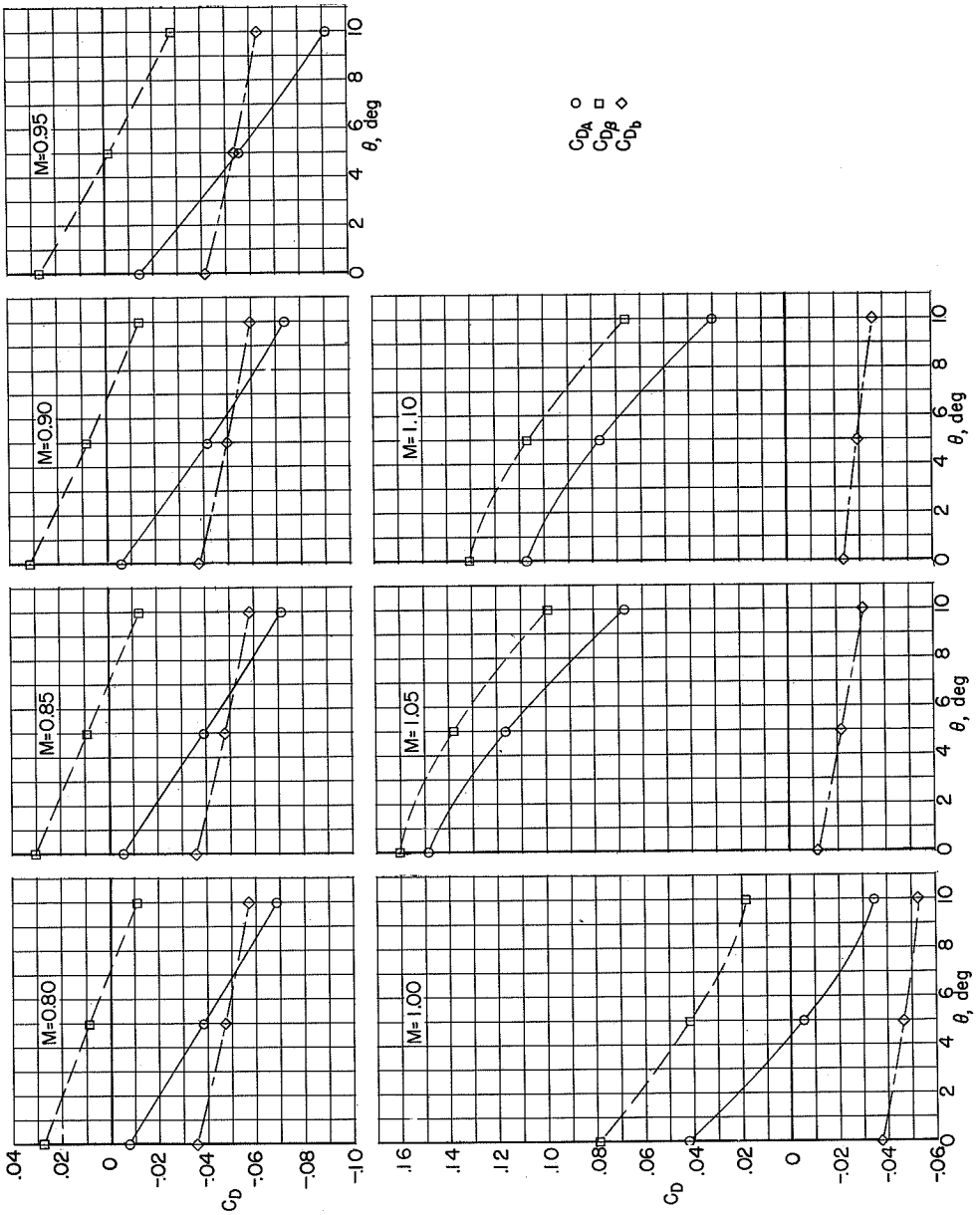

(f) Afterbody IV. $\beta = 16^\circ$; $\frac{A_s}{A_b} = 0.280$; $\frac{D_b}{D_m} = 0.473$.

Figure 8.- Continued.

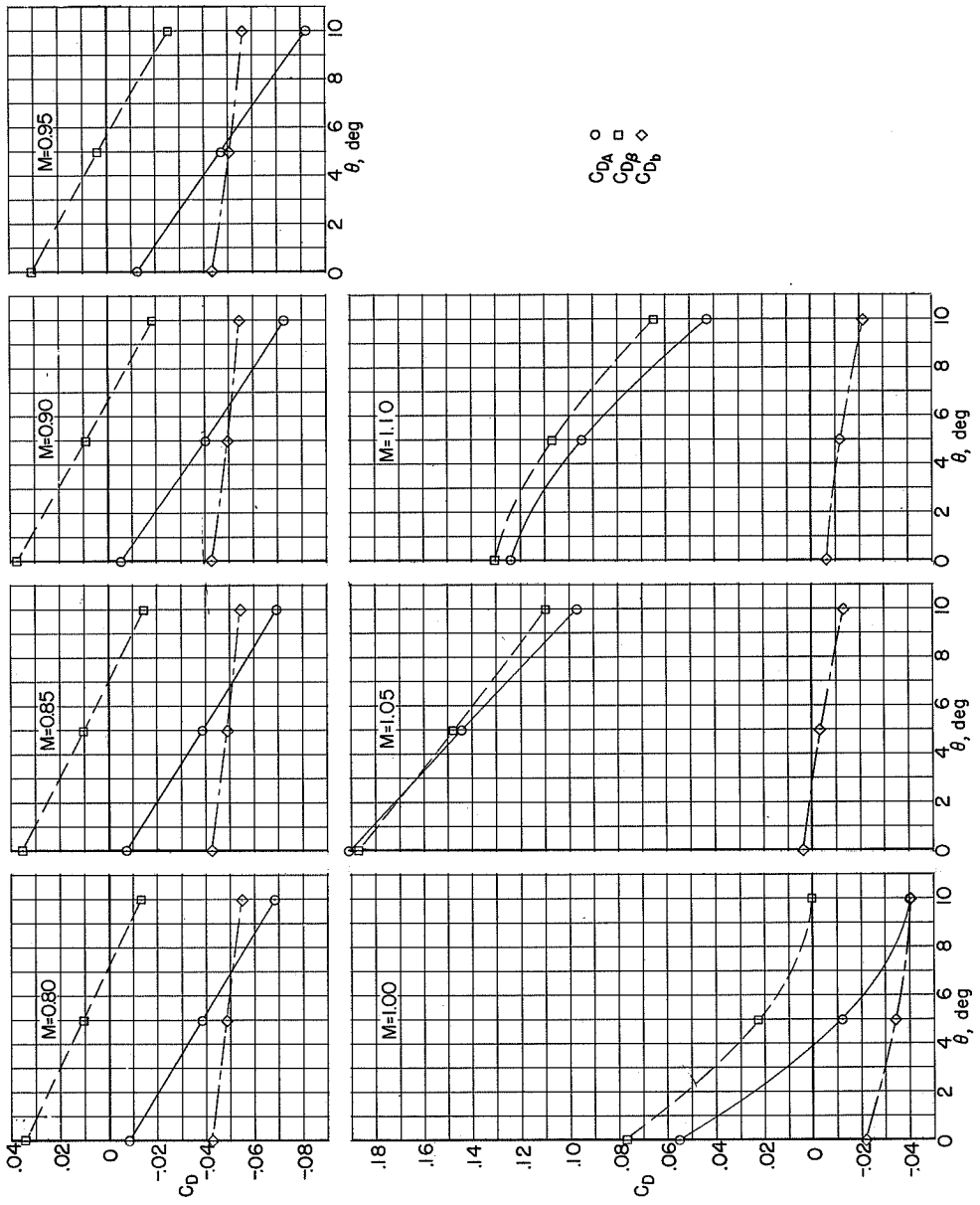

(g) Afterbody V. $\beta = 24^\circ$; $\frac{A_s}{A_b} = 0.280$; $\frac{D_b}{D_m} = 0.473$.

Figure 8.- Continued.

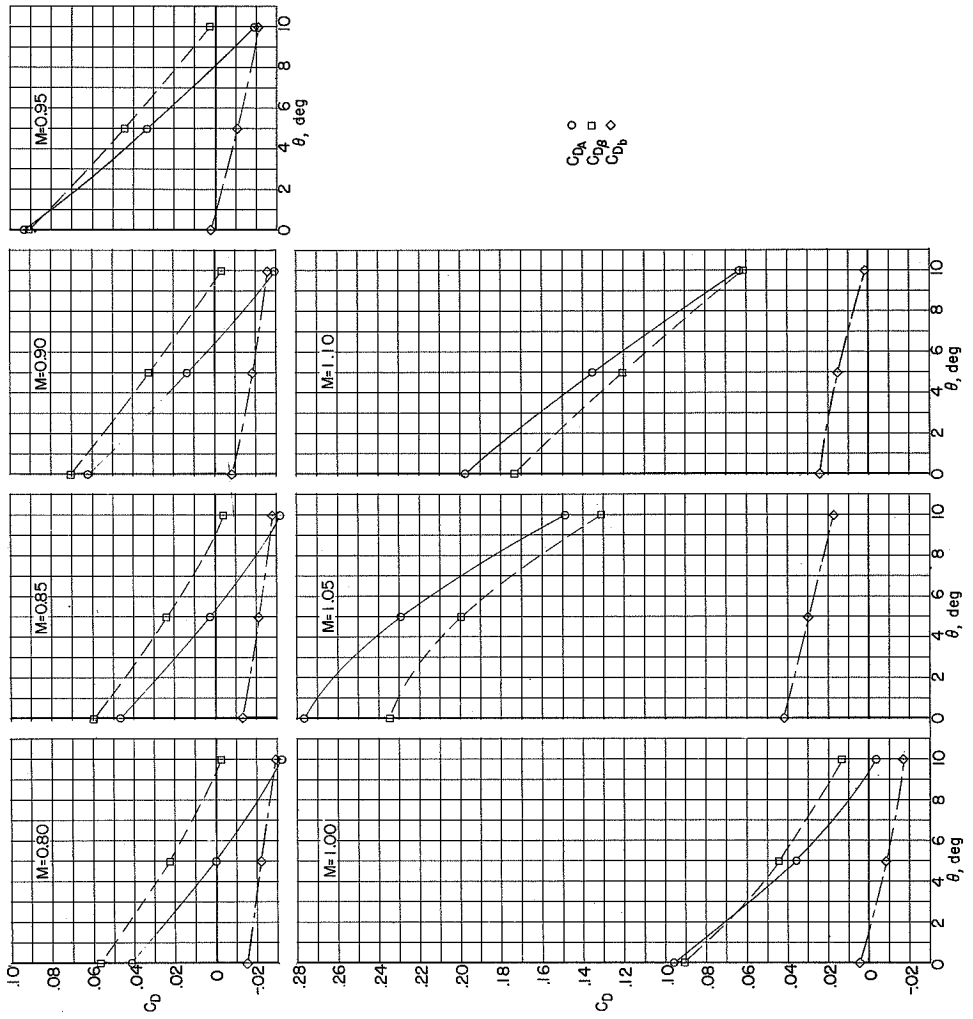

(h) Afterbody VI. $\beta = 45°$; $\frac{A_s}{A_b} = 0.280$; $\frac{D_b}{D_m} = 0.473$.

Figure 8.- Concluded.

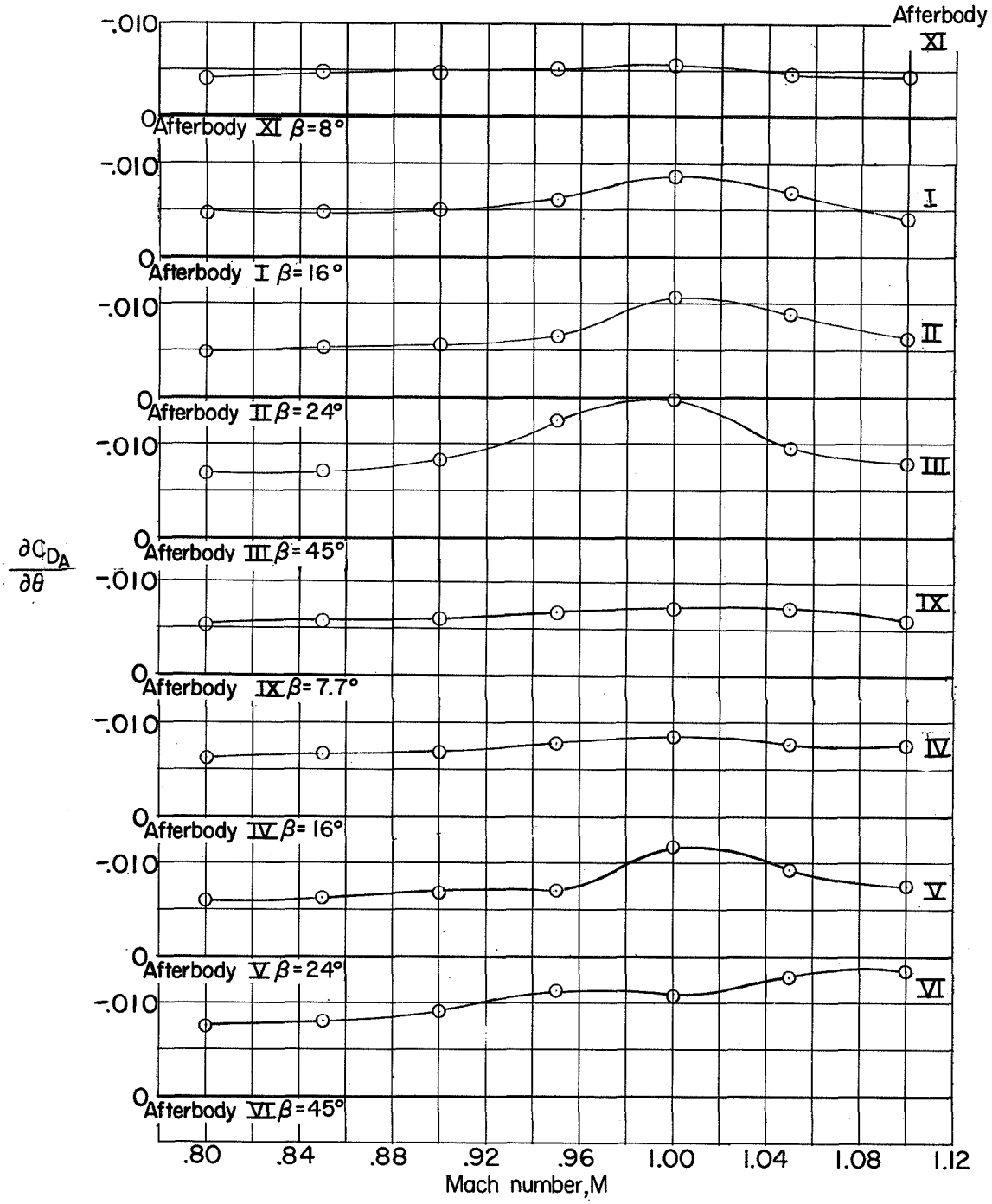

Figure 9.- Variation of sting-half-angle effect with Mach number. $D_b/l = \infty$.

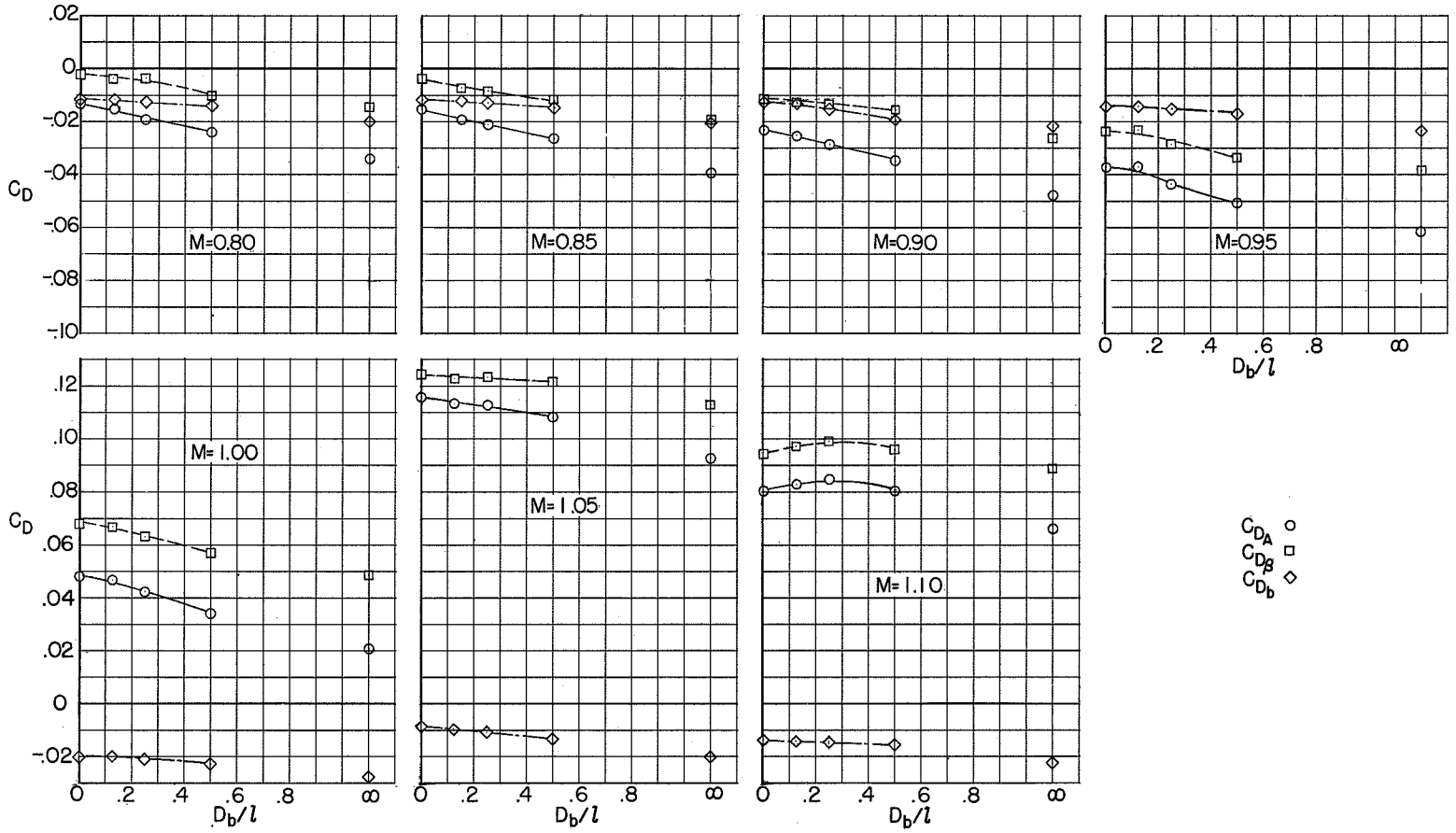

(a) Afterbody XI. $\beta = 8^\circ$; $\frac{A_s}{A_b} = 0.559$; $\frac{D_b}{D_m} = 0.334$.

Figure 10.- Variation of base, boattail, and total afterbody pressure drag coefficient with ratio of base diameter to sting length at different values of stream Mach number with $\theta = 5^\circ$.

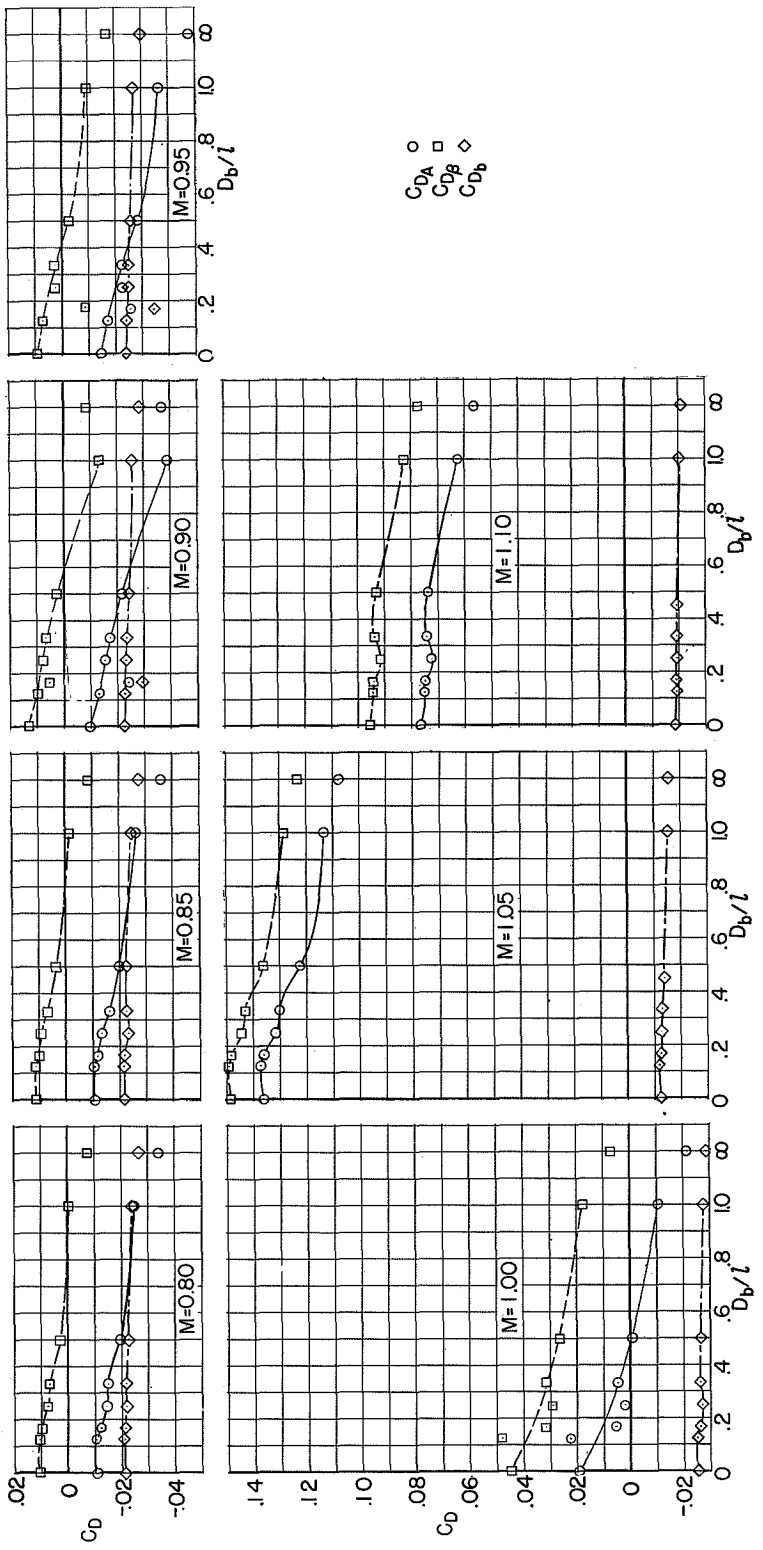

(b) Afterbody I. $\beta = 16^\circ$; $\frac{A_s}{A_b} = 0.559$; $\frac{D_b}{D_m} = 0.334$.

Figure 10.- Continued.

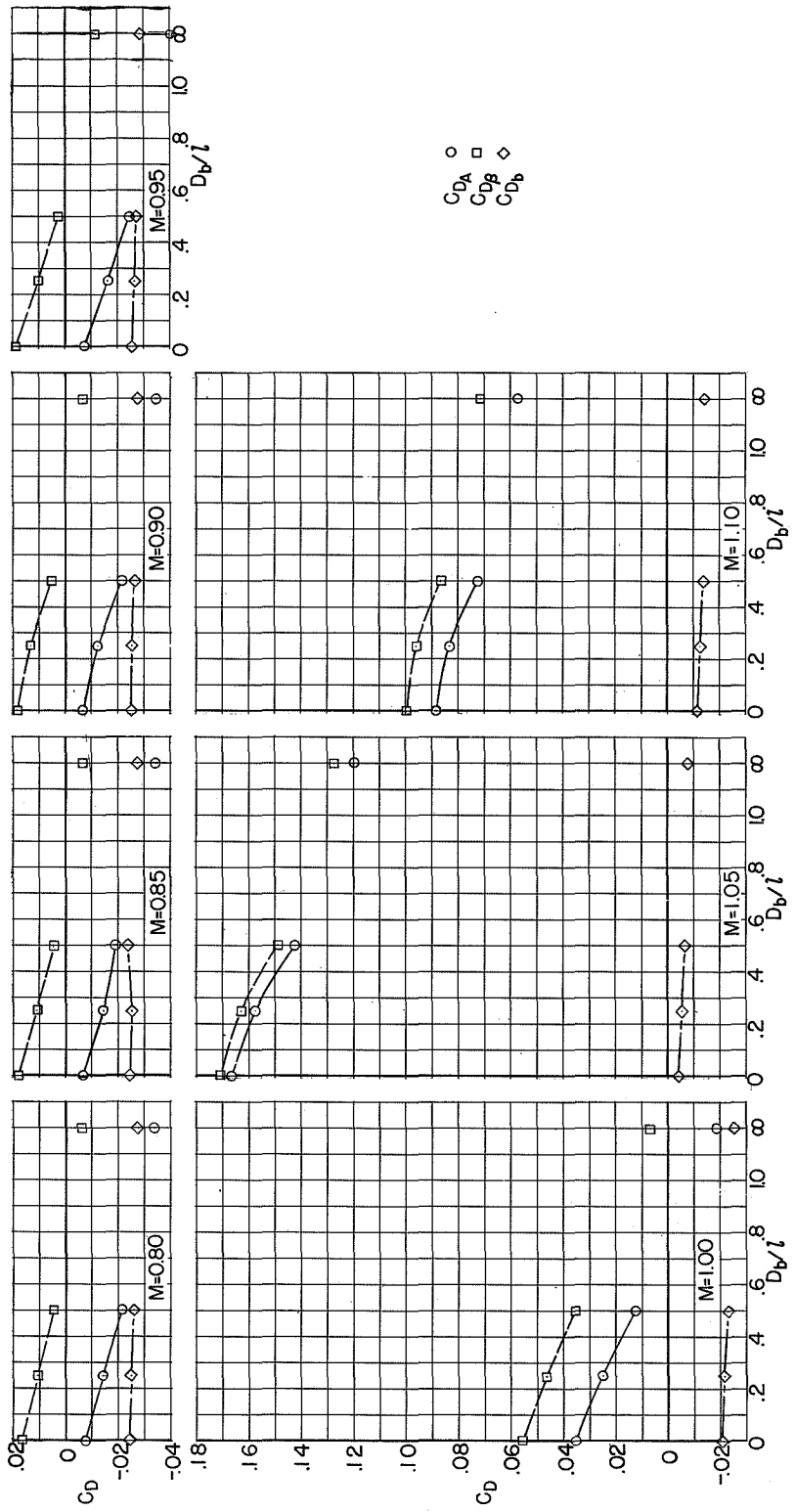

(c) Afterbody II. $\beta = 24^\circ$; $\frac{A_s}{A_b} = 0.559$; $\frac{D_b}{D_m} = 0.334$.

Figure 10.- Continued.

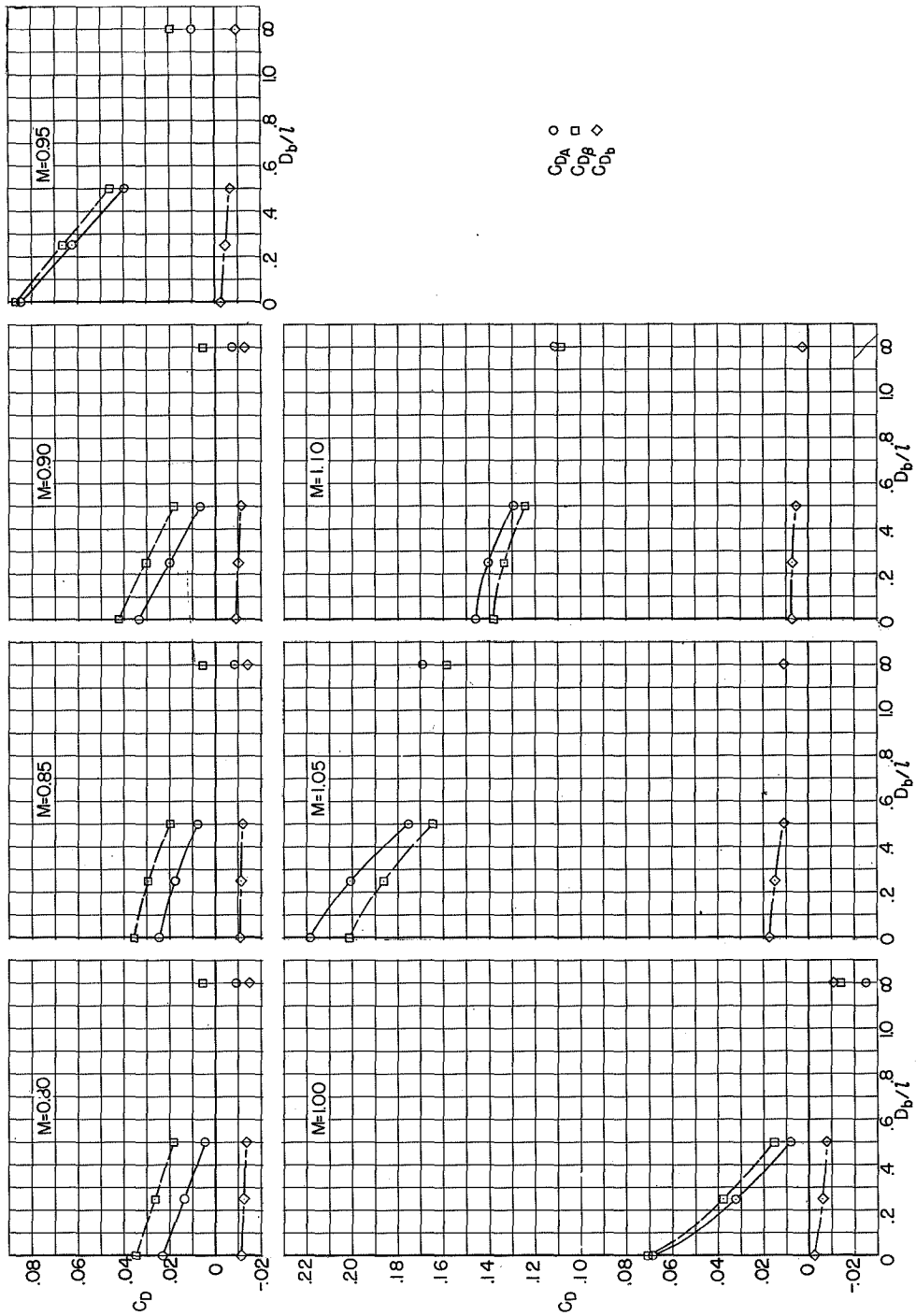

(d) Afterbody III. $\beta = 45^\circ$; $\frac{A_s}{A_b} = 0.559$; $\frac{D_b}{D_m} = 0.334$.

Figure 10.- Continued.

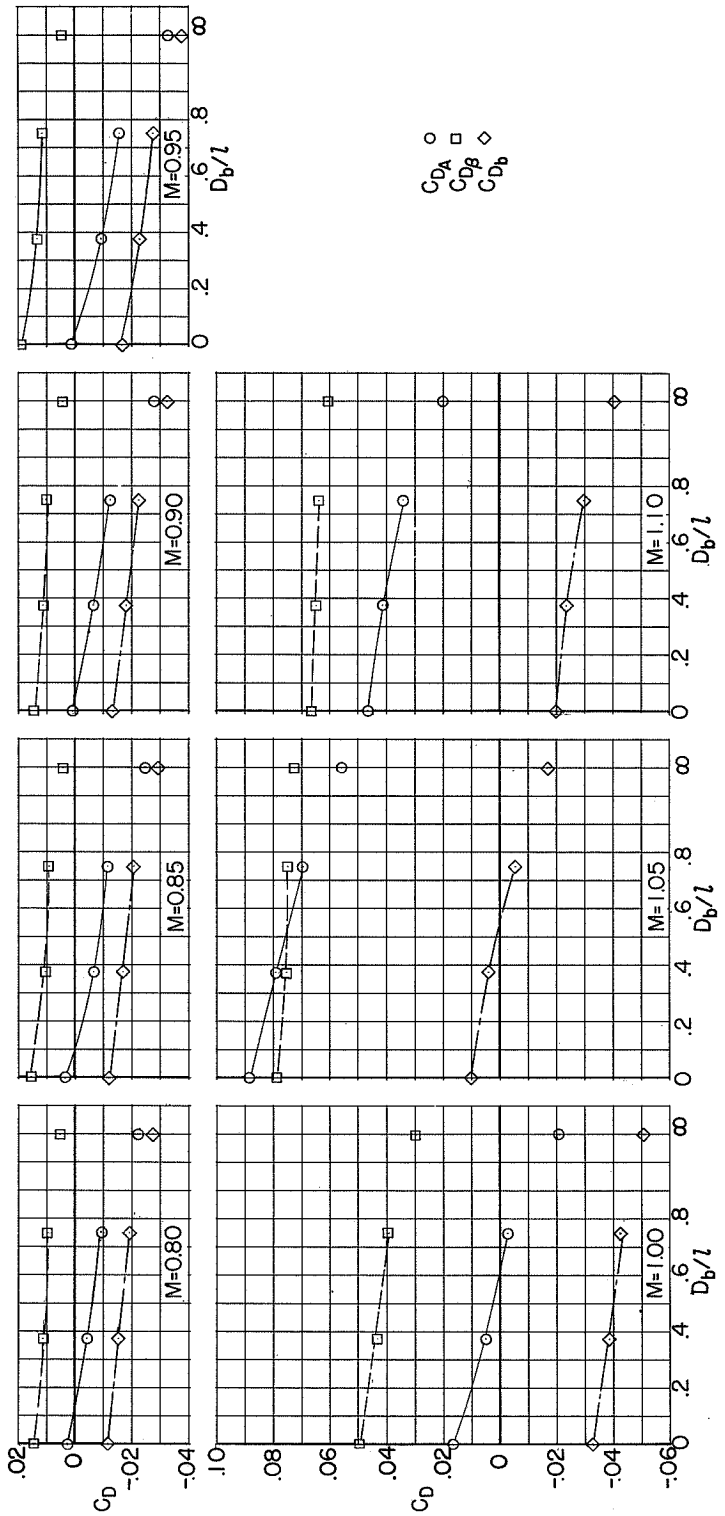

(e) Afterbody IX. $\beta = 7.7^\circ$; $\frac{A_s}{A_b} = 0.247$; $\frac{D_b}{D_m} = 0.503$.

Figure 10.- Continued.

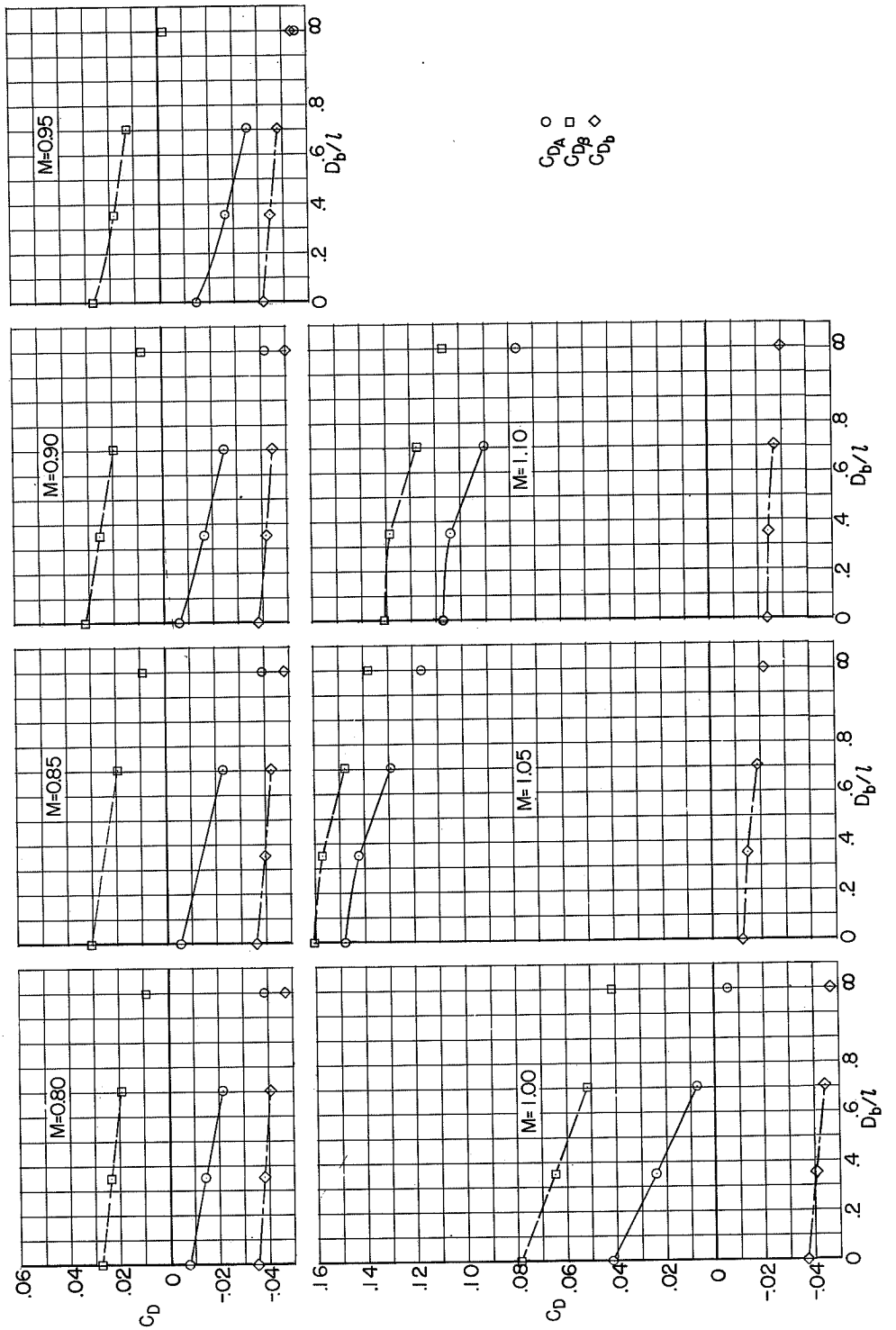

(f) Afterbody IV. $\beta = 16^\circ$; $\frac{A_s}{A_b} = 0.280$; $\frac{D_b}{D_m} = 0.473$.

Figure 10.- Continued.

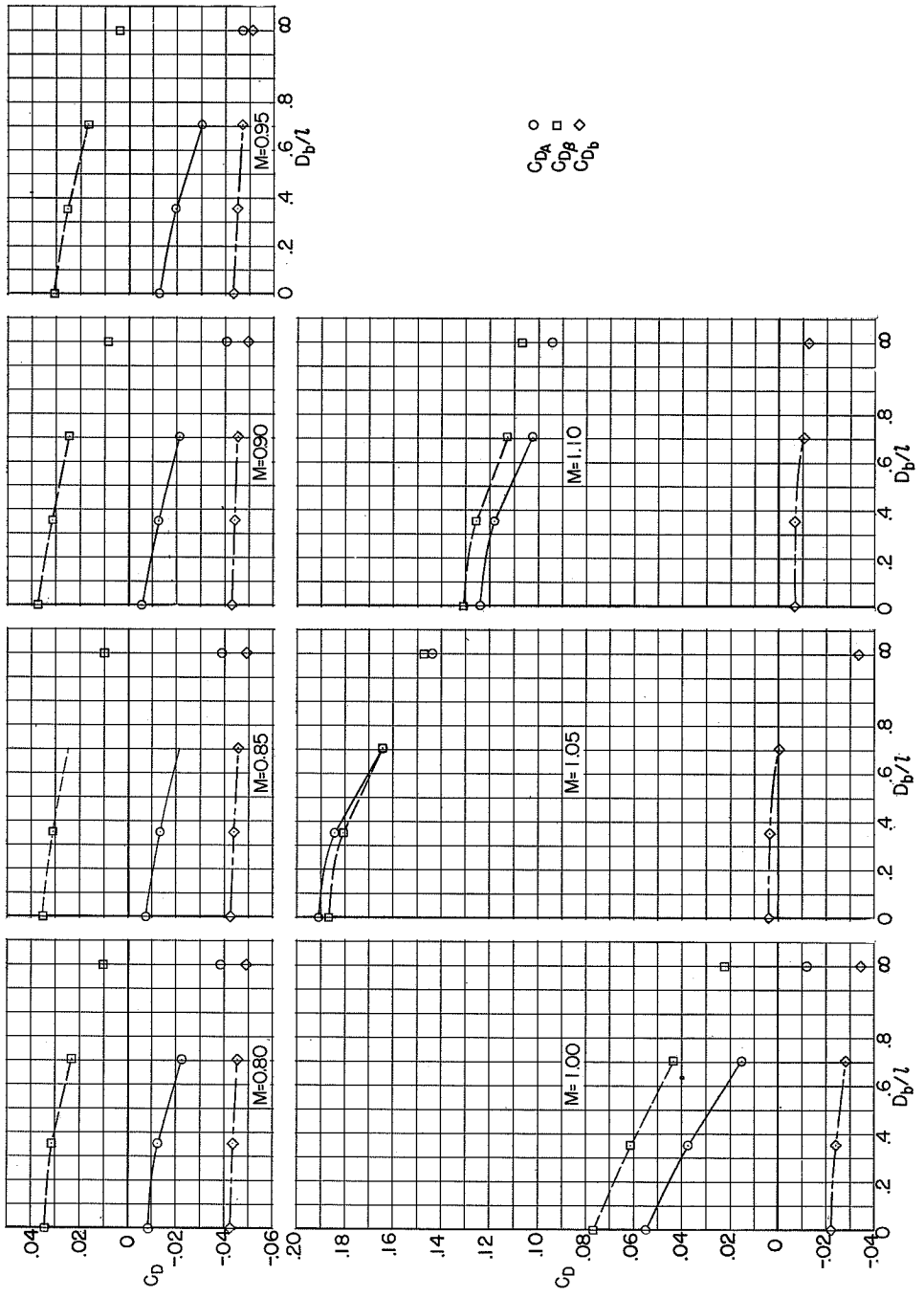

(g) Afterbody V. $\beta = 24^\circ$; $\frac{A_s}{A_b} = 0.280$; $\frac{D_b}{D_m} = 0.473$.

Figure 10.- Continued.

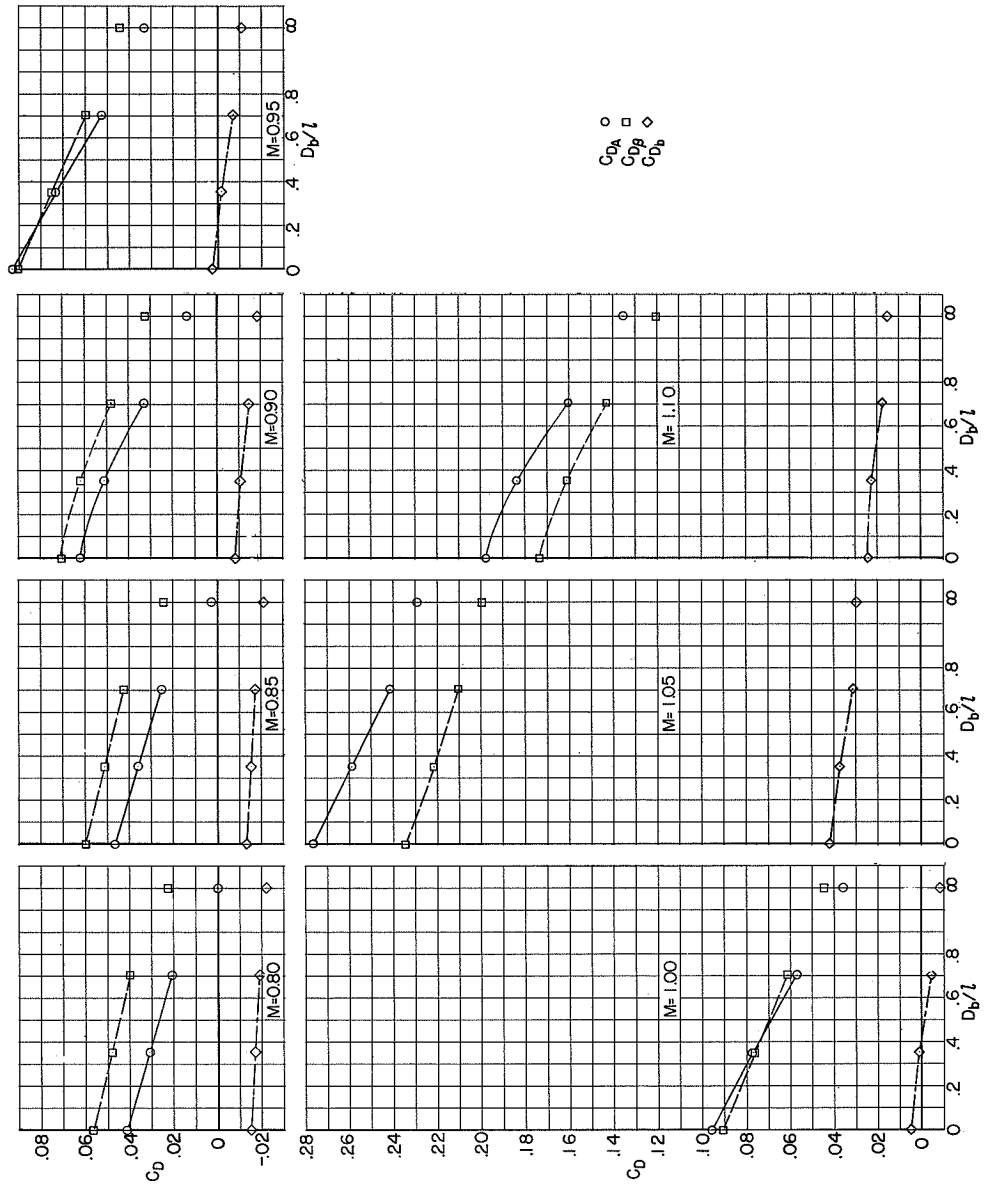

(h) Afterbody VI. $\beta = 45^\circ$; $\frac{A_s}{A_b} = 0.280$; $\frac{D_b}{D_m} = 0.473$.

Figure 10.- Concluded.

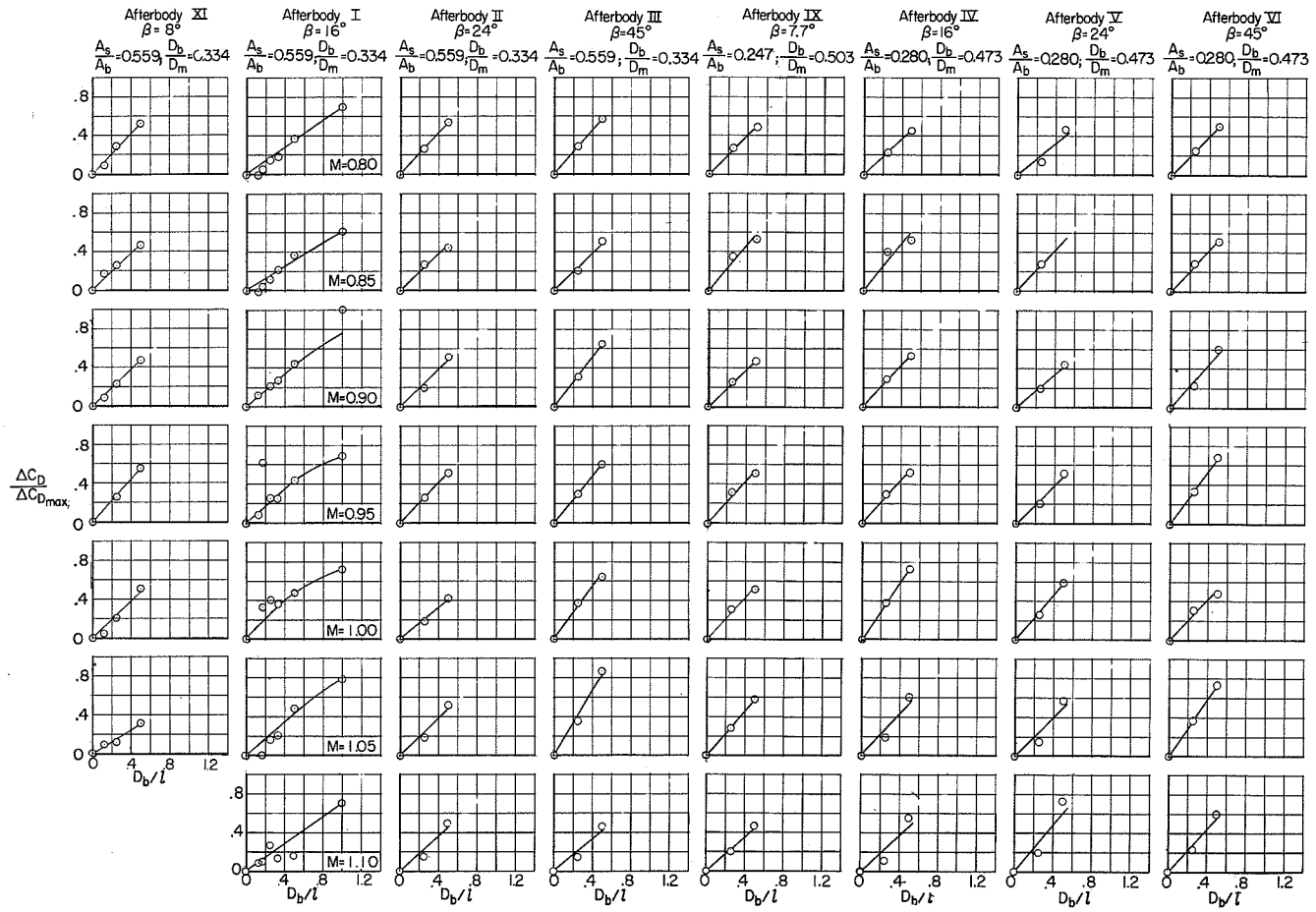

(a) Variation of $\Delta C_D/\Delta C_{D_{max}}$ with ratio of base diameter to sting length.

Figure 11.- Sting length effect at different values of free-stream Mach number with $\theta = 5^\circ$.

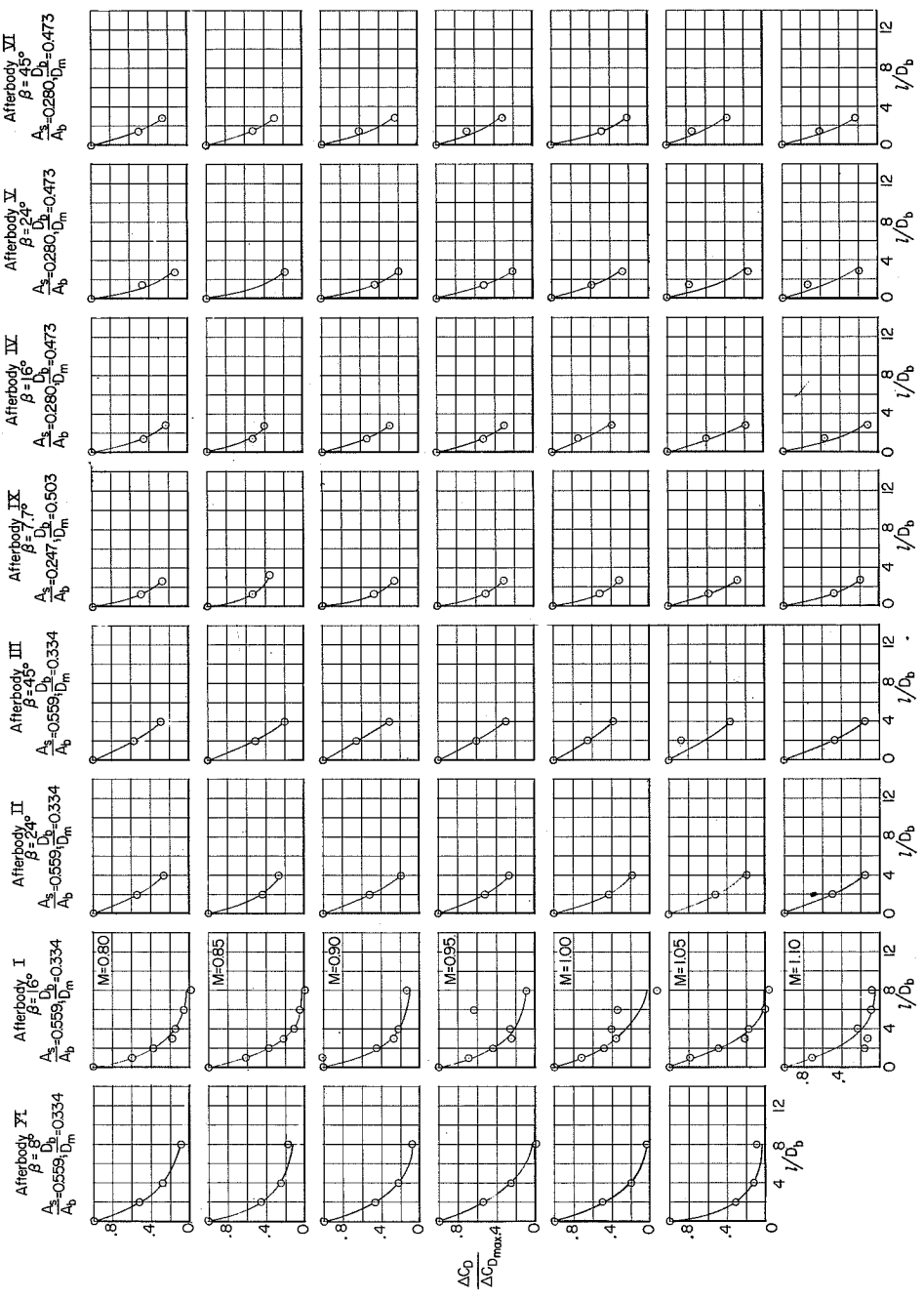

(b) Variation of $\Delta C_D/\Delta C_{D_{max}}$ with ratio of sting length to base diameter.

Figure 11.- Concluded.

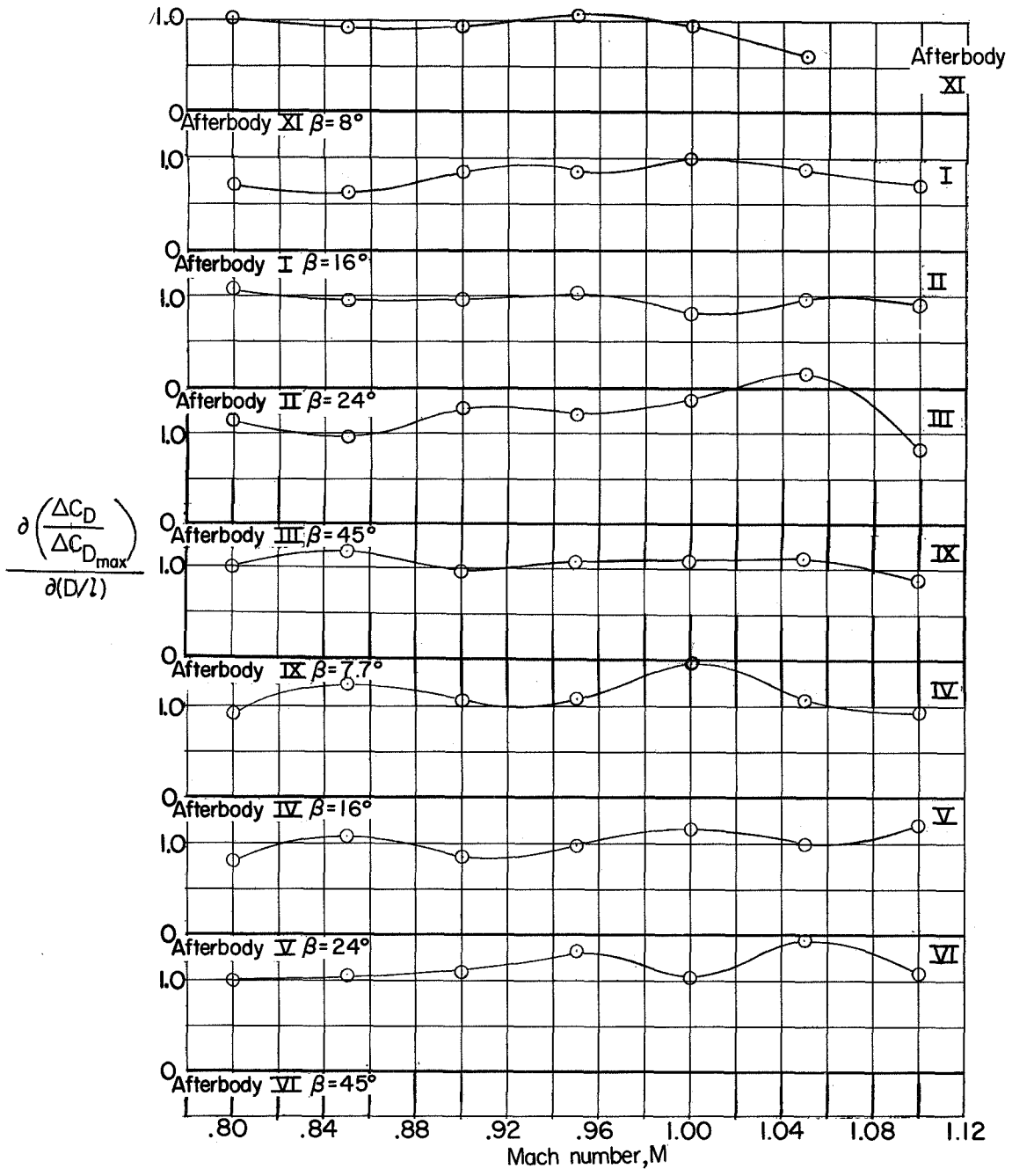

Figure 12.- Variation of sting length effect with Mach number. $\theta = 5^{\circ}$.

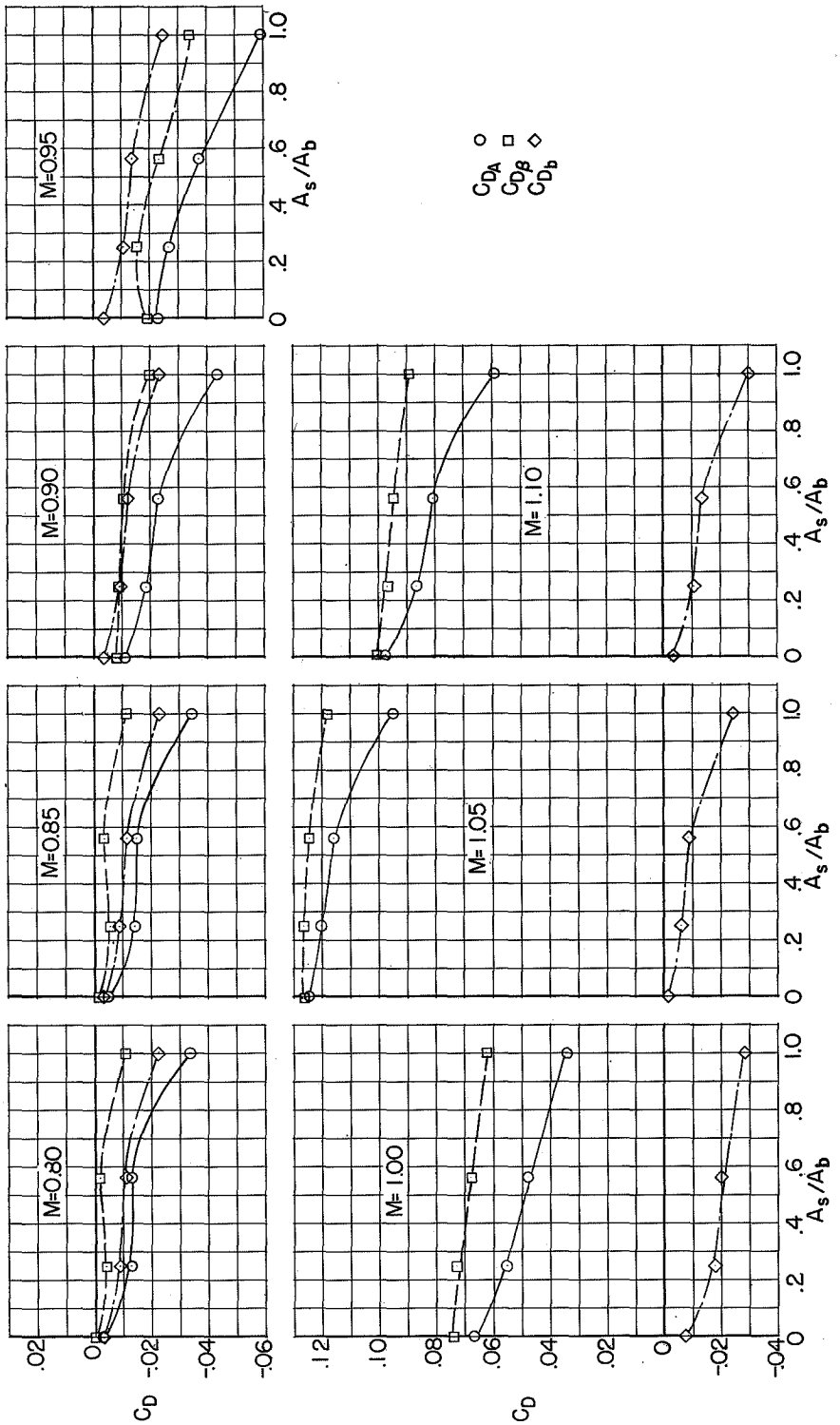

(a) Afterbody XI. $\beta = 8^\circ$; $\frac{D_b}{D_m} = 0.334$.

Figure 13.- Variation of base, boattail, and total afterbody pressure drag coefficient with ratio of sting to base area at different values of stream Mach number and with $\frac{D_b}{l} = 0$.

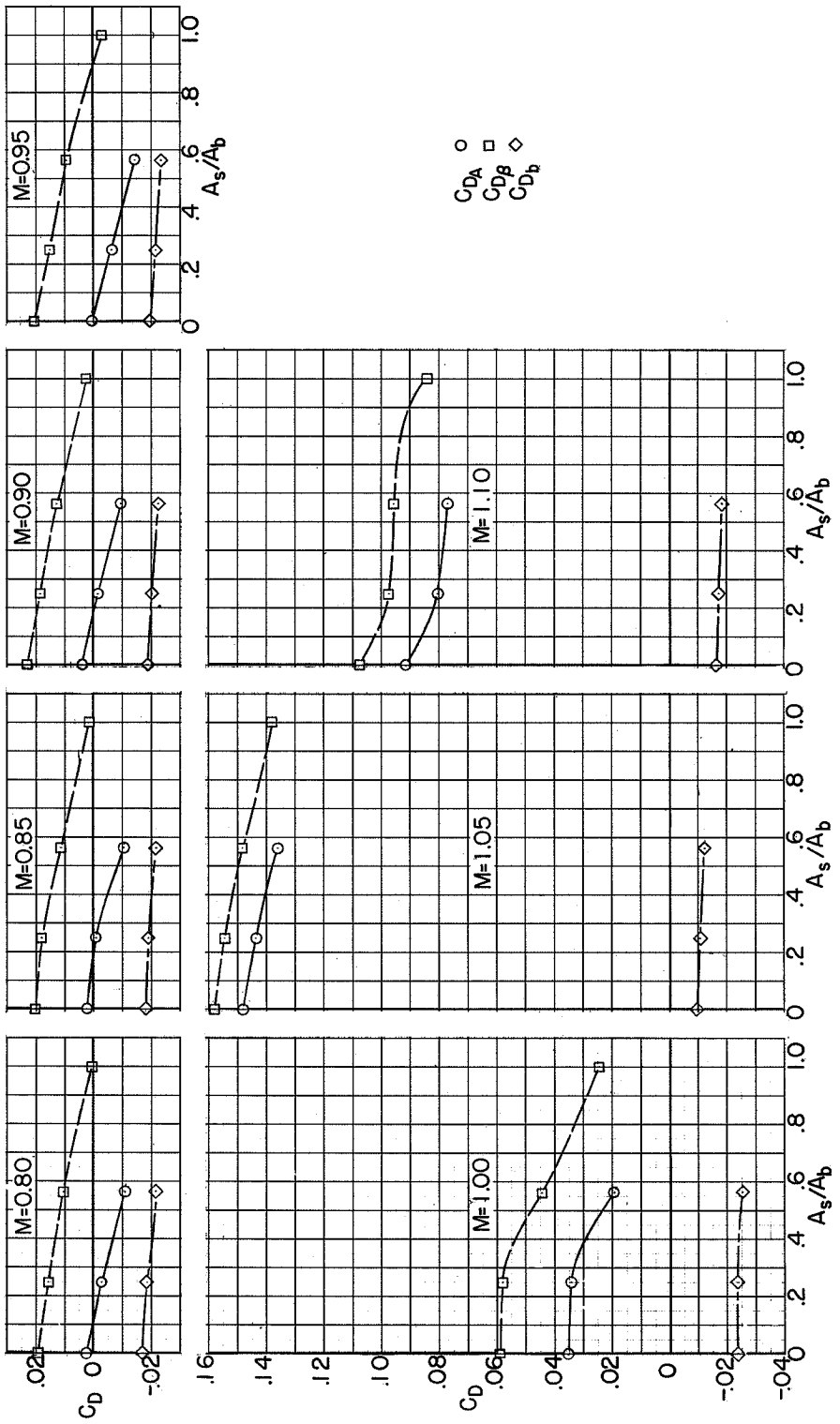

(b) Afterbody I. $\beta = 16^\circ$; $\frac{D_b}{D_m} = 0.334$.

Figure 13.- Continued.

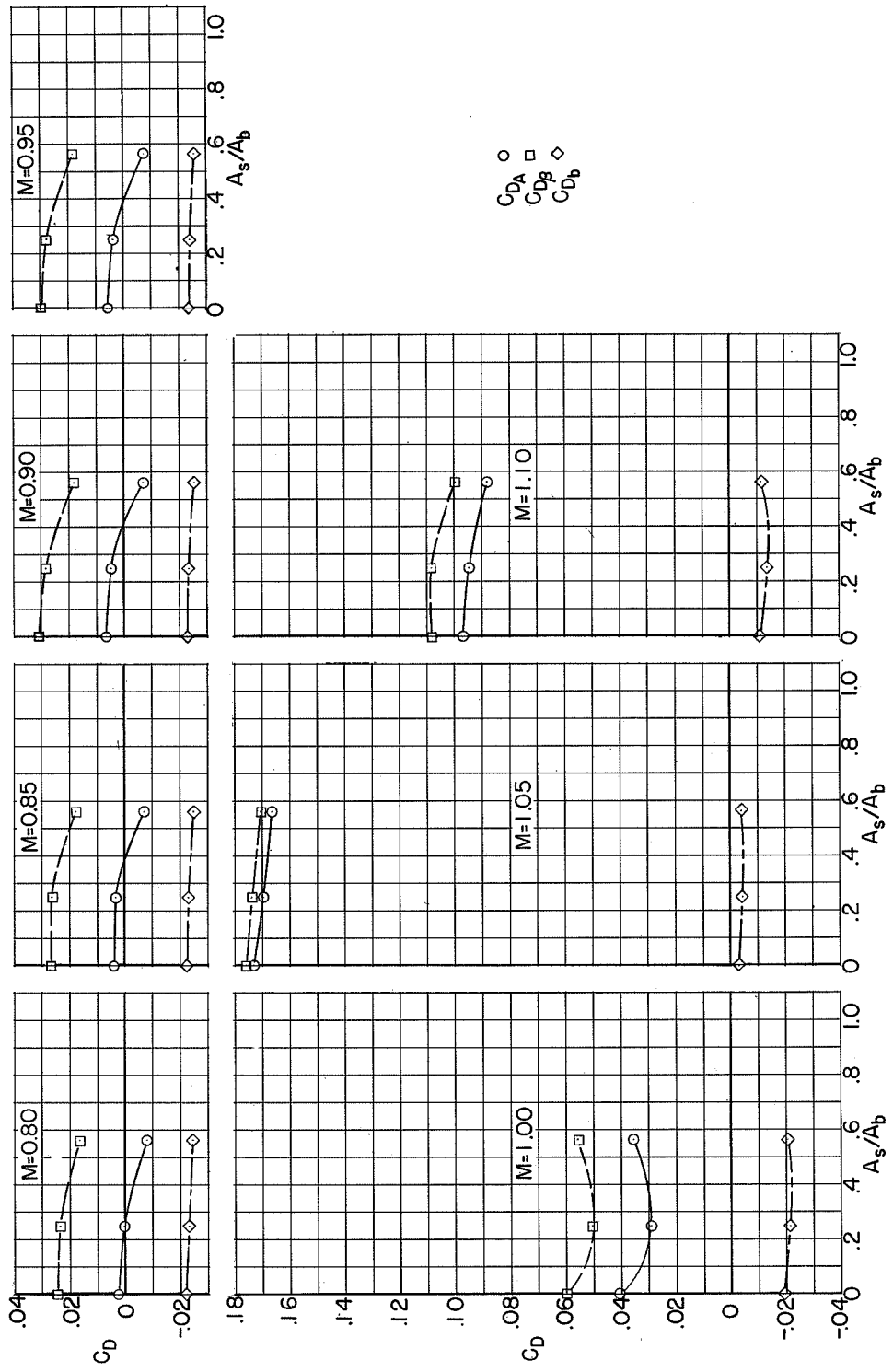

(c) Afterbody II. $\beta = 24°$; $\frac{D_b}{D_m} = 0.334$.

Figure 13.- Continued.

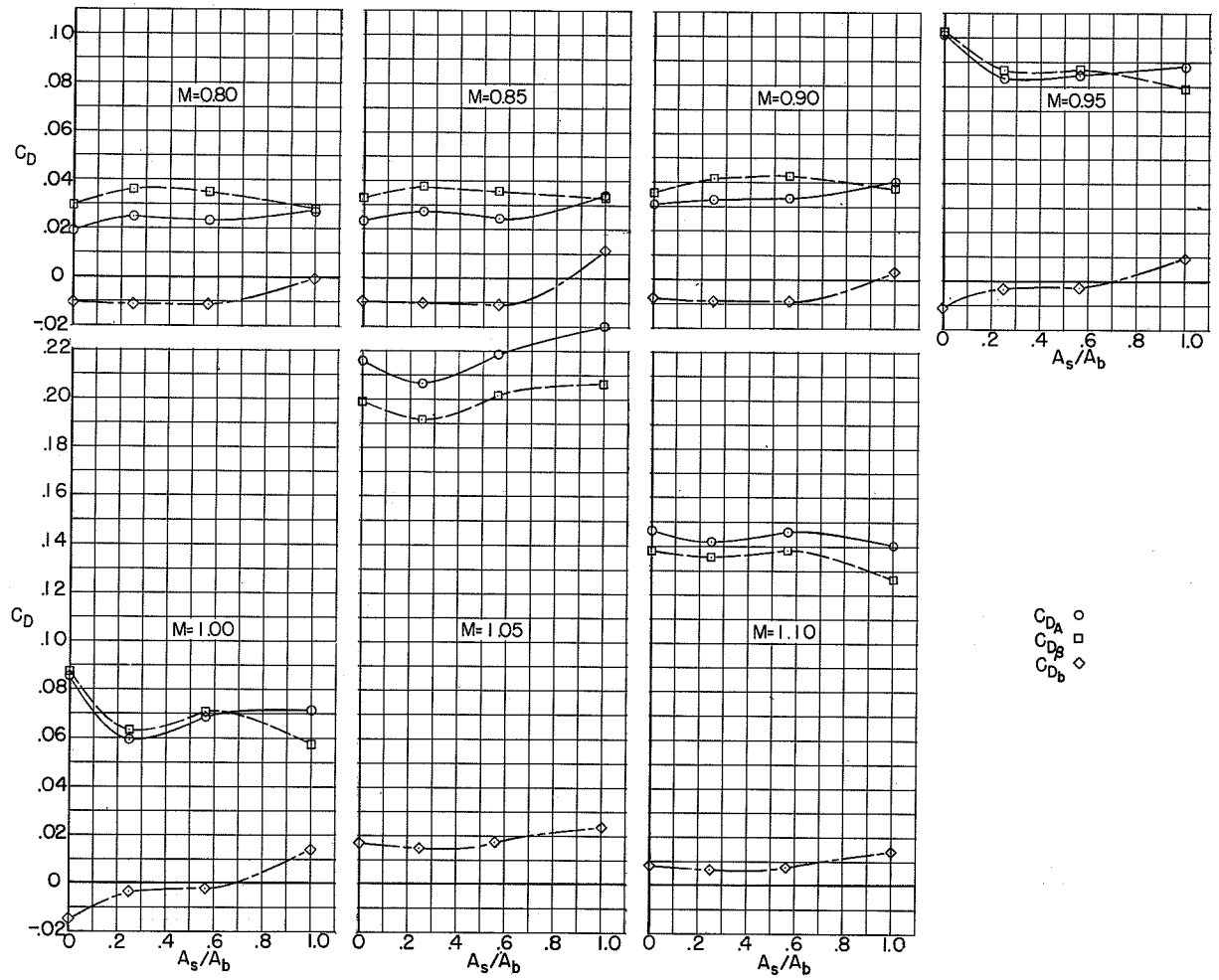

(d) Afterbody III. $\beta = 45^\circ$; $\frac{D_b}{D_m} = 0.334$.

Figure 13.- Continued.

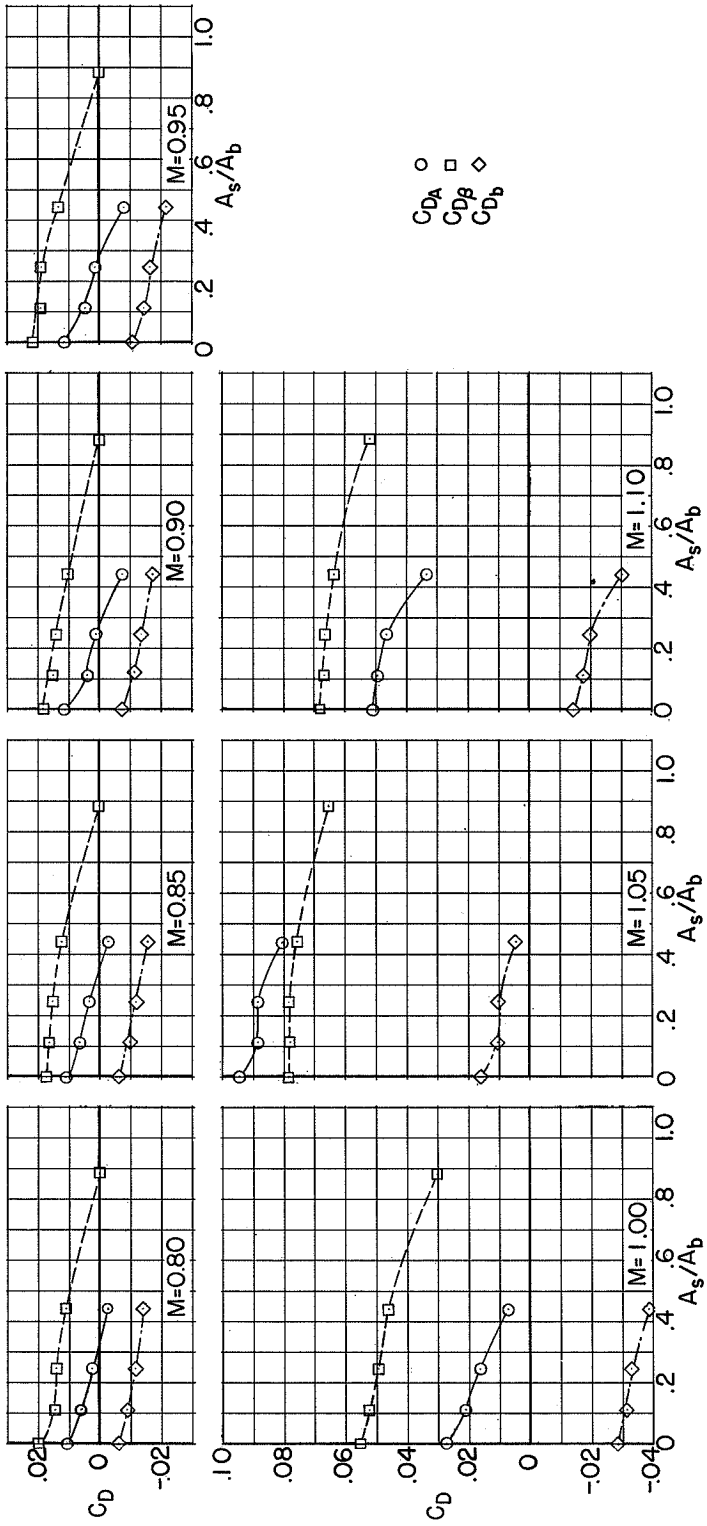

(e) Afterbody IX. $\beta = 7.7^{\circ}$; $\frac{D_b}{D_m} = 0.503$.

Figure 13.- Continued.

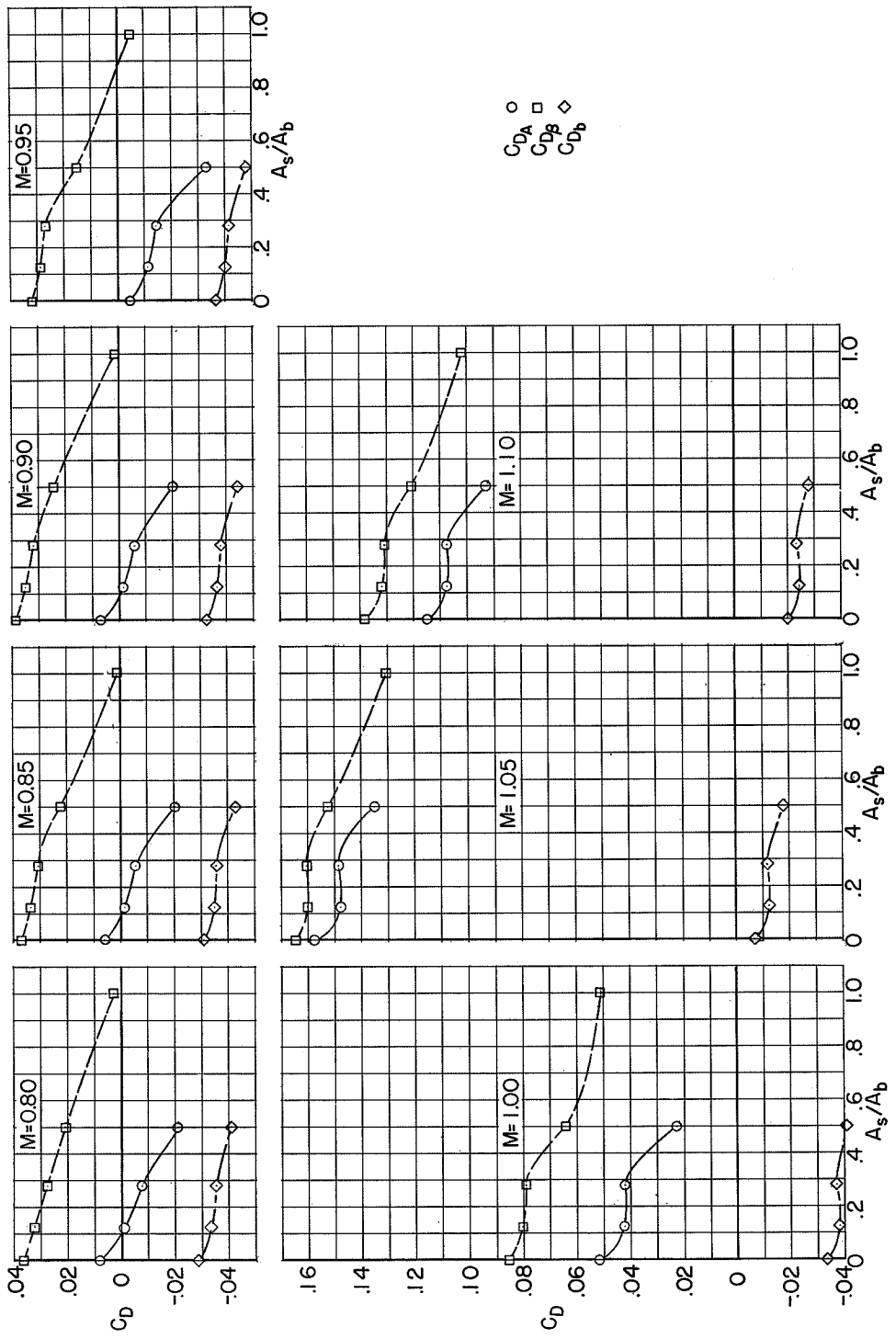

(f) Afterbody IV. $\beta = 16^\circ$; $\frac{D_b}{D_m} = 0.473$.

Figure 13.- Continued.

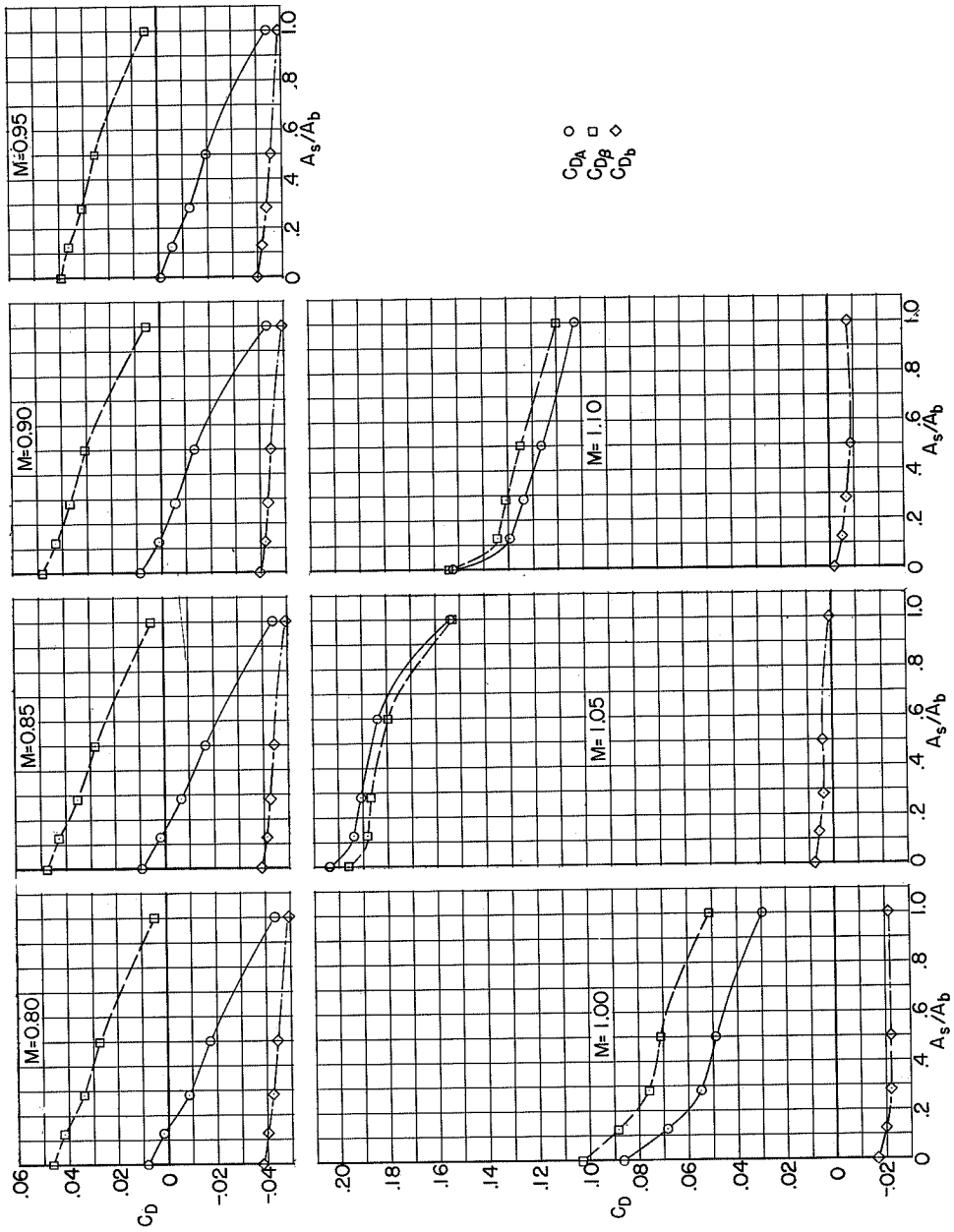

(g) Afterbody V. $\beta = 24^\circ$; $\frac{D_b}{D_m} = 0.473$.

Figure 13.- Continued.

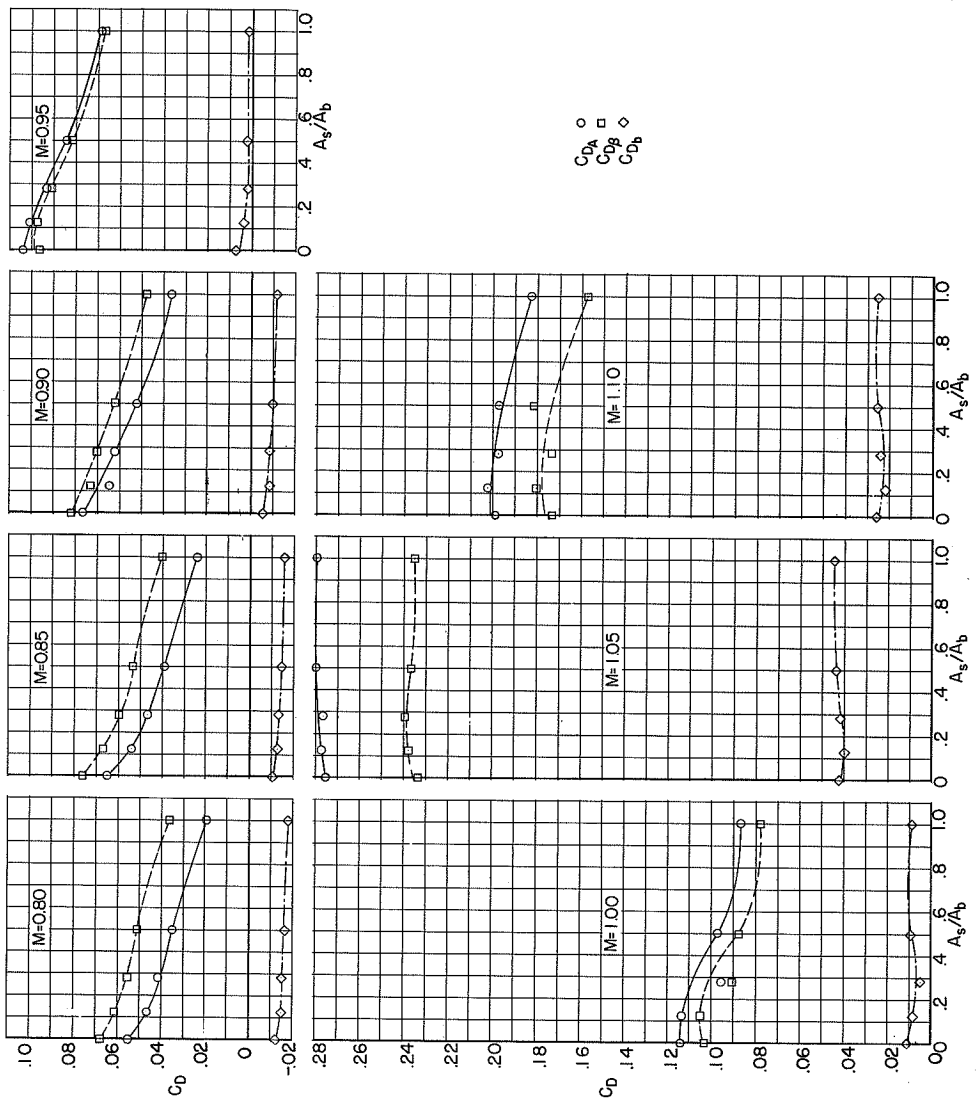

(h) Afterbody VI. $\beta = 45°$; $\frac{D_b}{D_m} = 0.473$.

Figure 13.- Concluded.

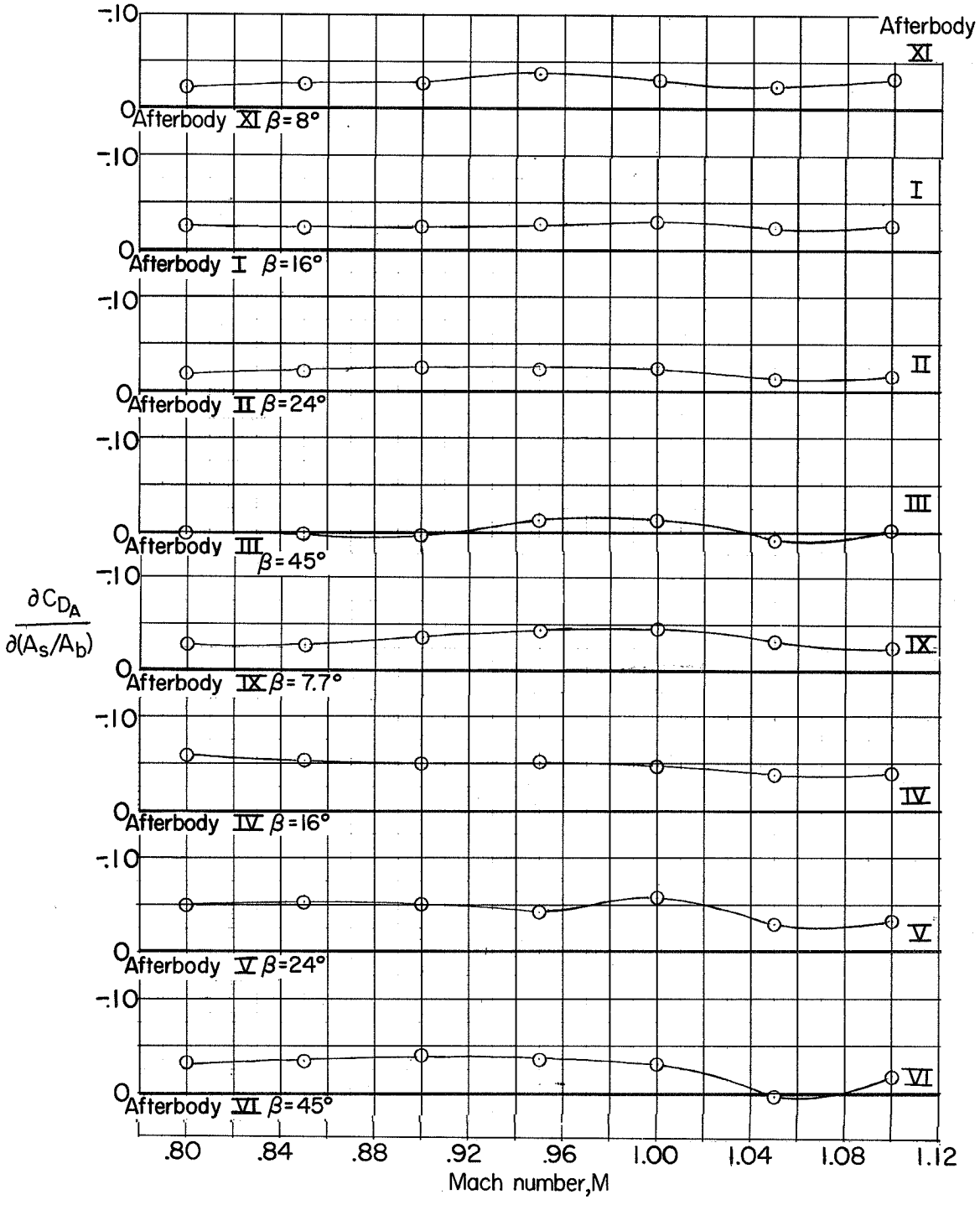

Figure 14.- Variation of sting-size effect with Mach number. $\frac{D_b}{l} = 0$.

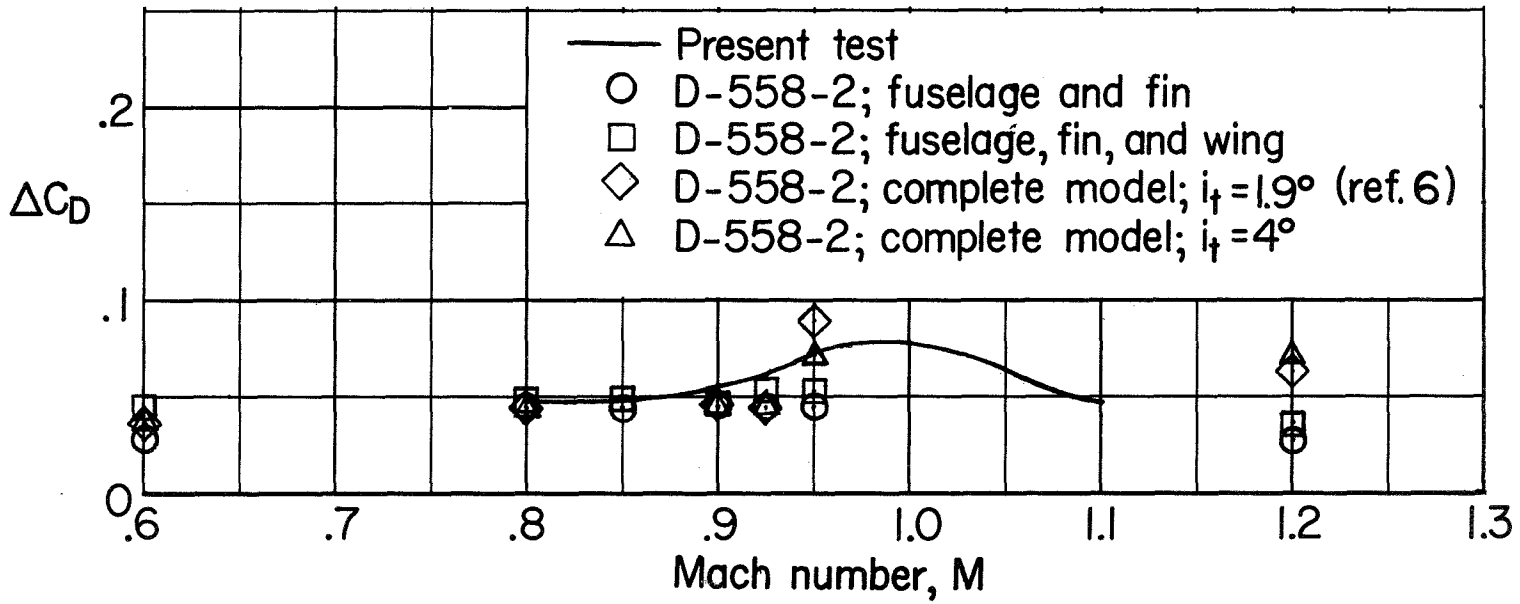

Figure 15.- Comparison of sting corrections from present test with corrections obtained in reference 6.

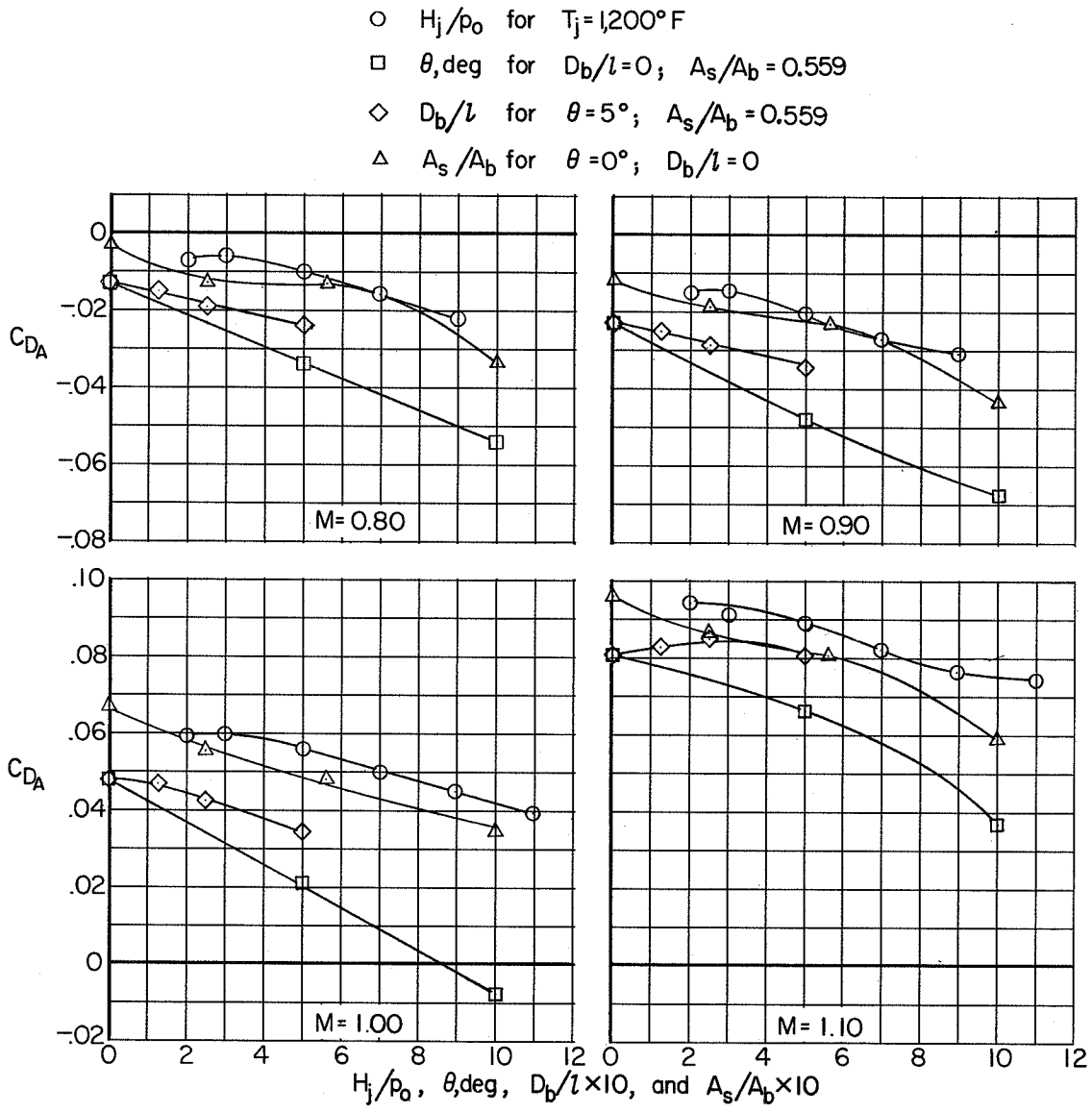

(a) Afterbody XI. $\beta = 8°$; $\frac{D_b}{D_m} = 0.334$; $\frac{D_j}{D_b} = 0.742$.

Figure 16.- Comparison of sting and jet effects.

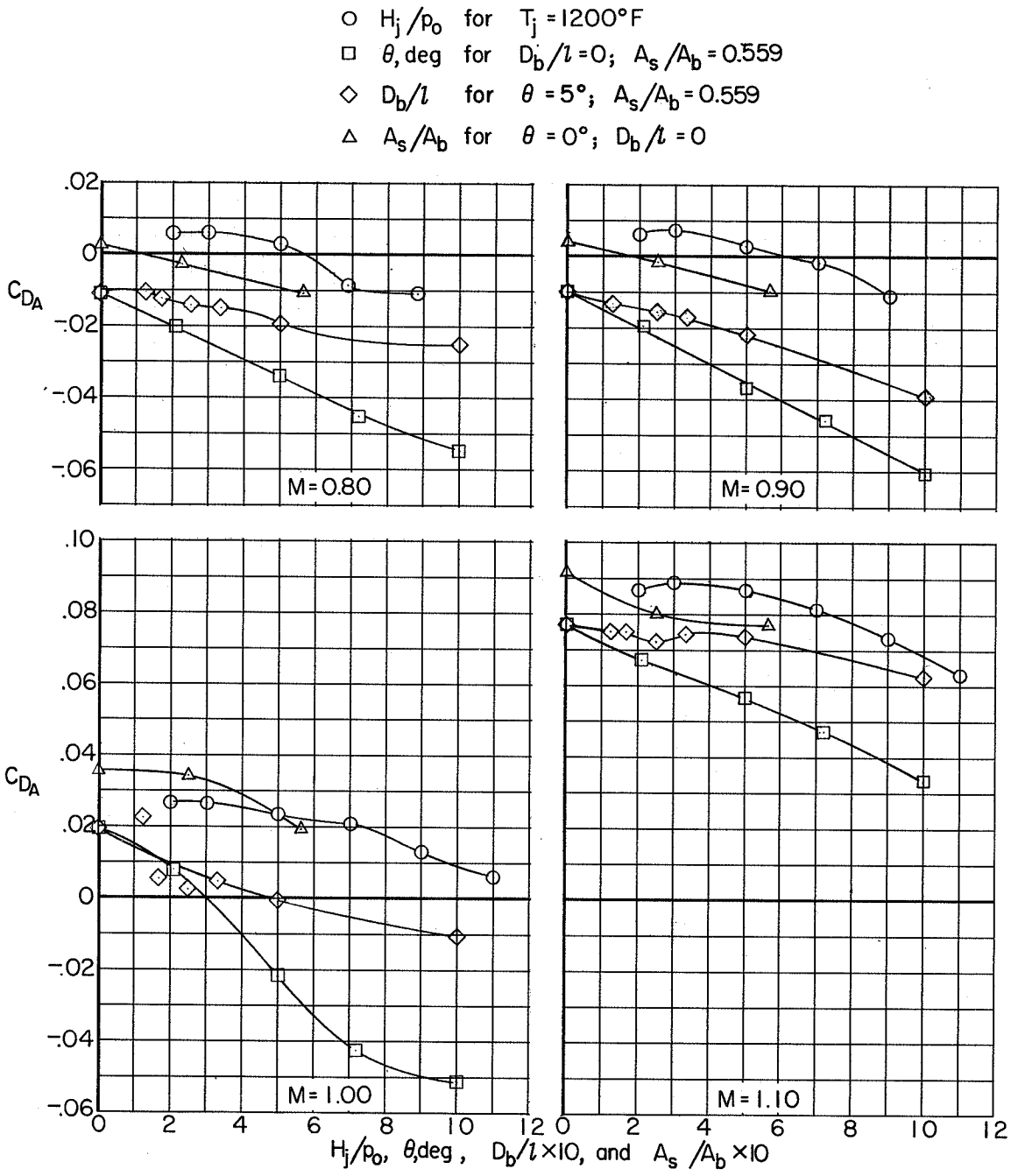

(b) Afterbody I. $\beta = 16^\circ$; $\frac{D_b}{D_m} = 0.334$; $\frac{D_j}{D_b} = 0.742$.

Figure 16.- Continued.

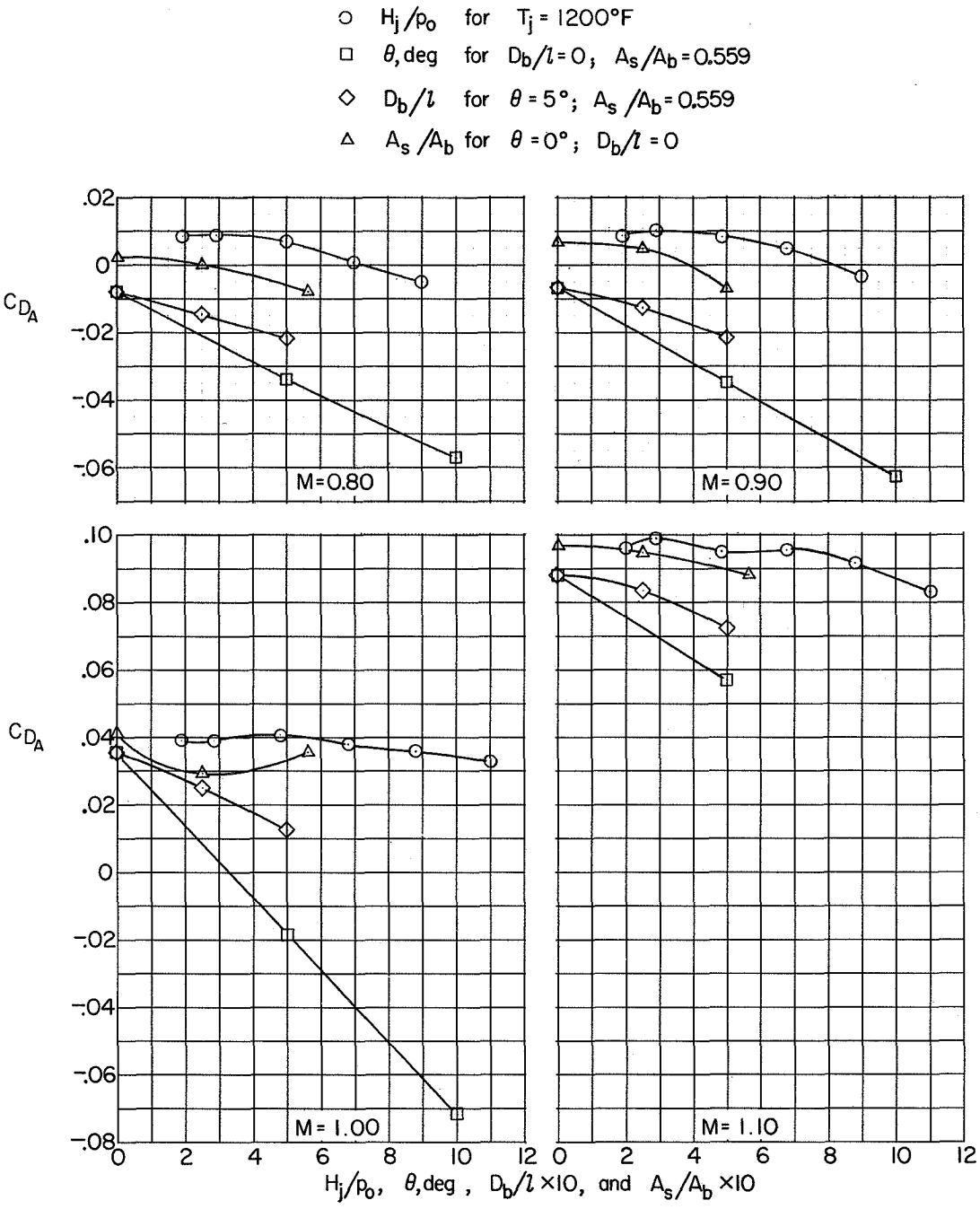

(c) Afterbody II. $\beta = 24^\circ$; $\frac{D_b}{D_m} = 0.334$; $\frac{D_j}{D_b} = 0.742$.

Figure 16.- Continued.

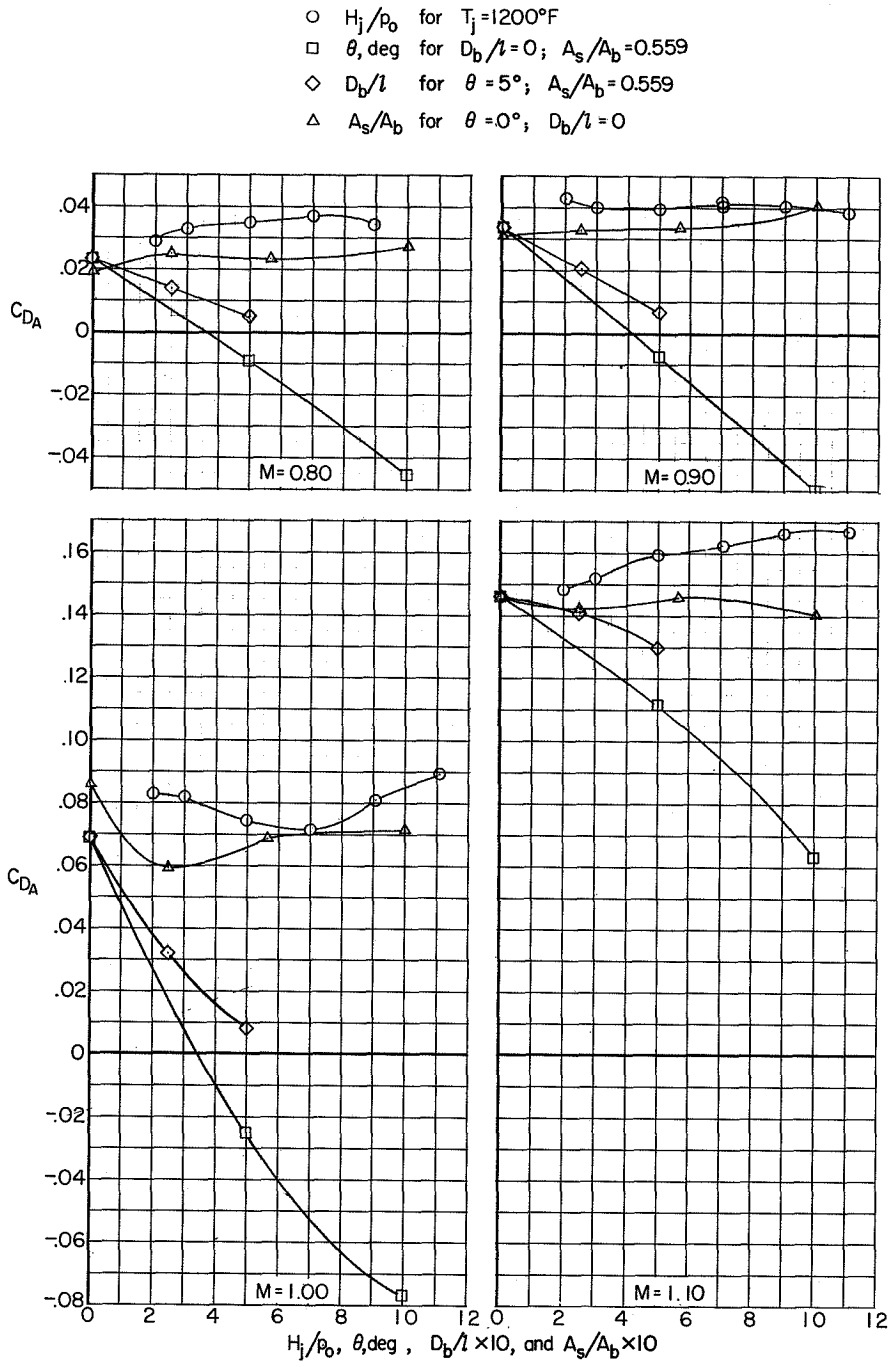

(d) Afterbody III. $\beta = 45^\circ$; $\frac{D_b}{D_m} = 0.334$; $\frac{D_j}{D_b} = 0.742$.

Figure 16.- Continued.

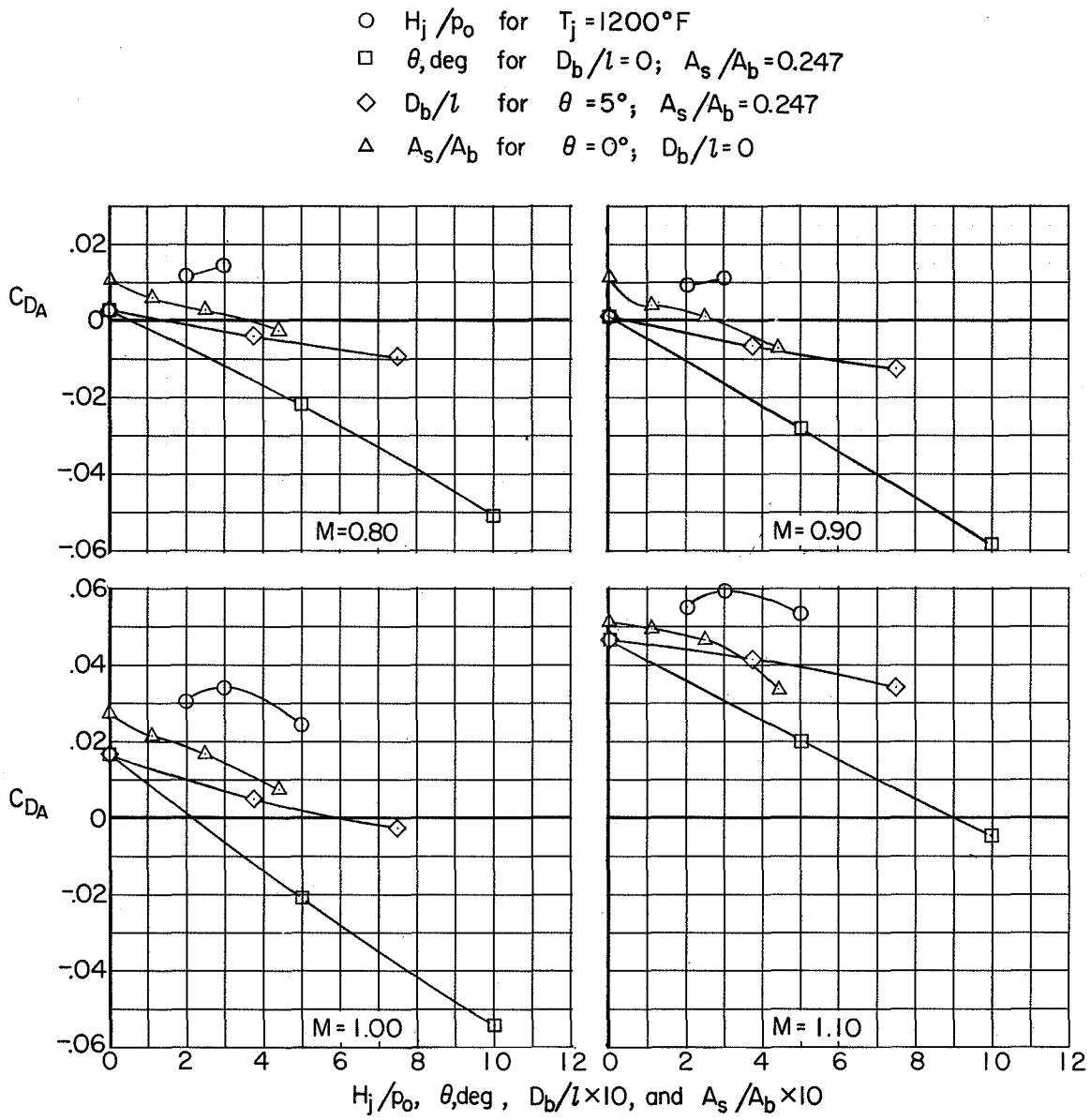

(e) Afterbody IX. $\beta = 7.7^{\circ}$; $\frac{D_b}{D_m} = 0.503$; $\frac{D_j}{D_b} = 0.698$.

Figure 16.- Continued.

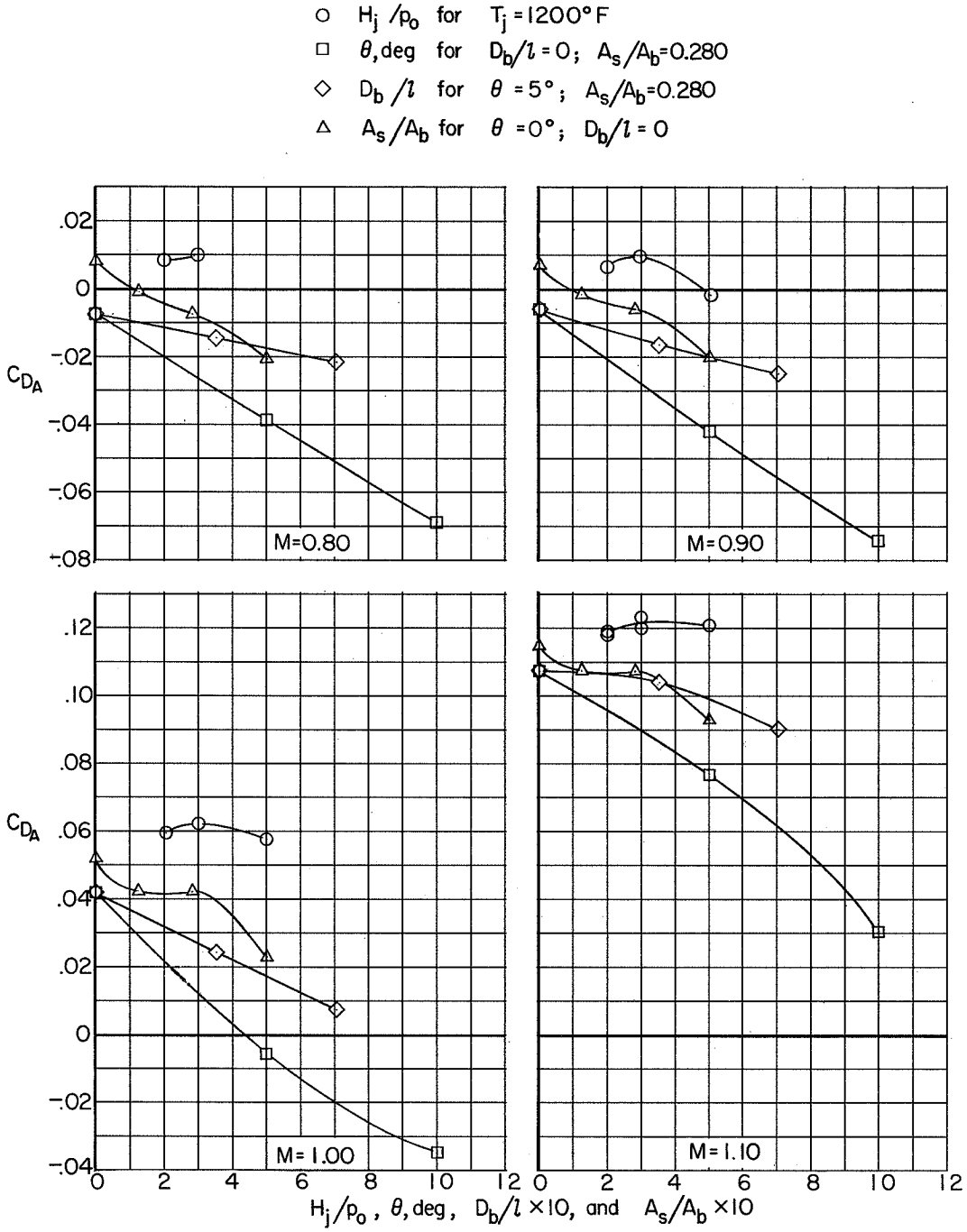

(f) Afterbody IV. $\beta = 16^{\circ}$; $\frac{D_b}{D_m} = 0.473$; $\frac{D_j}{D_b} = 0.742$.

Figure 16.- Continued.

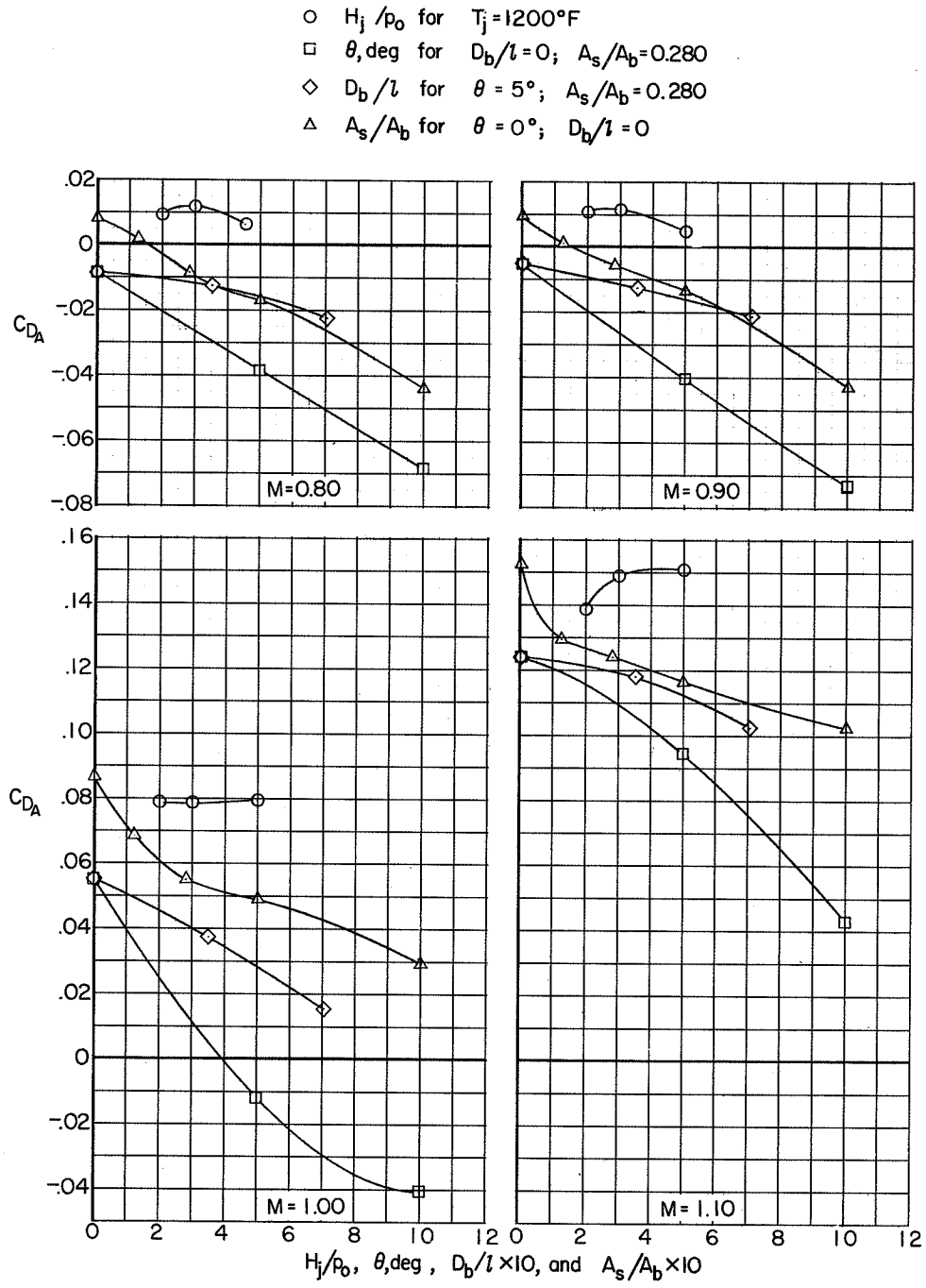

(g) Afterbody V. $\beta = 24^{\circ}$; $\frac{D_b}{D_m} = 0.473$; $\frac{D_j}{D_b} = 0.742$.

Figure 16.- Continued.

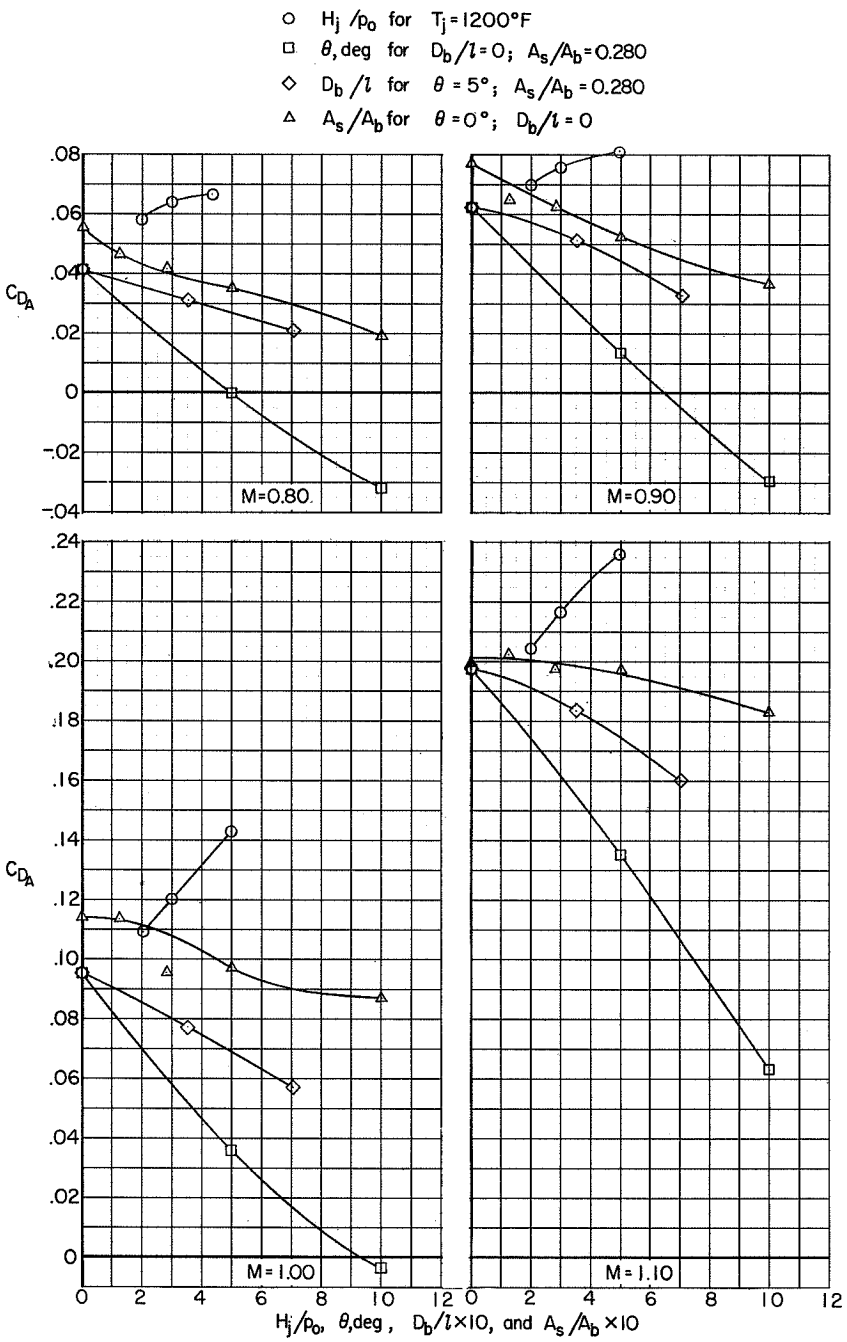

(h) Afterbody VI. $\beta = 45^\circ$; $\frac{D_b}{D_m} = 0.473$; $\frac{D_j}{D_b} = 0.742$.

Figure 16.- Concluded.